Time-Resolved X-Ray Diffraction Study on Superconducting $YBa_2Cu_3O_7$ Epitaxially Grown on $SrTiO_3$

Dissertation
zur Erlangung des akademischen Grades
doctor rerum naturalium (Dr. rer. nat.)

vorgelegt dem Rat der Physikalisch - Astronomischen Fakultät der
Friedrich-Schiller Universität Jena

von Dipl.-Phys. Andrea Lübcke
geboren am 09. 12. 1978 in Grevesmühlen

Gutachter

1. .....
2. .....
3. .....

Tag der letzten Rigorosumsprüfung .....

Tag der öffentlichen Verteidigung .....

Contents

1 Introduction

Sub-ps time resolved X-ray diffraction is extremely successful in studying the propagation of acoustic waves, ultrafast structural phase transitions and optical phonons in time-domain [1–10]. These experiments were performed to demonstrate the power of the time resolved sub-ps X-ray diffraction technique and systems with predictable responses were used. In this PhD thesis the ultrafast diffraction technique was applied to high-T_c superconductors. This is a class of superconducting ceramic cuprates with extraordinary high transition temperatures T_c. The field of High-Temperature Superconductors (HTSC) has opened in 1986 with the discovery of superconductivity in $La_{2-x}Ba_xCuO_4$ by Bednorz and Müller [11]. Starting from a superconducting transition temperature $T_c \sim 30$ K the race for higher T_cs developed rapidly: Already in 1987 superconductivity is reported in $YBa_2Cu_3O_7$ with a transition temperature $T_c \sim 90$ K, exceeding for the first time the boiling point of nitrogen [12]. The highest transition temperature reported up to now is 138 K at ambient pressure in $Hg_{1-x}Tl_xBa_2Ca_2Cu_3O_{8.33}$. The mechanism of HTSC is still controversely discussed. There is a large debate in the literature whether there is a structural response upon entering the superconducting regime (by varying the temperature) or not. And still, no coherent answer has emerged on this point. It is known that at the superconducting phase transition no structural phase transition occurs. However, hypothetically it could be possible that for very short times a different crystallographic phase or different equilibrium positions for the ions may exist. This is schematically shown in Figure 1.1 for the case that the phase transition from superconductivity to the normal conducting state is optically induced. The laser photons excite the groundstate A. The energy hypersurface for the excited state might have a minimum B at a different reaction coordinate. Thus, upon optical excitation the excited state will relax into the metastable state B and subsequently decay again to the ground state energy hypersurface and finally recover to the ground state A. The metastable state B may have different crystallographic properties than the ground state. To study this excited state a very high time resolution is necessary.

The focus of the present work was on the lattice response upon ultrafast optical breaking of Cooper pairs. As sample a thin $YBa_2Cu_3O_7$ film on a $SrTiO_3$

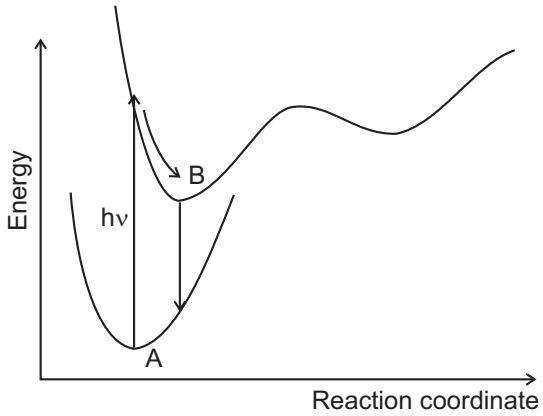

Figure 1.1: Schematic energy hypersurface.

substrate was used. $YBa_2Cu_3O_7$ is certainly the best studied high-T_c superconductor. The reason for using a thin film rather than single crystals was the importance of matching the extinction depths for pump and probe beam: If only a small fraction of the probed volume is excited the (likely) very small signal variation will be even smaller. As the experimental setup was chosen such that the substrate necessarily remains optically unexcited, the substrate's reflection could be used as reference. Surprisingly, the X-ray diffraction signal from the transparent $SrTiO_3$ underneath the strongly absorbing $YBa_2Cu_3O_7$ thin film has changed upon excitation. For this reason it is necessary to give not only an introduction to important properties of the high-T_c film but also to those of the substrate.

A brief review of these properties will be given in Chapter 2. In Chapter 3 conclusions from the properties of the sample for the choice of experimental and theoretical methods will be drawn. The setup of the diffraction experiment will be matter of Chapter 4. In Chapter 5 the results of a first static measurement will be described, before in Chapter 6 the time-dependent diffraction data will be presented. In Chapter 7 these data will be discussed and possible explainations will be proposed.

2 Literature Survey

In this chapter important properties of the $YBa_2Cu_3O_7$ thin film and the $SrTiO_3$ substrate are reviewed. Special attention is given to possible correlations between structural and superconducting properties as well as to the behaviour of high-T_c superconductors under the illumination with ultrashort laser pulses. The kinds of correlations between structure and superconductivity reported in the literature is widely spread. Understanding both, the connection between structure and superconductivity as well as the behaviour under short pulse illumination is very important for the discussion of the experimental results of the present work.

2.1 High-Temperature Superconductors

2.1.1 Universal properties

Even though much of the microscopic origins of high-T_c superconductivity is unresolved, there is consensus on many common properties of the high-T_c superconductors. The aspects of interest for this work will be reviewed briefly. Most of them will be discussed for the special case of $YBa_2Cu_3O_7$.
The unit cell of $YBa_2Cu_3O_7$ is shown in Figure 2.1. Its space group was determined to be $Pmmm$ (no. 47) [13]. Common to all HTSC is their strong anisotropy. A key role for the exceptional properties is awarded to the set of n CuO_2 planes that are separated by charge reservoirs. $YBa_2Cu_3O_7$ contains two CuO_2 planes per unit cell formed by the Cu(2) atoms and the O(2) and O(3) atoms (see Figure 2.1 for the notation). It is believed that the carrier transport and processes responsible for superconductivity are closely related to the CuO_2 planes. The electronic properties of the planes and those of the direction perpendicular to the planes, i. e. the c direction, differ strongly. Conduction in the CuO_2 planes is believed to be established by a charge transfer from the charge reservoir. In case of $YBa_2Cu_3O_7$ this charge reservoir consists of the CuO chains formed by the Cu(1) and O(1) atoms. The O(4) atom plays an important role for transferring the carriers from the reservoir into the CuO_2 planes. In $YBa_2Cu_3O_7$ holes are transferred to the CuO_2 planes by inducing oxygen vacancies in the chains. Besides the deviation from stoichiometry, car-

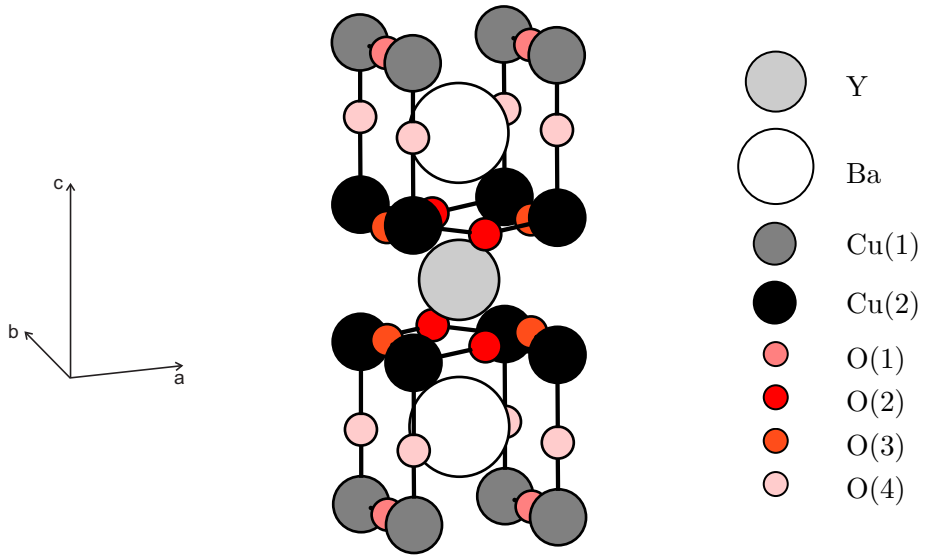

Figure 2.1: Unit cell of $YBa_2Cu_3O_7$.

riers can be provided by chemical substitution, as it is the case for example in $La_{2-x}Sr_xCuO_4$. In Figure 2.2 a phase diagramm of HTSC is shown that accesses both, the *electron doped* regime as well as the *hole doped* regime. Here, the parent compound for the hole doped case is La_2CuO_4. Holes are induced by partially substituting La ions by Sr ions. The electron doped regime can be accessed by starting from Nd_2CuO_4 and partially substituting Ce for Nd. This phase diagramm is thought to be generic for HTSC, even though usually not both sides (electron and hole doped) are accessible. Common to both sides of the phase diagramm is an antiferromagnetism for the undoped parent

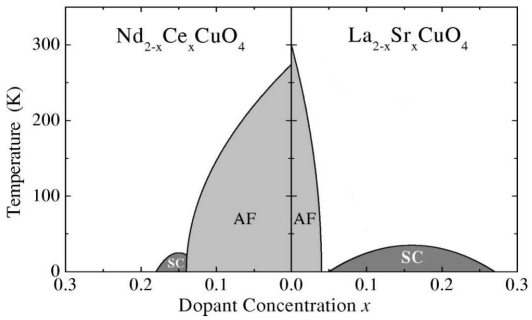

Figure 2.2: Typical phase diagramm of high-T_c superconductors: Starting from an antiferromagnetic insulator (AF), electron (left side) or hole doping (right side) opens a superconducting phase (SC). Reproduced from [14]

compound. At a critical doping level superconductivity emerges in both cases, the hole doped and the electron doped case. With increasing doping level the transition temperature initially also increases (underdoped regime), passing a maximum at the so-called optimum doping, following by a decrease of T_c as the doping level is further increased (overdoped regime).
Tallon et al. showed that for hole doped superconductors the carrier density, defined as holes per Cu atom in the CuO_2 planes, is always the same at optimal doping: $p \approx 0.16$ [15].
Much importance for the phenomenon of high-T_c superconductivity is attached to the dimpling (or buckling) of the CuO_2 planes, i. e. the O atoms and the Cu atoms are not lying in the same plane. Büchner et al. have tuned the buckling angle without modifying the carrier density in $La_{2-x}Sr_xCuO_4$ by Nd-doping and found destruction of superconductivity as a critical buckling angle $\Phi_c \approx 3.6°$ is exceeded [16]. The authors explained this result by a new electronic ground state with probably (local) antiferromagnetic order. Chmaissem et al. have varied the carrier concentration in $(La_{1-x}Ca_x)(Ba_{1.75-x}La_{0.25+x})Cu_3O_y$ ($x = 0.1$ and $x = 0.4$) by varying the oxygen content and measured T_c as well as the buckling angle [17]. They found that both, T_c and Φ, peak at the same carrier concentration, thus are related, suggesting a common origin [17]. Further, Chmaissem et al. bring in line these findings with those of Büchner et al. [16] by concluding that as the composition is changed to increase T_c, there is a structural response competing with superconductivity.

2.1.2 Crystallographic response to superconductivity

Shortly after the discovery of HTSC the search for a relation between superconductivity and structural parameters was in the center of research. This was triggered not only by the BCS theory of conventional superconductors in which the interaction leading to superconductivity is mediated by phonons, but also by the fact that the La-Ba-Cu-O system in which Bednorz and Müller discovered high-T_c superconductivtiy [11], undergoes a structural phase transition when varying the Ba content. While at room temperature the superconducting $La_{1.85}Ba_{0.15}CuO_4$ is tetragonal, La_2CuO_4 is orthorhombic [19] and an antiferromagnetic insulator. Similar to La_2CuO_4 also the $YBa_2Cu_3O_7$ family undergoes a structural phase transition when varying the carrier density (in this case by the oxygen content): $YBa_2Cu_3O_{7-\delta}$ is tetragonal for $\delta > 0.65$ while the structure is orthorhombic for $\delta < 0.65$. Strikingly, also superconductivity disappears for $\delta > 0.65$ [18]. The superconducting transition temperature T_c in dependence on the oxygen content is shown in

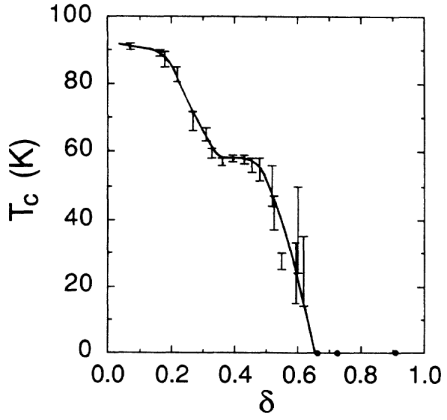

Figure 2.3: The dependence of the critical temperature T_c of $YBa_2Cu_3O_{7-\delta}$ on the oxygen content δ. Reproduced from [18]

Figure 2.3. The optimal doping condition is reached for very small deviation from stoichiometry, i. e. $\delta \approx 0.07$, and the stoichiometric $YBa_2Cu_3O_7$ is still superconducting. This is no contradiction to the statement, that all

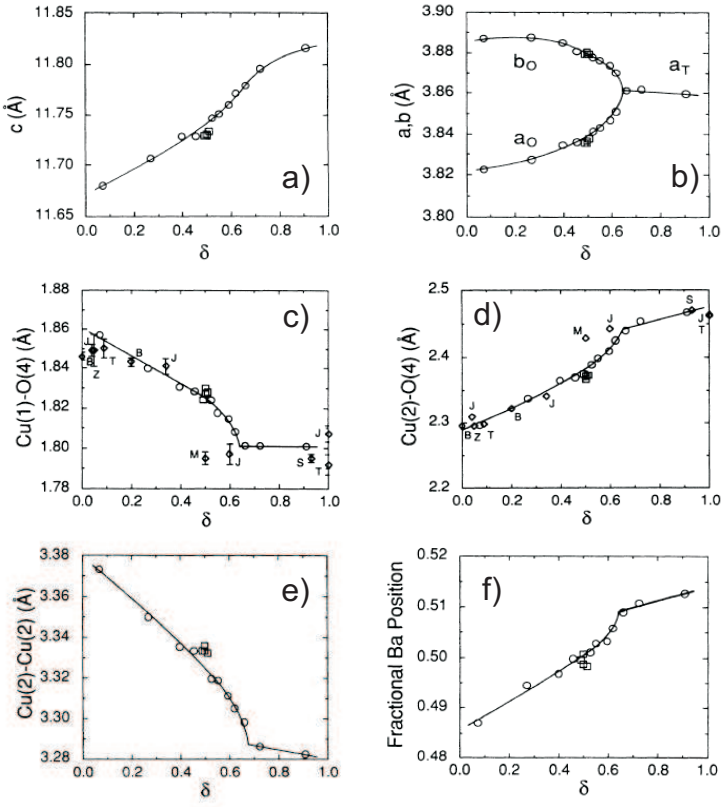

Figure 2.4: Oxygen content dependence of the lattice constants (a and b), the distance of the apical O(4) atom to the two Cu sites (c and d), the distance of the two CuO_2 planes (e)and the fractional Ba position (f). Reproduced from [18]

HTSC have an antiferromagnetic parent compound: The parent compound of the Y-Ba-Cu-O system is the tetragonal $YBa_2Cu_3O_6$, carriers are induced by successivly filling chain-oxygen sites. Thus, the stoichiometric compound $YBa_2Cu_3O_7$ can be considered as slightly overdoped. Jorgensen et al. [18] also measured crystal parameters as well as atomic positions by means of neutron powder diffraction and Rietveld refinement. Some selected results are reproduced in Figure 2.4. While there is no anomaly in the c lattice parameter (Figure 2.4a), the transition from orthorhombic to tetragonal symmetry in a and b lattice constants is readily seen (Figure 2.4b). Furthermore, the position of the apical oxygen O(4) (Figure 2.4c and d), the distance of the two CuO_2 planes (Figure 2.4e) as well as the fractional Barium position (Figure 2.4f) show a distinct discontinuity in their first derivative as a function of oxygen content.

If superconductivity is closely related to the crystal structure one may expect crystallographic changes also when varying the temperature over a region that includes the superconducting transition. In fact, many studies report anomalies in various parameters. Paul et al. [20] performed temperature dependent, high resolution neutron powder diffraction experiments on $La_{1.85}Ba_{0.15}CuO_4$. They measured the orthorhombic splitting $(b-a)/(b+a)$ occuring after the tetragonal to orthorhomic phase transition at about 180 K, and they found a close relation between the temperature dependences of the resistivity and the

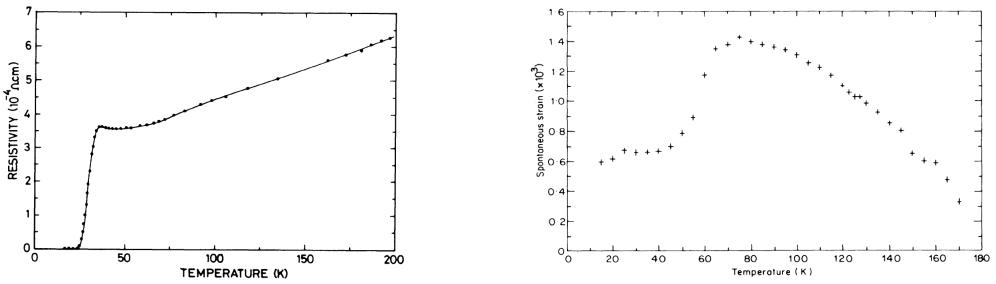

Figure 2.5: Temperature dependence of resistivity and orthorhombic splitting (defined as spontaneous strain) for $La_{1.85}Ba_{0.15}CuO_4$ (reproduced from [20]). Below 180 K the crystallographic structure is orthorhombic. The orthorhombic splitting increases monotonically with decreasing temperature down to 75 K where the lattice distortion surprisingly starts to decrease again. Around 35 K, the superconducting transition temperature, the orthorhombic distortion saturates.

orthorhombic splitting (see Figure 2.5).

Horn et al. were the first to publish temperature dependent X-ray scattering data on $YBa_2Cu_3O_7$ [21]. They observe, similar to Paul et al. for $La_{1.85}Ba_{0.15}CuO_4$, an anomalous temperature dependence of the orthorhombic strain near the superconducting transition temperature (see Figure 2.6).

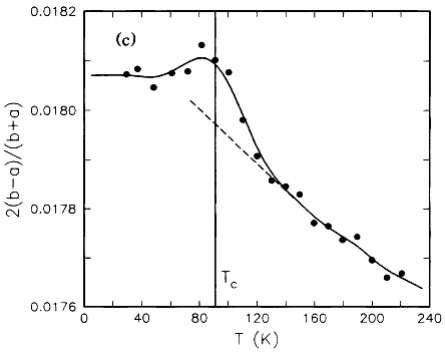

Figure 2.6: The temperature dependence of orthorhombic strain in $YBa_2Cu_3O_7$ [21]. At T_c the orthorhombic strain is maximal, being stabilized in the superconducting phase at a constant value.

Srinivasan et al. performed X-ray powder diffraction on $YBa_2Cu_3O_7$ and studied the variation of the lattice parameters with temperature [22]. They report a discontinuity in the c lattice constant while crossing the superconducting transition temperature. Within their experimental uncertainties they observed an anomalous behaviour neither of the a and b lattice constants nor of the orthorhombic strain (see Figure 2.7).

In a theoretical study Millis and Rabe [23] predicted slope discontinuities and fluctuations of the lattice constants of superconductors whose order parameter is coupled to the lattice strain at T_c. You et al. [24] confirmed these predictions experimentally by means of high resolution X-ray diffraction. They found unexpectedly large slope discontinuities of the lattice constants near T_c and possible fluctuations over a wide temperature range. Meingast et al. [25] used high resolution dilatometry on untwinned $YBa_2Cu_3O_7$ crystals to measure the

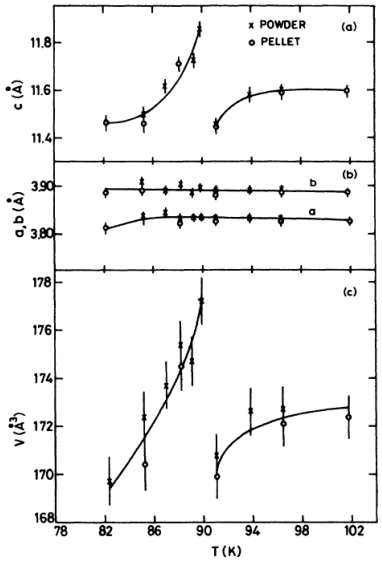

Figure 2.7: X-ray powder diffraction data from [22] for $YBa_2Cu_3O_7$. While the a and b lattice constants do not show any special features within experimental uncertainties, Srinivasan et al. measured a rather large discontinuity for the c-axis lattice constant as well as for the unit cell volume.

thermal expansion and found a large anisotropy within the *ab* plane (see Figure 2.8). From their data on the temperature dependence of the orthorhombic strain they could qualitatively confirm the observations of Horn et al. [21], who observed a reduction of the orthorhombic distortion at the transition tempera-

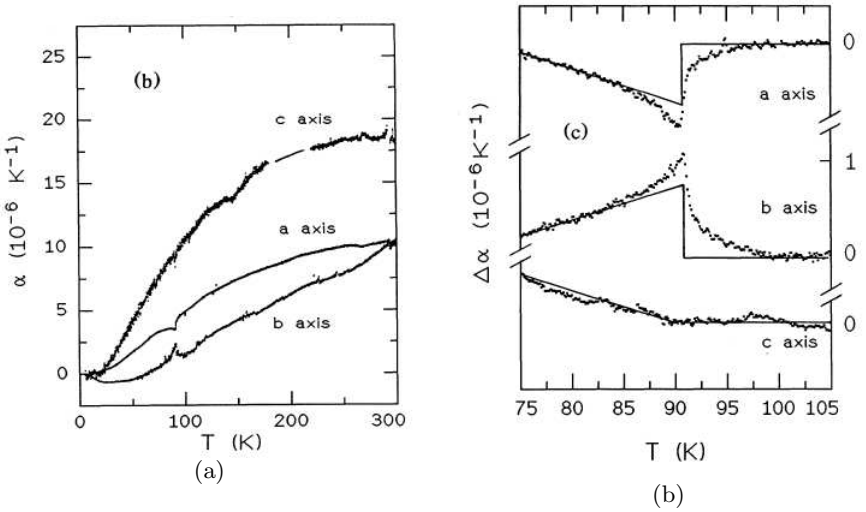

Figure 2.8: Temperature dependence of the expansivities α of $YBa_2Cu_3O_7$ reproduced from [25]. In (b) a linear fit to the data above T_c was substracted. Deviations from the mean field behaviour (solid lines) are considered as a result of superconducting fluctuations.

ture.

Some of the observations described above cannot be reproduced by other authors and, as already indicated, are contradictory, such as Meingast et al. [25] did not observe any discontinuity for the lattice constants contrary to Srinivasan et al. [22], who observed a jump in the c lattice constant. There are certainly many reasons for the discrepencies. But a very important parameter is definitely the kind of sample used for the experiments: The sample can be on hand as single crystal, powder or thin film. Also the real structure plays an important role. Especially for the early experiments twinning of the sample made conclusions on the a and b axis difficult. Finally, also the presence of different phases, e. g. $YBa_2Cu_3O_8$ in a $YBa_2Cu_3O_7$ sample, can complicate the analysis.

2.1.3 Superconducting Stripes

A substantial progress in the understanding of high-T_c superconductivity as a process closely related to local distortions rather than global ones was achieved by the application of atomic-pair-distribution analysis to High-Temperature

Superconductors [26–30].
The atomic pair distribution function (PDF) is essentially obtained by a Fourier transform of a total powder diffraction pattern (diffuse scattering included) and gives the bond length distribution of the material under investigation. It is thus a probe for the local environment of a certain atom. Dmowski et al. reported already in 1988 strongly correlated local displacements of thallium and oxygen atoms in superconducting $Tl_2Ba_2CaCu_2O_8$ obtained from PDF analysis at 17 K [26]. Two different structures were identified, which form chains or pairs and which both have orthorhombic symmetry. However, due to the absence of superlattice peaks, Dmowski et al. concluded that it is a question of short range order rather than long range. Toby et al. [27] reported the first observation of local structural changes at the transition from normal conductivity to superconductivity in $Tl_2Ba_2CaCu_2O_8$. They proposed a change in the pattern of oxygen buckling in the CuO_2 planes through T_c to explain their results.
A variety of models for $YBa_2Cu_3O_7$ using local lattice distortions to explain high-T_c superconductivity was introduced. The most important are:

- Zigzag–like CuO chains where the chain O(1) atom is displaced in a direction.
- A double-well potential for the apical O(4) atom. A theoretical model with two different apical oxygen sites is suggested in order to realize a strong enhancement of the electron-lattice coupling [31].
- Split planar Cu(2) sites. The CuO_2 planes are suggested to be locally distorted, leading to two different Cu(2) positions.

François et al. [32] performed high resolution neutron powder diffraction and also analyzed the thermal factors. For the chain oxygen O(1) atoms they found anomalously large values of the thermal factors, which supports the model of zigzag–like CuO chains. Experimental support for a double well potential of the apical oxygen came from Mustre de Leon et al. [28,33], who performed Cu-K edge extended X-ray absorption fine structure spectroscopy of $YBa_2Cu_3O_7$. They found two different Cu(1)–O(4) bond lengths and interpreted this as resulting from a double well potential for the apical oxygen O(4) atom. The two nearly equally populated sites are 0.13 Å apart from each other for temperatures above or away from T_c. The distance is reduced by 0.02 Å at temperatures close to T_c. Sullivan [34] performed room temperature X-ray diffraction studies on untwinned $YBa_2Cu_3O_7$ single crystals and calculated the electron-density Fourier map. They found distortions of the electron density of the planar cop-

per ions and interpreted this in terms of nonhomogeneous CuO_2 planes: Instead of two different apical oxygen sites (as suggested by the double well potential model) their data is consistent with two different planar Cu(2) sites leading to a modulated buckling of the CuO_2 planes and two different Cu(2)-O(4) bond lengths. The apical O(4) atom, however is displaced slightly in the *ab* plane [34]. Distortions of the CuO_2 planes in high-T_c superconductors were also found by Bianconi et al. and Gutmann et al. [29, 30, 35]. Bianconi et al. measured the Cu-O pair distribution function in $La_{1.85}Sr_{0.15}CuO_4$ and in $Bi_2Sr_2CaCu_2O_{8+y}$ finding in both cases a small and a large value for the CuO bond length for both the planar and the apical bond. Gutmann et al. measured the atomic pair distribution functions of $YBa_2Cu_3O_7$ by pulsed neutron diffraction finding also indications for two different planar copper sites. This situation is sketched in Figure 2.9. Copper atoms are found occupying positions A and B. As a microscopical model Gutmann et al. suggest different charge states of the copper ion in the CuO_2 planes, which determines its equilibrium position in the CuO_5 pyramide. The copper ion at site A is triply positively charged, thus closer to the negatively charged oxygen ions, i. e. more inside the CuO_5 pyramide than

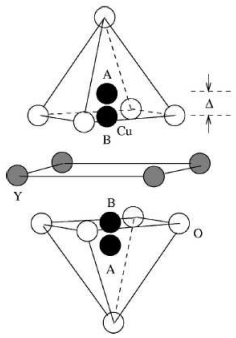

Figure 2.9: Gutmann et al. found 2 different planar Cu(2) sites A and B in $YBa_2Cu_3O_7$. Reproduced from [30].

the copper ion at site B, which is doubly charged.

The picture that has emerged from a variety of studies on local distortions in high-T_c superconductors shows that the CuO_2 planes form stripes in *b* direction. This is sketched in Figure 2.10. The CuO_2 planes are structurally inhomogenous. Distorted "D" stripes alternate with undistorted "U" stripes. In *z* direction these inhomogeneous CuO_2 planes are separated by metallic or insulating blocks as for example in $YBa_2Cu_3O_7$ the BaO and CuO blocks. It seems that the modulation of the CuO_2 planes can be commonly described by

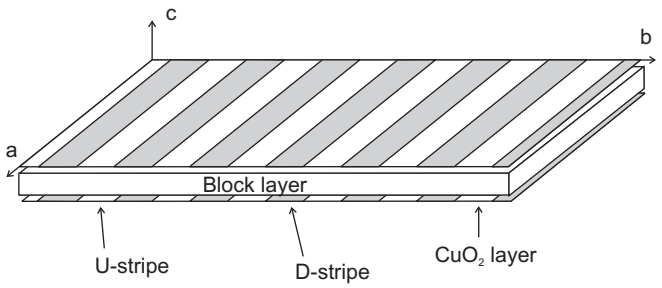

Figure 2.10: Local structural distortions of the CuO_2 lead to stripes along the b direction.

a superstructure of the type $\mathbf{q} = p\mathbf{b}^* + \frac{1}{n}\mathbf{c}^*$ in the orthorhombic notation (for approximately optimally doped cuprates) with the reciprocal lattice vectors $\mathbf{b}^*$ and $\mathbf{c}^*$. Examples are shown in Table 2.1. For $YBa_2Cu_3O_7$ no such a static

Material	p	n	Reference
$Bi_2Sr_2CaCu_2O_{8+\delta}$	0.21	2	[36–38]
$Bi_2Sr_2Cu_2O_{6+\delta}$			[39, 40]
$La_2CuO_{4.1}$	0.2	3	[41]
$La_{1.925}Sr_{0.075}Cu_2O_4$	0.16	2.5	[42]

Table 2.1: Superstructure parameters for various high-T_c superconductors.

superstructure could be determined but this might be explained if stripes in $YBa_2Cu_3O_7$ were highly dynamic.

The stripe phase manifests itself not only in lattice distortions but also in electronic inhomogeneities. The first proof of one-dimensional electronic structures was brought by Tranquada et al. [43]. They performed neutron scattering studies, finding that charge carriers in the CuO_2 planes of cuprates are confined in narrow one-dimensional lines. These stripes are separated by antiferromagnetic (and presumably insulating) regions. An important role in the theory of high-T_c superconductivity is attributed to dynamic charge stripes which is in accordance with experimental data for example by Mook et al. and Sharma et al. [44, 45]. On the specific properties, the origin and the role of dynamic charge stripes in high-T_c superconductors there is still an intensive ongoing discussion [46, 47]. However, the occurence of stripes will influence global electronic properties of the superconductor. Perali et al. suggested a rather simple model to account for the high transition temperatures to superconductivity [48]: The heterostructure of one-dimensional charge stripes gives rise to electronic subbands. The position of the bottom of a subband is dependent on the exact

geometry of the stripes. Perali et al. propose that the high superconducting transition temperatures can be explained by the vicinity of the chemical potential and the bottom of such a subband. Bianconi and Saini measured a width of the stripes [35, 49] that supports the model of Perali et al.

2.1.4 High T_c superconductors under short pulse illumination

Studying optically excited High-Temperature Superconductors can provide very important information on the non-equilibrium behaviour of these materials, such as quasiparticle creation and relaxation [50–55]. This gives insight into possible mechanisms underlying the phenomenon of high-T_c superconductivity. To understand the possible interaction between Cooper pairs and the crystal lattice, it is crucial to understand the basic mechanisms of quasiparticle creation and relaxation.

The most common way to study the photoresponse is to measure the transient reflectivity or transmittivity. This allows for a very high time resolution of the carrier dynamics, as it is limited by the laser pulse duration only. In metals a variety of mechanisms can contribute to the change of optical reflectivity due to heating [56]:

1. The decrease of plasma frequency due to volume thermal expansion. This causes shifts and bending of the electron energy bands by changes in the one-electron potential and, subsequently, a shift of the Fermi-level.

2. Shear strains due to thermal expansion if the sample is constrained by a substrate. This can lead to splitting of degenerate energy bands and shifting and warping of the bands. Again, the Fermi-level shifts.

3. Broadening of the step in the Fermi distribution. This affects all interband transitions that originate or terminate on states near the Fermi-level.

4. Increase of phonon population. This causes a decrease of electron relaxation times and leads to shifts and bending of energy bands due to electron-phonon interaction.

For very short times after the excitation of the sample the points 1 and 2 will not contribute significantly to the reflectivity change. The main contribution arises from the broadening of the Fermi distribution: As the temperature of the conduction electrons is increased, the number of unoccupied states below the Fermi energy is increased and above the Fermi energy decreased. Subsequently, probing the sample with photon energies smaller than the difference between valence band edge and Fermi energy will result in negative reflectivity changes

as more photons can be absorbed by electrons in the valence band. In turn, probing with photon energies higher than the difference between valence band edge and Fermi level will result in an increased reflectivity as there is a larger number of free electrons. For $YBa_2Cu_3O_7$ the Fermi level is around 0.25 eV [57], which is much lower than in conventional metals, where the Fermi level is several eV [58]. For this reason optical reflectivity transients in normal conducting $YBa_2Cu_3O_7$ are positive. This was measured for example by Han et al. [51] (see Figure 2.11a)). Upon heating by a pump pulse (60 fs, photon energy: 2 eV, flux: 3 μJ/cm^2), an ultrafast increase of reflectivity is measured, followed by a slow bolometric relaxation with a time scale of about 3 ns at 300 K. As the sample is

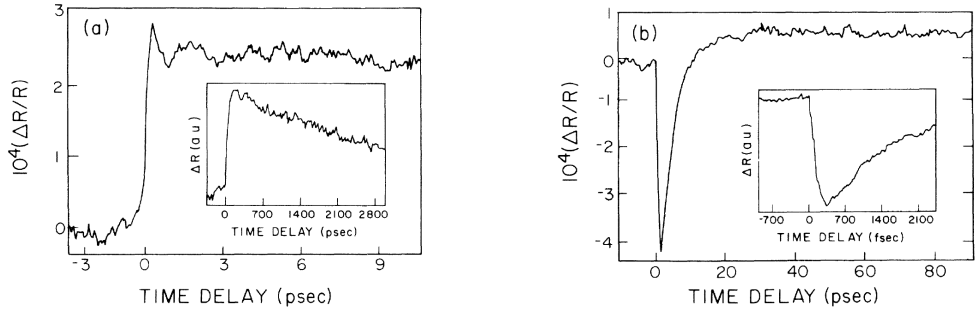

Figure 2.11: Transient reflectivities of $YBa_2Cu_3O_7$, following excitation with 2 eV photons above T_c at 300 K (a) and below T_c at 40 K (b). In the metallic case the reflectivity increases upon optical excitation, relaxing on time scales of several ns (shown in the inset). In the superconducting state, there is an ultrafast decrease of reflectivity and a much faster relaxation than in the superconducting case on time scales of few ps (see inset). Reproduced from Han et al. [51]

cooled below the transition temperature, the ultrafast photoresponse changes dramatically: Reflectivity is reduced with a characteristic time scale of 300 fs, followed by a slower increase with a time scale of few ps. The initial reflectivity is even exceeded and relaxes, subsequently, on much longer time scales. (see Figure 2.11(b)). Han et al. discuss the initial rapid photoresponse in the superconducting state in terms of an avalanche multiplication of quasiparticles due to hot-carrier thermalization which occurs immediately after photoabsorption. The relaxation is discussed as quasiparticle recombination into Cooper pairs followed by a thermal relaxation producing a bolometric response with $\Delta R > 0$. They suggest that the reflectivity is changed by a redistribution of oscillator strength in a two fluid model: The Drude contribution of the free electrons in metals to the conductivity is a Lorentzian around $\omega = 0$ with a width given by the scattering rate. As the metal undergoes the superconducting transition this scattering rate is reduced to zero and the lorentzian transforms to a δ-function.

Optical breaking of Cooper pairs will (partially) reestablish the metallic Drude contribution leading to a contribution of free electrons to the conductivity at finite frequencies, that changes the reflectivity for the probe beam at 2 eV. Reitze et al. [59] and Mazin et al. [60] however have shown that a simple redistribution of oscillator strength is insufficient to explain both the magnitude and the sign of $\Delta R/R$. A better understanding of the optical response in the superconducting state was achieved by the detection of coherent optical phonons in $YBa_2Cu_3O_7$ by Albrecht et al. [61]. Their data is shown in Figure 2.12. They

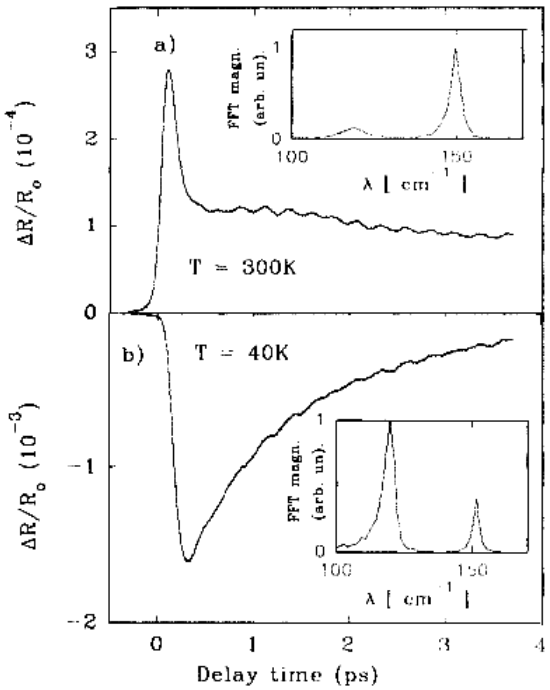

Figure 2.12: Transient optical reflectivity at 1.5 eV after excitation with an ultrashort pulse of the same photon energy at 300 K and 40 K. Reproduced from [61]. The insets show the Fourier transforms of the modulated part of the data. Note the different scales for the reflectivity.

used 1.5 eV photons and a fluence of about 15 μJ/cm^2, which is a factor of 5 larger than the fluence used by Han et al. [51]. Above T_c there is an ultrafast increase of reflectivity due to opening of states below the Fermi level and occupation of states above the Fermi level. The following fast decrease is caused by rapid carrier cooling due to phonon escape into the lattice; the slowly decaying background is due to lattice relaxation. In addition, the data features an oscillatory part that can be explained in the frame of displacive excitation of coherent phonons [62], where the oscillations are due to the two low-frequency metallic A_{1g} modes - the vibration of Ba (120 cm^{-1}) and Cu(2) (150 cm^{-1})

along the c-axis. In the superconducting state there is a sign reversal of the reflectivity change as in the work of Han et al. [51]. The reflectivity change at 40 K is one order of magnitude larger than at room temperature. The oscillatory part remains but the Ba mode gains influence. An important feature of these data is a delayed onset of the reflectivity change, and the maximum of the reflectivity change in the superconducting state occurs when the interband transitions leading to the reflectivity change in the normal state have just relaxed.

These findings were theoretically interpreted by Mazin et al. [60]. The picture they suggest to account for the photoresponse of high-T_c superconductors is the following: Carriers are optically excited from the O2p band to the Cu3d band. They rapidly thermalize with the lattice via emission of incoherent phonons. These phonons break Cooper pairs, which temporarily removes pairing energy. The elastic energy is altered to sustain the energy balance, subsequently a new ionic equilibrium position is obtained and coherent optical phonons are excited since the current ionic positions deviate from the new equilibrium position. The coherent optical phonons show up in the reflectivity data as the dielectric function is determined by the current ionic positions [62]. For this reason, the temporal dependence of the non-oscillating part of the reflectivity is necessarily the same as the temporal dependence of the Cooper pair density.

Probing the high-T_c superconductor by means of optical reflectivity measurements in fact probes dielectric properties, i. e. the entire electron distribution close to the Fermi energy. Conclusions on the Cooper pair density, however, can be drawn only indirectly. Zhao et al. and Li et al. [63,64] used an electronic method to exclusively determine the Cooper pair breaking rate following optical excitation. They used dc biased superconducting stripes that were illuminated by short laser pulses. The laser pulse will break Cooper pairs, decreasing the superconducting carrier density, which in turn increases the kinetic inductance L_{kin} of the superconducting bridge [65]:

$$L_{\mathrm{kin}} = \frac{m\alpha}{e^2}\frac{1}{n_{\mathrm{sc}}}. \tag{2.1}$$

Here, m is the effective mass of the superconducting carriers, n_{SC} is their density, and α is a geometry factor. The change of kinetic inductance gives rise to induction of a voltage:

$$U = I\frac{\mathrm{d}}{\mathrm{d}t}L_{\mathrm{kin}} \tag{2.2}$$

$$= -I\frac{m\alpha}{e^2}\frac{1}{n_{\mathrm{sc}}^2}\frac{\partial n_{\mathrm{sc}}}{\partial t}, \tag{2.3}$$

where it was used that the current is supplied by a current source, i. e. remains constant. Thus, breaking of Cooper pairs corresponds to a positive voltage

transient, recombination corresponds to a negative voltage transient.
Using this direct technique to determine the Cooper pair breaking rate both groups, Zhao et al. and Li et al. found a very sharp resonance at photon energies of about 1.5 eV for $YBa_2Cu_3O_{7-\delta}$. This strong pump photon energy dependence cannot be explained in the simple model of Han et al. [51]. At this point it should be noted that already all optical pump and probe measurements have revealed an extraordinary response around 1.5 eV for $YBa_2Cu_3O_7$ [52,66], however the observed features were spectrally broader. The results of Li et al. are shown in Figure 2.13. The pump pulse fluence of that experiment was 10 μJ/cm^2. They found a resonance triplet structure, with 3 peaks located at

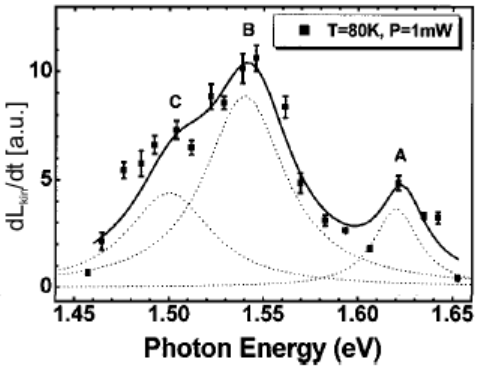

Figure 2.13: Cooper pair breaking rate in dependence on photon energy. Reproduced from [64]

$E_A = 1.62$ eV, $E_B = 1.54$ eV and $E_C = 1.50$ eV. The peak separations can be assigned to reported phonon and magnetic excitation energies. The energy difference between peak B and C is close to the 41 meV peak observed in neutron scattering experiments on Y-Ba-Cu-O systems [67], and the difference between peak A and B can be attributed to the energy of the longitudinal optical bond stretching phonon in the CuO_2 planes (70-80 meV), observed in inelastic neutron scattering experiments on high-T_c superconductors [68]. The sharpness of the peaks cannot be brought in line with the concept of an electronically homogeneous conductor, for which band widths on the order of several hundred meV may be expected. On the other hand such sharp lines are observed for excitonic transitions in semiconductors and insulators. Further support that these structures originate from an insulating region is given from the fact that the position of peak A is slightly below the charge transfer gap energy of insulating $YBa_2Cu_3O_6$. The authors of reference [64] therefore assign peak A to a charge transfer (CT) exciton, which is associated with an electronic transition in which an electron is transferred from one atom to another one, i. e. here

from an oxygen to a copper atom. Li et al. also performed such measurements in oxygen deficient ($T_c \sim 60$ K) and Zn-doped ($T_c \sim 38$ K) Y-Ba-Cu-O samples and found very similar results as for the optimally doped sample concluding that the origin of the triplet structure are the CuO_2 planes. They suggest to explain the data in the frame of the charge stripe model (see also Section 2.1.3): Mobile holes are confined in conducting stripes which are separated by antiferromagnetic domains; pairing originates in the insulating regions [69]. Li et al. argue that any perturbation in the insulating region such as a CT exciton could result in dramatic pair breaking. Their results suggest the presence of such charge stripes over ps time scales.
I want to note, that the results of Li et al. and Zhao et al. can be explained in the frame of the model of Mazin et al. [60] as long as the initial excitation is not restricted to an electronic excitation into the Cu3d band. To the author's understanding the model of Mazin et al. still holds, even though the initial excitation may be a CT-exciton.
Another very important result of these Cooper pair breaking spectroscopy measurements was found by Zhao et al.: They show that only about 1% of the laser energy at the resonance photon energy is used for breaking Cooper pairs [63]. For any measurement that is not exclusively probing the superconducting fraction this means that the effect induced by broken Cooper pairs might be small and could be superimposed by the response of normal carriers.

2.2 $SrTiO_3$

2.2.1 Lattice structure

$SrTiO_3$ has a cubic perovskite structure at room temperature with a lattice constant of $c = 3.9050$ Å [70]. The unit cell is shown in Figure 2.14 (a). At the corners of the unit cell the Sr atoms are located, the Ti atom in the center of the unit cell is surrounded by an oxygen octahedron. At 105 K $SrTiO_3$ undergoes a structural phase transition: The oxygen octahedron begins to rotate around one cubic axis leading to an antiferroelectric distortion and a tetragonal relaxation [71]. The new tetragonal phase is shown in Figure 2.14 (b). The rotational axis forms the tetragonal c axis. Since the oxygen atoms remain on the faces of the unit cell, the a axis is reduced keeping constant the distance between the Ti and the O atom. In turn, the c axis is elongated compared to the cubic lattice constant. The phase transition is of second order, with the angle of rotation of the O octahedron as order parameter. In the low-T tetragonal phase, domains with different orientation of the c axis with respect to the surface occur.

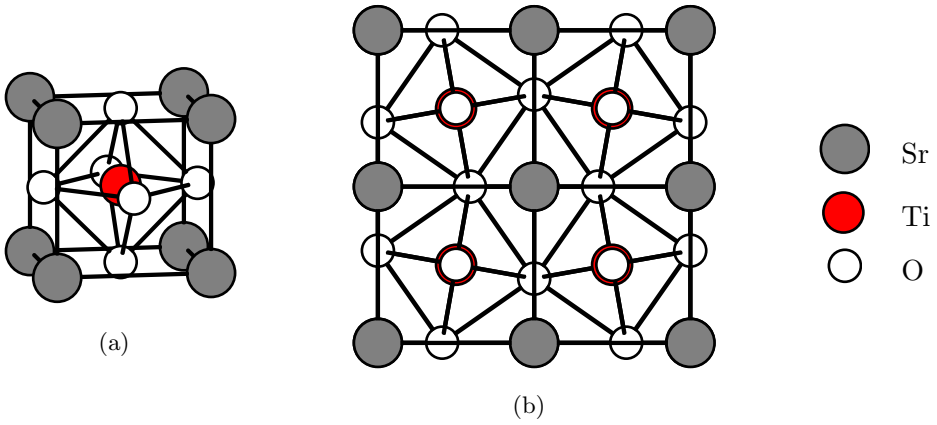

Figure 2.14: Unit cell of $SrTiO_3$ in the high-T cubic phase (a) and low-T tetragonal phase (b).

2.2.2 Properties

$SrTiO_3$ features a variety of outstanding properties. For technical applications its extraordinarily increasing dielectric constant with decreasing temperature plays a very important role. Pure $SrTiO_3$ single crystals exhibit dielectric constants as high as 25000 as temperature approaches zero [72]. A ferroelectric transition as occuring for example in $BaTiO_3$ does not exist at finite temperature. The paraelectric phase is stabilized by quantum fluctuations. However, the ferroelectric transition can be induced by an electric field [73], by uniaxial strain [74] as well as by epitaxial strain [75, 76]. In ref. [76] ferroelectricity was demonstrated in thin $SrTiO_3$ films even at room temperature. Further, at very low temperatures $SrTiO_3$ shows a giant piezoelectric effect [77], which is comparable to the best piezoelectric materials at room temperature.
In [78] coherent optical phonons were optically excited by stimulated Raman scattering and detected by ultrafast polarization spectroscopy. As the atomic displacements involved are due to the oxygen octahedron rotation, an important role of these optical phonons for the present work is not expected.

2.2.3 Epitaxial strain induced thin film behaviour

In his master thesis Lötzsch studied in more detail the structural phase transition of $SrTiO_3$ and how it is influenced by a thin $YBa_2Cu_3O_7$ film [79]. He used a very well characterized $SrTiO_3$ single crystal and studied the evolution of the lattice constants with temperature by means of X-ray diffraction. Afterwards the same sample was covered by a 250 nm thick $YBa_2Cu_3O_7$ film and the measurements of the lattice constants were repeated. Ti-Kα radiation was used: its small extinction depth allows for probing the near-surface region. Lötzsch

observed a different temperature evolution than published so far for the single crystalline, bare $SrTiO_3$. The tetragonal splitting in the low-T phase was found to be significantly larger than reported by others [70, 80, 81], who are insensitive to the near-surface region, but probe the bulk values. Lötzsch explains these deviations by expansive strain due to higher dislocation density close to the surface. When covered with a thin epitaxially grown $YBa_2Cu_3O_7$ film, the rotation of the oxygen octahedra in the near-surface layer is no longer accompanied by a tetragonal relaxation. This is shown in Figure 2.15. The c lattice

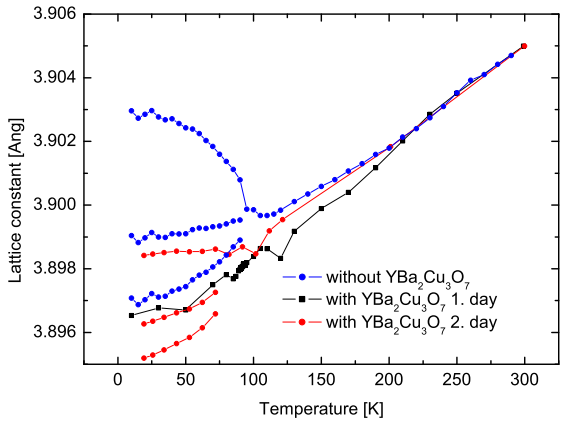

Figure 2.15: The tetragonal relaxation in the structural phase transition in $SrTiO_3$ is initially supressed if the substrate is covered by a thin $YBa_2Cu_3O_7$ film. After repeated heating and cooling tetragonal relaxation is reestablished even though not yet identical with the uncovered case. Taken from Ref. [79].

constant evolves smoothly through the phase transition. Such a behaviour is known from thin $SrTiO_3$ films [82]. It is explained by clamping of the atoms in $SrTiO_3$ by $YBa_2Cu_3O_7$ [79] or, in case of thin $SrTiO_3$ films, by clamping by the substrate [82]. This clamping effect will play a very important role in the interpretation of the data presented in this PhD thesis.

The work of Lötzsch brings forward another very important point: After repeated cooling the tetragonal relaxation of the $SrTiO_3$ covered by a thin $YBa_2Cu_3O_7$ film sets in again [79]. This is explained by reduced clamping due to stress release after several cooling cycles and is also shown in Figure 2.15. Interestingly, the reestablished tetragonal splitting now amounts to bulk values. Lötzsch proposed that the in-plane compressive strain just cancels the expansive strain from dislocations, and thus establishing bulk conditions. This finding is of importance for this work as it shows that the sample may change upon repeated cooling.

3 Experimental and Theoretical methods

3.1 Time-resolved X-ray diffraction technique

The preceeding discussion of temperature dependent lattice properties as well as the response to optical excitation in high-T_c superconductors has shown that the ultrafast lattice response to optical Cooper pair breaking will be very small if present at all. Therefore to study these possible effects an ultrafast probe with very high spatial resolution and very high sensitivity is required. The optical investigations on carrier dynamics (Section 2.1.4) shows that any Cooper pair breaking induced changes occur on time scale of few hundred fs to few ps. Thus, studying such changes require appropriate time resolutions combined with appropriate photon numbers. Currently, only laser plasmas as X-ray sources are suitable.
The spatial and electronic inhomogeneity of $YBa_2Cu_3O_7$ indicates that Cooper pair breaking induced structural changes do not occur on the crystallographic scale and a local probe, such as EXAFS (extended X-ray absorption fine structure) rather than a global probe like X-ray diffraction is more suitable. X-ray absorption spectroscopy requires continuous radiation. A typical X-ray emission spectrum from a laser produced plasma is shown in Figure 3.1. Besides characteristic line radiation the Ti target also emits continuous Bremsstrahlung. However, at the maximum of the Bremsstrahlung emission the number of photons in an energy interval of 70 eV is only about 10% of the photon numbers within the same interval at the peak of the Kα line. Thus, exposure times would be required that are still not practicable considering the present source stability (see Chapter 4). For this reason the X-ray diffraction technique was chosen to investigate the possible fast lattice response to Cooper pair breaking. The possible local changes will be reflected in the diffraction signal as a change of the average structure.

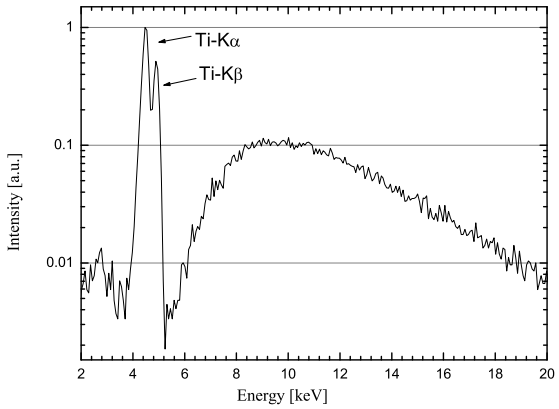

Figure 3.1: Typical emission spectrum from a laser produced X-ray source (here: titanium target) as recorded from the back side of the target. The minimum at energies just above the characteristic line emission is due to absorption in the target.

Sample

$YBa_2Cu_3O_7$ is available as single crystal, thin film and powder and all three kinds would in principle allow for time-resolved X-ray diffraction. The number of diffracted photons per detector area for the powder sample is much smaller than for the other two cases, which require either a very large detector or very long exposure times. On the other hand the detection of many reflections is possible without realignment given a large enough detector. Since the sample has to be cooled at cryogenic temperatures, the need for a large angular range covered by the detector excludes the powder sample so far.
The advantage of the single crystal is the larger number of diffracted photons and the narrower rocking curve width compared to the ones from a thin film. However, the thin film allows matching of pumped and probed volume, as the extinction length of the X-ray pulse is much longer than the absorption length of the optical pump pulse. In this way the ratio of excited–to–probed volume is maximized. Further, the thin film allows an in-situ control of possible damages due to pumping by a resistivity measurement. For these reasons a thin film rather than a single crystal was used for the experiments reported here. The thin film was epitaxially grown onto a $SrTiO_3$ single crystal that provides very good lattice matching.

Pumping conditions

As seen in Section 2.1.4 there is a Cooper pair breaking resonance in $YBa_2Cu_3O_7$ for photon energies of about 1.55 eV. Thus, this is the photon energy of choice. Further, the pump fluence must be chosen as to break as many Cooper pairs as possible. Care should also be given to the finding of Zhao et al., that only 1% of the laser energy is transferred into Cooper pairs [63]. On the other hand, the pump fluence must be chosen low enough as to minimize unwanted excitations.

3.2 Theory of X-ray diffraction

To draw conclusions on the structural properties of the probed volume the X-ray diffraction signal is evaluated theoretically. The measured diffracted signal, i. e. the measured rocking curve is characterized by its angular position, the integrated reflectivity, the width of the rocking curve and its particular shape. It is dependent on the symmetry S of the unit cell, the electron distribution A_j of each atom j in the unit cell, the net plane distance d_{hkl}, the investigated volume V, the real structure of the sample rs, e. g. dislocation density, and properties of the radiation used to acquire the diffraction signal, i. e. wavelength, polarization and divergence of the beam:

$$D = D(S, A_j, d_{hkl}, V, rs, R) \tag{3.1}$$

For fixed radiation properties, the angular position of the rocking curve is given by the net plane distance and the reflection order n according to Bragg's Law: $2d_{hkl}\sin\theta = n\lambda$. Thus, a shift of the rocking curve indicates a modified net plane distance. If the shape of the rocking curve is conserved, the probed volume is homogeneously strained, i. e. the net plane distance is constant. On the other hand, a peak shift and a simultaneous change of the rocking curve shape corresponds to a strain gradient in the probed volume, as would be the case in the presence of acoustic waves for example. These situations are schematically shown in Figure 3.2. The reduction of peak intensity in the presence of a strain gradient (Figure 3.2 (c)) is due to extinction in the volume fraction above the undisturbed part.
The symmetry of the unit cell determines the structure factor $F_h = \sum_j (f_j + if_j^*)\exp[-M_j - 2\pi i\mathbf{h}\cdot\mathbf{r_j}]$, i. e. the amplitude of the electric field scattered by a single unit cell, and thus the peak intensity of the rocking curve. f_j and f_j^* are the real and imaginary parts of the form factor of the atom j, respectively. M_j is the Debye-Waller factor, $\mathbf{h}$ is the reciprocal lattice vector corresponding to the reflection under consideration, and $\mathbf{r_j}$ is the position vector for atom j.

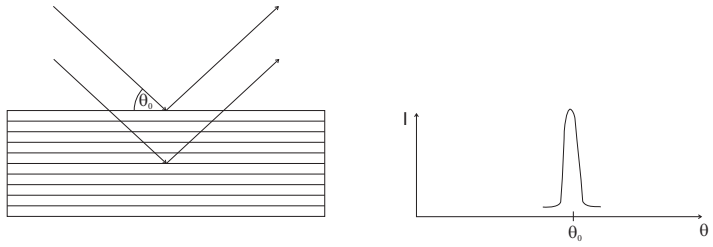

(a) Perfect crystal

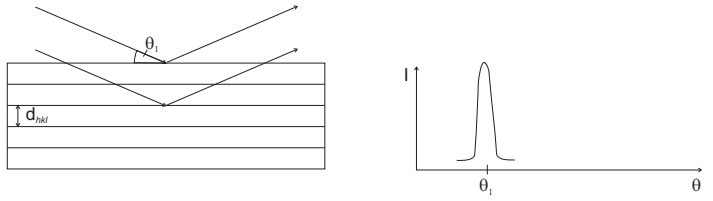

(b) Constant strain

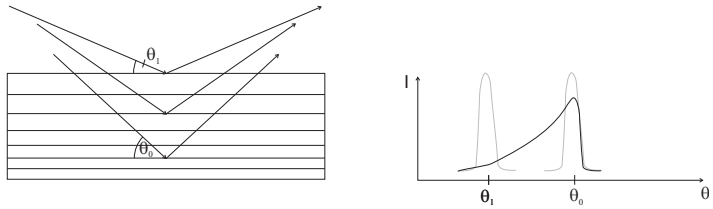

(c) Depth-dependent strain

Figure 3.2: A constant strain shifts the diffraction signal according to Bragg's law without changing the rocking curve shape (b). A depth-dependent strain on the other hand, is reflected in the rocking curve shape.

Modified atomic positions (e. g. due to optical phonons) thus alter the peak intensity accompanied by a slight change of the rocking curve shape. A phase transition may lead to the disappearance of some peaks and to the appearance of others.
The electron distribution of the atoms in the unit cell is contained in the form factor $f_j + i * f_j^*$. Thus, a change in the electronic structure leads also to a modification of the structure factor, however, for relevant reflections these changes are usually marginal. The electron distribution also determines the rocking curve width. As changes in the electronic structure of the atoms usually are due to valence electrons, their influence to the rocking curve shape may be important for light atoms, only.

Depending on the kind of sample there are different approaches to calculate the

intrinsic rocking curves.

1. *Kinematic theory of X-ray diffraction.*
   The kinematic theory of X-ray diffraction assumes that the amplitude of the wave incident on every diffraction center is the same. It neglects the interaction of the wave with the matter, e. g. the extinction of the incident wave due to reflection. Good results are obtained for thin samples or imperfect crystals, i. e. where the extinction length is much larger than the absorption length. For other cases the kinematic theory fails to explain the rocking curve width and peak intensity. The width is simply inversely proportional to the thickness of the sample, and the maximum scales with the square of the thickness.

2. *Dynamical theory of X-ray diffraction.*
   The dynamical theory of X-ray diffraction solves Maxwell's equation within a medium of a complex and periodic refractive index. Contrary to the kinematic theory it also takes into account the interaction of the diffracted wave with the refracted wave, e. g. multiple reflections and interference effects. In its basic form as derived by Laue [83] it is mainly applied to thick, perfect crystals. The results for thin crystals tend asymptotically towards those derived from the kinematic theory. For imperfect crystals different approaches exist. In principle, by knowing the exact strain distribution rocking curves can be calculated using the generalization of the dynamical theory by Takagi and Taupin [84–86].

In the following the methods used in this work to calculate rocking curves are briefly sketched.

3.2.1 $YBa_2Cu_3O_7$

From the experimental data in Section 6.1 it will be seen, that only the peak intensity of the $YBa_2Cu_3O_7$ thin film rocking curve has changed. This indicates a modified structure factor F_h. As the $YBa_2Cu_3O_7$ is present as thin film, the kinematic theory of X-ray diffraction is appropriate to model the rocking curve. The integrated reflectivity for an absorbing crystal that is larger than the X-ray beam, as in the present case, is given by [87]

$$R_{\mathrm{int}} = \frac{\lambda^3 R^2 C}{\sin 2\theta_B} \frac{1}{V^2} \frac{1}{2\mu} |F_h|^2 \left[1 - \exp\left(-\frac{2\mu t}{\sin\theta_B}\right)\right] \propto |F_h|^2 \qquad (3.2)$$

where λ is the X-ray wavelength, R is the classical radius of the electron, θ_B is the Bragg angle, V is the volume of the unit cell, μ is the absorption coefficient

and t is the thickness of the crystal. The polarization factor C is given by

$$C = \begin{cases} 1 & \text{for} \quad \sigma - \text{polarization} \\ \cos 2\theta & \text{for} \quad \pi - \text{polarization} \end{cases} .$$

To model the changes in the $YBa_2Cu_3O_7$ rocking curve, the ideal atomic positions in the unit cell were modified and the resultant integrated reflectivity is compared with the undisturbed value. The ratio of disturbed to undisturbed value is then compared with the measured reflectivity change.

3.2.2 $SrTiO_3$

As the $SrTiO_3$ substrate is a thick single crystal and changes in the rocking curve shape have to be explained (see Section 6.2) the dynamical theory of X-ray diffraction has to be applied. A brief introduction to the equations of interest is found in Appendix A. The basic equations of the dynamical theory of X-ray diffraction (see eq. (A.5) and (A.6)) are solved by splitting the crystal in thin laminae of thickness ΔA with piecewise constant strain as suggested by Wark et al. [88]. The strain is introduced in the basic equations by allowing the Bragg angle to vary with depth. The diffracted amplitude at depth A is found recursively in terms of that at depth $A_0 = A - \Delta A$: As boundary condition it is used that the reflected amplitude at the back side of the crystal is 0 and iteration is done to the front side (diffracting surface). The pseudocode for calculating the rocking curve, i. e. the angular intensity distribution at the front side of the crystal, is sketched in Figure 3.3. Firstly, for a given time

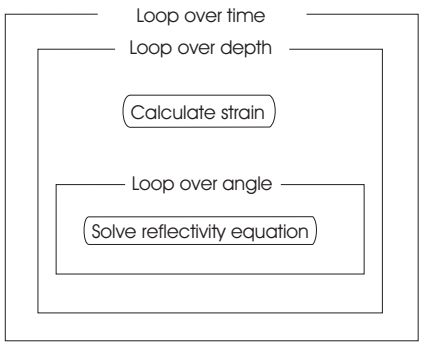

Figure 3.3: Pseudocode to solve the basic equations of dynamical theory of X-ray diffraction.

point the depth-dependent strain is calculated which serves as input to the depth-dependent Bragg angle. Afterwards the loops over depth and angle are executed. Using this method one obtains time dependent rocking curves that can be compared with the measured ones.

4 Time-Resolved X-ray diffraction

A very powerful tool to investigate crystalline structures on a sub-ps time scale is time resolved X-ray diffraction in the pump-probe scheme. Such experiments require, besides an ultrashort pump pulse, either a very fast X-ray detector, such as an X-ray streak camera or a very short X-ray probe pulse. The fastest X-ray streak cameras currently available provide sub-ps time-resolutions [89,90]. Sub-ps keV X-ray pulses are provided by several experimental schemes. Among these are laser produced plasmas [7], the fs-slicing method with synchrotron radiation [91], high harmonic radiation [92] and relativistic Thomson scattering [93]. Different physical aims favour special source parameters, e. g. for powder diffraction experiments the number of photons per solid angle and per time are the most important parameters. The experiments reported here were performed at a laser produced plasma source. This kind of source together with an appropriate X-ray optic allows for very sensitive measurements of variations of lattice constants and changes in the rocking curve profile on sub-ps time scales.

4.1 Experimental setup

The experiments were performed at the JETI (Jenaer multi-TW Ti:Sapphire) laser system [94]. In three amplification stages the 800 nm laser pulse is amplified up to 1.3 J, the laser pulse duration is recompressed to about 80 fs. The pulse can be focused down to $5\,\mu\mathrm{m}^2$. For these experiments laser pulse energies of about 500 mJ were used. The schematic experimental setup is shown in Figure 4.1. The laser pulses were split by a 90:10 beam splitter *(BS)*. The more intense part was focused by an off-axis parabola *(P)* onto a 25 μm thick titanium tape target *(T)* and created a hot plasma. The incidence angle of the laser pulse was about 30°. Electrons are accelerated by the laser field into the target where their interaction with the target atoms gives rise to production of characteristic X-radiation as well as bremsstrahlung [95]. The Kα emission is isotropic. Therefore radiation emitted from the front side of the target as well as that emitted from the back side can be used. Spatial constraints as well as the advantage to be insensitive to temporal jitter due to eventual target

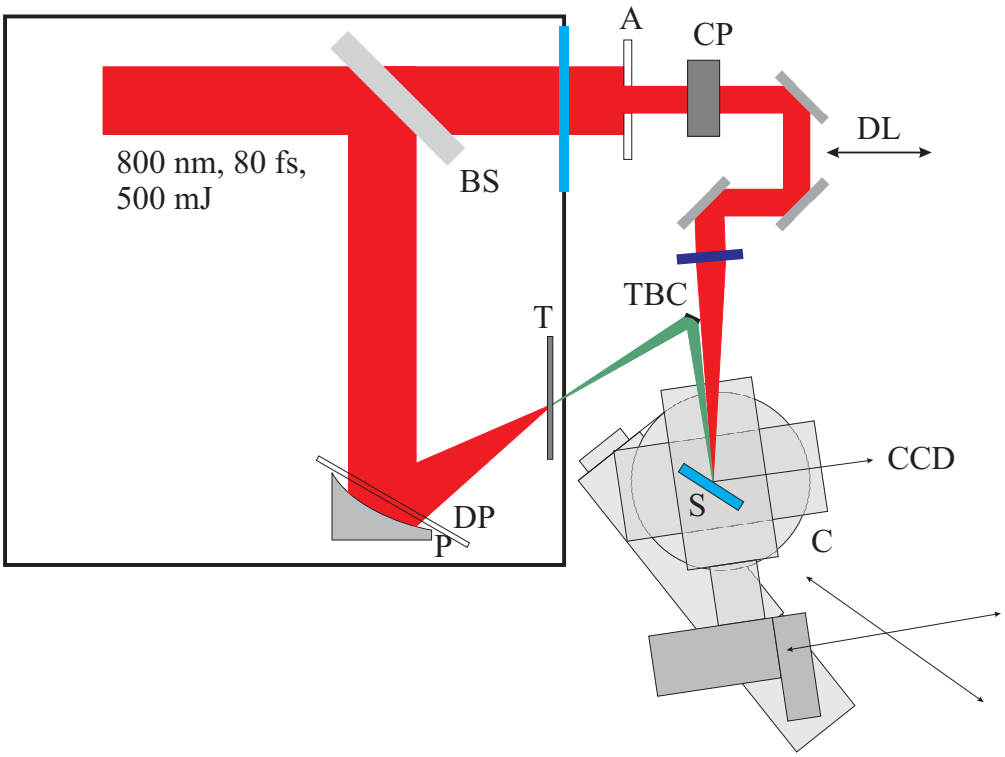

Figure 4.1: Experimental setup for the optical pump X-ray probe experiment.

movements convinced us to choose the X-rays coming from the back side. This setup allows to assemble large part of the experiment outside the target chamber and thus an easier realignment of certain components is possible. Part of the emitted radiation is refocused and monochromatized by a toroidally bent GaAs(100) crystal *(TBC)*. To minimize the losses due to photon absorption in air, the crystal optic as well as a large part of the X-ray path was also put in a vacuum chamber not shown in Figure 4.1. This vacuum chamber was connected to the target chamber, where the main pulse is focused to produce the hot plasma. The bent crystal images the X-ray plasma source monochromatically onto the sample *(S)* which is placed in the cryostat *(C)*, in turn positioned on a Huber goniometer. As the sample is structured (see Section 4.4) it is important to allow for a variation of the focal position on the sample. This is also necessary in case of damages. For this reason two independent translation stages are mounted under the sample's goniometer. The vacuum system of the cryostat was decoupled from the target and crystal chamber. The X-rays leave the crystal chamber through a kapton window (50 μm thick) and enter the vacuum system of the cooler through a beryllium window (100 μm thick). The diffracted radiation was detected by a deep depletion CCD camera [96],

which is positioned 12 cm behind the sample. Since the production of a hot plasma with lasers is always connected with the production of debris, the off axis parabola is protected by a thin coplanar fused silica plate *(DP)*, which can be exchanged and cleaned when the losses become too high.
The second, weaker pulse is attenuated by an aperture *(A)* and two crossed polarizers *(CP)* to minimize excitations not due to Cooper pair breaking. A delay line *(DL)* allows to vary the temporal delay between this optical pump and the X-ray probe pulse in steps smaller than 10 fs. The pump pulse is then focused by a lense onto the portion of the sample probed by the X-ray pulse. The difference in angle of incidence between the pump and probe beam on the sample is about 5°. The temporal overlap between pump and probe pulse is adjusted by means of an cross-correlation measurement. The alignment was done as follows:

1. Without moving the tape target several laser pulses are focused on to the tape in order to produce a hole. The main laser pulse can thus go through the target, is reflected by the GaAs crystal and (ideally) focused on to the portion of the sample probed by the X-rays. As will be discussed in Section 4.3 the crystal, in fact, is slightly miscut, i. e. the lattice planes are not exactly parallel to the crystal surface. This leads to a separation of optical and X-ray focus. However, as shown in Section 4.3 the size of this effect is well known and the alignment is corrected for. The sample is positioned in the focus of the bent crystal by the two translation stages.

2. Both laser pulses (strongly attenuated to prevent damage by the main pulse) are then spatially overlapped on the sample. Here, the separation of optical and X-ray focus of the GaAs crystal is accounted for and the pump pulse is chosen to be large enough to ensure a spatial overlap also for the optical pump and the X-ray probe pulse.

3. The cryostat is moved away by the help of the translation stages.

4. A non-linear crystal (BBO) is put in the focus of the bent crystal. Both beams are spatially overlapping here, each of them generating second harmonic beams which are spatially separated on a piece of paper behind the BBO crystal due to the different directions of pump and probe pulse.

5. The delay between pump and probe pulse is varied, until a third second harmonic signal exactly in between the first two signals appears. This signal is due to photon mixing between the two pulses and therefore shows up only if the temporal overlap between both pulses is established.

6. Due to the finite pulse length of the two pulses, the third signal occurs for a range of different delays. The "0" position is defined as the center of that range.

7. The BBO crystal is again replaced by the cryostat.

As the alignment of the temporal overlap involves many steps and experimental rearrangements, the experimental uncertainty of the "0" delay is not better than ± 700 fs.

4.2 The target

As mentioned in Section 4.1, the target system used was a Titanium tape target. The thickness of the tape was 25 μm, the width was 5 cm and the length was chosen long enough to ensure that a replacement of the tape was not necessary during an experimental campaign. A picture of the tape target is shown in Figure 4.2. The tape is rolled up on two coils, each of them can be moved by

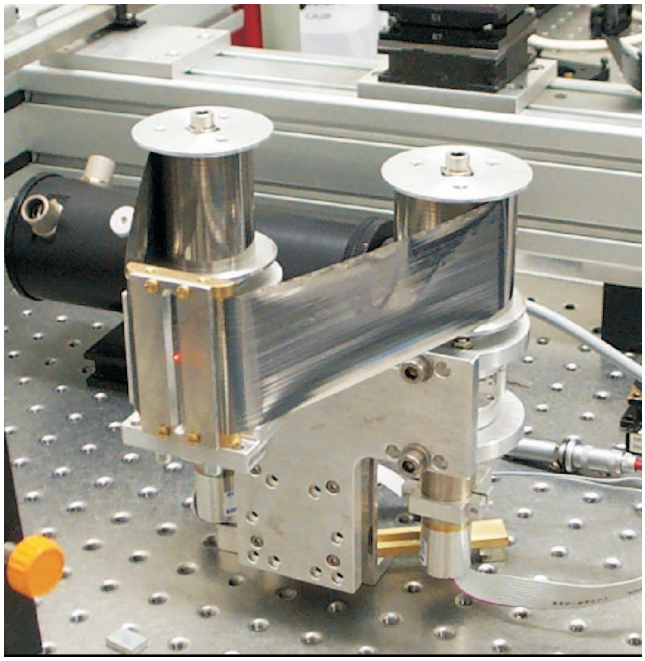

Figure 4.2: Tape target system used in the experiment.

dc motors. The motors move with a velocity of about 1 mm/s providing a new fresh target surface for every shot at the repetition rate of 10 Hz. The tape target is constructed in such a way that it automatically reverses the direction as soon as one coil is empty. Once the direction is reversed, a stepping motor

translates the target system by a given amount in order to provide a new track to the following laser pulses.
The position of the target in the focal plane is fixed: A guide made of two metal plates gives the needed stability. In the plates a slit is left open for the laser and the X-rays. The spacing of the two plates is fixed to be 3 times the tape thickness, i. e. 75 μm. Therefore, this is also an upper allowed value for the target movement in focus direction. However, as detailed investigations using a microscope have shown, the target plane changes by not more than about 20 μm while moving.
The slits in the plates were optimized to provide a good tape shot-to-shot stability and at the same time a sufficient long-term stability. The latter one is limited by debris from the tape accumulated in the slit which may displace the target from the focal plane.
Recently, the stability of the target system could be increased by using a thinner titanium tape.

4.3 The X-ray optic

In principle time-resolved X-ray diffraction experiments at laser produced plasmas in optical pump – X-ray probe scheme can be performed with and without an appropriate X-ray optic. Both methods were demonstrated to work [2, 3, 5, 6, 8, 9, 97]. The setups for either case are shown in Figure 4.3.
The main difference is that the X-ray optic serves as monochromator. This has a deep impact in the experiment:

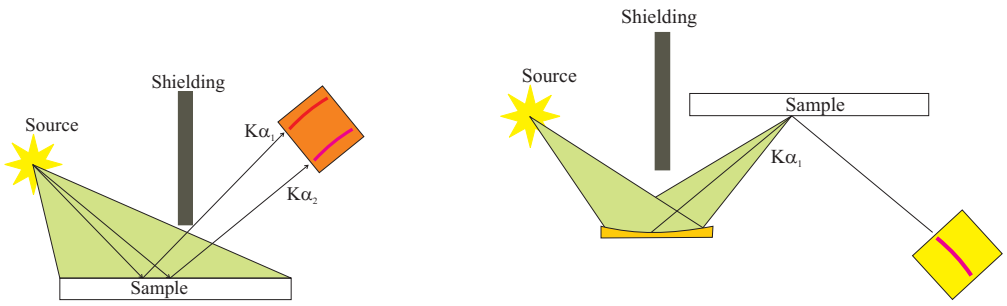

(a) Without X-ray optic (b) With X-ray optic

Figure 4.3: Schematic experimental setup with and without X-ray optic.

1. The position of the diffracted signal on the detector is directly determined by the double Bragg angle 2θ. For polychromatic radiation and in presence of several different lattice spacings the data analysis is more

complicated, since different lattice spacings can diffract X-rays of different wavelengths to the same point on the detector. In turn, with an appropriate crystal optic a wavelength interval is diffracted, that can be much narrower than the characteristic line width. A summary of effects limiting the achievable resolution for a toroidally bent GaAs crystal is shown in Table 4.1. The rocking curve width is much smaller than the Kα_1 linewidth, thus only a fraction of the line is reflected. Broadening occurs due to a finite source size and the spectral broadening due to deviation from Bragg angle over the bent crystal surface $\sigma = \frac{x^2}{8l_a^2 \tan\theta_0}$ [98]. However it is seen, that these broadening effects are smaller than the intrinsic rocking curve and much smaller than the Kα_1 linewidth, i. e. they do not lead to a significant broadening. The limiting factor of the resolution for X-ray optics making use of multilayers or capillaries for example is the X-ray linewidth.

2. For the monochromatic case, the background on the detector is reduced. This is mainly due to the fact that the channels for secondary production of X-rays in the sample, such as fluorescence radiation, are reduced. Other sources of secondary X-ray emission than the sample can easily be shielded.

In case that an X-ray optic is used, also different setups are imaginable. Shown in Figure 4.3 is the case of a point-to-point image, where the sample is placed in the focus of the optic. This has the advantage that there is no mapping between the incident angle and the position on the sample. Instead, in one point (the focus) a whole range of incident angles is provided according to the opening angle of the optic. This means, that for a possible change of lattice constant due to the excitation, the intense characteristic radiation is diffracted by the same portion of the sample as in the unexcited case. This makes the

Broadening effect		Size of the effect $\Delta\theta/\tan\theta$
Rocking curve width	GaAs 400, Ti-Kα_1	$6.2 \cdot 10^{-5}$
X-ray line width	Ti-Kα_1	$3 \cdot 10^{-4}$
Finite source size	FWHM = 50 μm	$3.1 \cdot 10^{-5}$
Spectral broadening σ	Crystal width = 15 mm	$1.0 \cdot 10^{-5}$

Table 4.1: Broadening effects for the GaAs toroidally bent crystal used for the present study. As the X-ray line width is much larger than all other contributing effects, only a fraction of the line is reflected allowing for very high sensitivity measurements of changes of the Bragg angle or the shape of the rocking curve.

experiment independent of the real structure of the crystal: In case of the presence of grain boundaries or dislocations a change of lattice parameters might shift the probed volume on another grain which can intrinsically have a different reflecting power. Thus, an experiment, for which the probed volume is an extended region depends on very high quality samples and is though restricted to few materials.
Imaging the source onto the sample has another very important advantage: The temporal profile of the X-ray pulse is approximately conserved, while in the absence of an X-ray optic different positions on the sample correspond to different transit times between source and sample.
Usually, time resolved X-ray diffraction experiments at currently available table top fs-laser produced plasmas suffer from a lack of photons on the CCD which reduces the sensitivity with which changes in the structure of the sample can be measured. To increase the sensitivity it is important that a substantial part of the probed volume is also pumped and that the pumping conditions in the pumped volume are (nearly) only a function of depth. By using an X-ray optic with the sample put in the focus, these conditions are easily fulfilled: In general, the pump spot can be chosen larger in size than the X-ray focal spot.
On the other hand, there is also a good reason for some experiments to be performed without an X-ray optic. This is because of the need for normalization: Up to now, the emission of characteristic X-radiation from laser produced plasmas does not feature the long-term stability as for example known from an X-ray tube. The reasons are:

1. The instability of the driving laser pulse. The pulse to pulse instability of Jena TW Ti:sapphire high power laser system is in the range of 3% (rms). As the electron acceleration in the laser plasma, and thus the Kα production is a highly non-linear process, small variations in the laser energy can result in large fluctuations of X-ray photon numbers.

2. The instability of the target. A variation of the laser focus size has dramatic influence on the X-ray emission. Much work was spent to optimize the stability of high repetitive targets for the production of characteristic X-radiation.

3. The temporal decrease of laser intensity due to debris. As a hot plasma is produced by a laser pulse, matter is not only highly ionized, but whole clusters of ions are blasted away and the plasma serves as a sputter system. This debris destroys the focusing laser optics which therefore have to be protected by an appropriate debris protection. In the experiments here, a thin quartz glass plate in front of the off-axis parabola is used.

Obviously, the transparency of that quartz plate decreases with time. This is the main reason for the decrease of X-ray photon numbers with time. Currently, much effort is spent to develop a debris protection that provides temporally independent focussing conditions, i. e. a tape-type system.

A normalization is necessary if one is interested in reflecting powers and not only in the line shapes and Bragg angles. It can be realized in different manners: If no X-ray optic is used, the probed but not pumped volume can be used for normalization. This has the advantage that the plasma conditions for the pumped and unpumped signals are definitely the same. If there is an X-ray optic present in the experiment and the sample is put in its focus, there are, in principle, three ways for a normalization:

1. The use of a second crystal (flat or bent) that will not be excited. The use of a flat crystal has the previously discussed disadvantages of reflecting many wavelength and therefore increasing the noise on the detector. The use of a bent crystal has the disadvantage that for large sources it might not image the same fraction of the source as the first bent crystal. Plasma instabilities can lead to uncorrelated signals in both regions.

2. For thin film samples, a substrate reflection can be used for normalization, in case that no changes in the substrate can occur.

3. Diffraction images from the sample can be recorded, when the pump pulse is blocked. This has the disadvantage, that the plasma conditions for pumped and unpumped exposures can be different.

In the present case the last two options were used to normalize the diffracted signal.

The choice of an appropriate X-ray optic

Bargheer et al. [99] compare four different X-ray optics for fs-X-ray diffraction experiments: A toroidally bent crystal, a multilayer optic, an ellipsoidal capillary and a poly-capillary. They characterized them in terms of focal spot size, photon flux, angular flux density, flux density, suppression of other wavelengths and temporal broadening. Depending on specific experimental demands any of these optics have special features that makes them favourable for a special experiment. For example, if one is interested in reflectivity changes only, the X-ray optic with highest photon flux will be the first choice, irrespective of the fact that the focal spot size might be huge compared to the X-ray source size and

that a whole bunch of wavelengths is used. Then, a multicapillary optic or an elliptical HOPG (*highly oriented pyrolytic graphite*) optic [100] are best choice. On the other hand, if one is interested in tiny changes of the lattice parameters a very high sensitivity to any shift of the rocking curve will be required, and the optic of choice will be a crystal optic or maybe a multilayer optic which both provide small focal spot sizes and, even more important, very high monochromaticity. The reflection curve of a crystal optic can be even much narrower than the Kα_1 linewidth, while a mulitlayer optic will reflect both, Kα_1 and Kα_2 radiation. For studying sub-ps lattice dynamics the temporal broadening of the X-ray pulse in the X-ray optic might be an issue. The broadening in bent crystals is due to path length differences between the radiation reflected from the surface and the radiation reflected in a finite depth of the optic. Thus, the parameter determining the temporal broadening is the penetration depth (together with the Bragg angle). For a toroidally bent GaAs crystal and Ti-Kα radiation the temporal broadening is readily estimated: the penetration depth t of Ti-Kα in a bent GaAs(100) crystal with bending radius of about 400 mm and for the 400 reflection is about 2 μm [101]. As shown in Figure 4.4 the temporal broadening is given by:

$$\Delta\tau \quad = \quad \frac{2t}{c \cdot \sin\theta} \approx 10\,\text{fs.},$$

where c is the velocity of light. The duration of the X-ray pulses from fs-laser produced plasmas could not be measured directly up to now. An estimation is given by the fastest transient structures measured in time-resolved X-ray diffraction. Sokolowski-Tinten et al. have studied the ultrafast melting in a thin crystalline Germanium layer. From their results they infer an upper limit for the X-ray pulse duration of about 300 fs [6]. The broadening is therefore

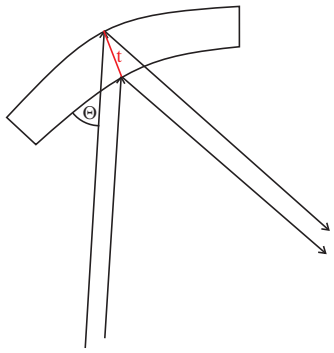

Figure 4.4: The temporal broadening can be estimated by the path length difference between radiation reflected from the surface and the radiation reflected at the penetration depth t.

much smaller than the expected pulse duration and can thus be neglected.
Changes in the crystal structure of High-temperature superconductors due to breaking of Cooper pairs, if present at all, will be very small. Thus an experimental setup has to be chosen that provides very high sensitivity to any change in the crystal structure. From optical pump and probe measurements [51,61] it is known that Cooper pairs break on time scales of few hundred fs and recover on time scales of few ps. The sample studied is a thin $YBa_2Cu_3O_7$ film on a $SrTiO_3$ substrate (see section 4.4). Since the observed $YBa_2Cu_3O_7$ 006 reflection is very close to the $SrTiO_3$ 002 reflection for the success of the experiment it is crucial to separate Kα_1 from Kα_2 radiation. These considerations favour a toroidally bent crystal as X-ray optic.
To optimize the feasibility of the X-ray optic in terms of photon flux it was examined how the range of well established toroidal crystal optics can be extended to other crystal materials [102]. The fabrication procedure for toroidally bent crystals is described in [103]. The demand for a very narrow reflection curve, for high peak reflectivity and for very small focal spot sizes limits the number of possible materials to those with very high crystalline quality (such as silicon, quartz and germanium). For elastical bending the crystals must be available as very thin crystal plates. Typical thicknesses are of the order of 80 μm. Further, for optimum focusing properties, the orientation deviation of the crystal plate must be minimal. Such thin crystal plates with the desired properties are not readily available. In the X-ray optics group in Jena there is experience in preparing thin silicon or quartz plates, and many X-ray optics using these types of crystal were proven to work excellently [1, 5, 8, 10, 104–110]. However, to maximize the reflectivity one wishes to go to higher Z materials, such as Ge or GaAs. While no thin Ge plates with the desired properties were available, industrially manufactured thin GaAs plates met the requirements for the X-ray optic, which was then manufactured in the X-ray optics group as described above. The disadvantage of GaAs crystals is that they hardly come free of dislocations. A comparison between the well established Si(311) and the new GaAs(400) crystal optic is shown in Table 4.2 [102]. The distances between source and crystal and between crystal and focus for the GaAs crystal were chosen significantly larger than for the silicon crystal. One reason is the higher Bragg angle and a minimum distance between source and focus required for the experiment. While previous experiments where performed with the Si 311 optic in air (to simplify experimental work), the longer pathlength necessary for the GaAs 400 optic allows for an easy evacuation (without significant experimental constraints) of the whole X-ray path length and therefore reduction of photoabsorption. For a comparison of the two optics the transmission from

Crystal & reflection	Si 311	GaAs 400
Horizontal bending radius R_h [mm]	149.83	400.00
Vertical bending radius R_v [mm]	105.62	378.52
Crystal width x_h [mm]	11	15
Crystal height x_v [mm]	11	40
Bragg angle θ	57.1°	76.6°
Asymmetry angle	0°	0°
Distance source–crystal [mm]	125.8	389.11
Distance crystal–focus [mm]	125.8	389.11
Distance source–focus [mm]	136.66	180.35
$R_{\mathrm{int}} \cot\theta$ [mrad]	17.49	58.60
Vertical opening angle	5.0°	5.9°
Transmission source–focus	0.29	0.78

Table 4.2: Comparison between a commonly used Si 311 crystal optic and the newly developed GaAs 400 optic.

the source to the focus must therefore be included. For an experimental setup with the Si 311 optic about 17 cm of the X-ray path is at atmospheric pressure. Between the crystal and the plasma source there is a beryllium window of 100 μm thickness. The transmission of Ti-Kα radiation is therefore 0.29. In case of the GaAs 400 optic, the whole path length can, in principle, be evacuated. However, an experimental setup must include at least one X-ray window which would be a 50 μm thick kapton foil. The transmission through this window for Ti-Kα radiation is 0.78. A measure for the number of photons on the sample is the product of $R_{\mathrm{int}} \cdot \cot\theta$ with the vertical opening angle and the transmission between the source and the focus of the optic. In case of the GaAs 400 optic this product, and thus the number of photons, is 10.6 times higher than in case of Si 311, which is a very important improvement for the experiment.

Characterization of the toroidally bent crystal

Figure 4.5 schematically shows how a toroidally bent crystal is used in X-ray diffraction experiments. The demand for a point to point image is fulfilled if the vertical and horizontal foci lie in the same position, i. e. the horizontal focal length f_h and the vertical focal length f_v are equal [98]

$$f_h \quad = \quad f_v$$

with

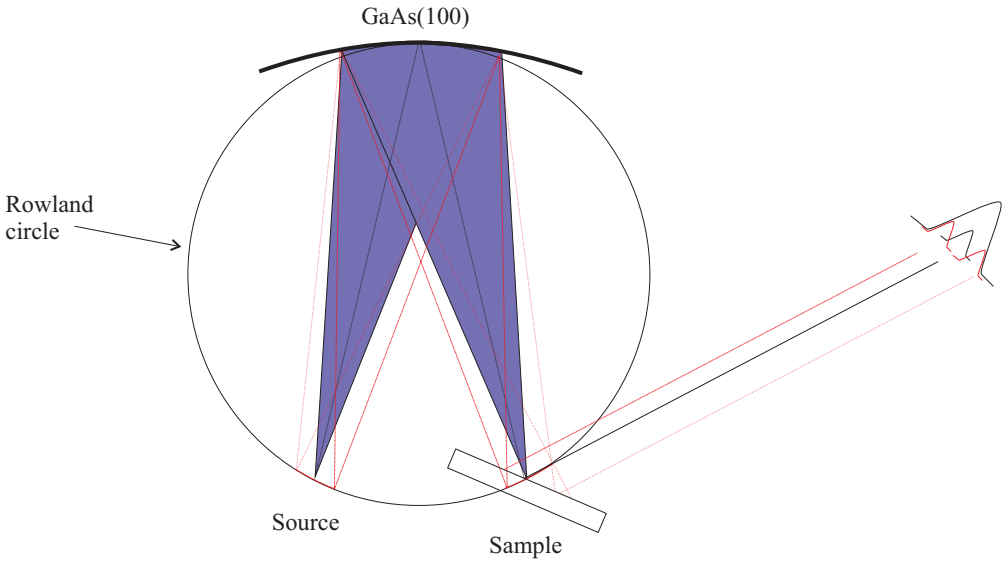

Figure 4.5: Functionality of a toroidally bent crystal optic for X-ray diffraction experiments. If the source is located on the Rowland circle the quasi-monochromatic two-dimensional image will be found again on the Rowland circle. The sample which is put in the focus of the bent crystal will Bragg reflect part of the incident radiation with a much smaller divergence. A finite source size will broaden the focus and thus the measured rocking curve width.

$$\begin{aligned} f_h &= \frac{R_h}{2}\sin\Theta \\ f_v &= \frac{R_v}{2\sin\Theta}. \end{aligned}$$

A given horizontal bending radius R_h thus fixes the vertical bending radius R_v for a given Bragg angle Θ:

$$\sin^2\Theta = \frac{R_v}{R_h} \tag{4.1}$$

A 1:1 image is obtained with source and image placed on the Rowland circle. Broadening effects are due to a finite source size and geometrical deviations. The detailed rocking curve is dependent on wavelength, crystal structure, crystal reflection, bending radius, geometry of reflection (Bragg or Laue, symmetric or asymmetric) and the crystal perfection. The computer code DIXI [111] computes the rocking curve for an arbitrary crystal setup. In Figure 4.6 such a theoretical rocking curve is shown for a GaAs (400) reflection of Ti-Kα radiation. The bending radii for the toroidal crystal were chosen as in the experiment:

$$\begin{aligned} R_h &= 401.47\,\text{mm} \\ R_v &= 390.54\,\text{mm}. \end{aligned}$$

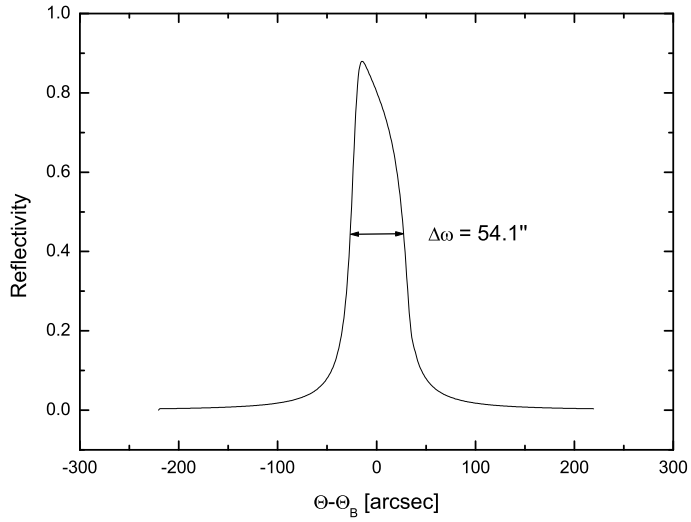

Figure 4.6: Intrinsic Rocking curve for 004 reflection from the toroidally bent GaAs crystal.

It was assumed that the crystal is a perfect single crystal. Thus, any dislocations were neglected. Dislocations or any other crystal defects lead to a broadening of the rocking curve. However as Galler has shown in his diploma thesis, for the given dislocation density a broadening of not more than 4% is expected [112].
To investigate the role of a finite source size on the focus of the bent crystal ray tracing calculations were performed. An X-ray source size of 50 μm full width at half maximum (FWHM) was used for the calculation which is in agreement with the measurements of Reich et al. [110] ($\sim 70\,\mu$m). From the Bragg angle of the 400 reflection of GaAs $\theta = 76.6°$ and equation (4.1) applied to the measured radii of curvature it can be seen, that the curvatures of the crystal are not ideally fitting to the reflection for a point to point imaging. This geometrical deviation is due to manufacturing imperfections. The calculations were performed for both the ideal case and the realistic case. The results of the calculations are shown in Figure 4.7. For the ideal bending radii the focal spot diameter is given by the finite source size. Other broadening effects can be neglected. For the real bending radii the geometrical deviation from the ideal form broadens the focal spot additionally.
The focal size of the bent crystal was also determined experimentally. A focal series is shown in Figure 4.8. The effect of the geometrical deviations is clearly seen: There is not just one point-focus, but scanning the camera through the focus reveals an astigmatism. For the experiment only the dimension in the

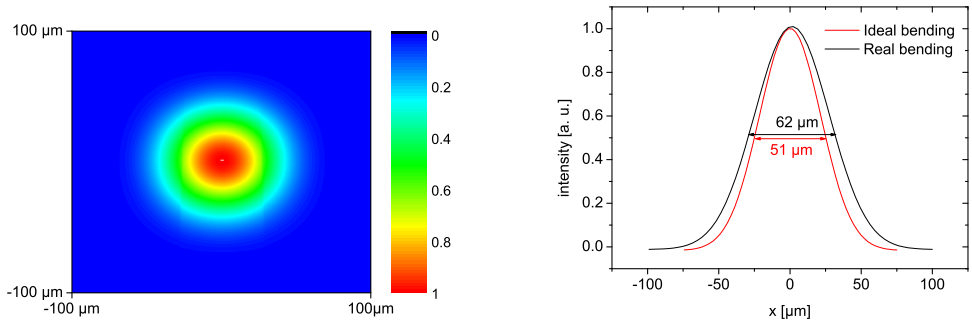

Figure 4.7: Simulated focal spot of the GaAs 400 toroidally bent crystal with bending radii as used in the experiment (left). An X-ray source with a FWHM = 50 μm was assumed. In the right Figure the lineout is compared to the case where geometrical deviations from the ideal crystal form are not present.

dispersion plane, i. e. the horizontal width, is crucial. This is because the sample is structured meander-like (see Section 4.4). The measured horizontal focus is about 100-120 μm in diameter (FWHM). Differences to the focus estimated by ray tracing are certainly due to different X-ray source sizes and due to the imperfections of the crystal as well as a small miscut. A miscut of the thin crystal plate will lead not only to a larger focal size, but also to a shift of the focal position with respect to the optical focus given by the crystal surface. The knowledge of the size of this effect is crucial as otherwise the spatial overlap of pump and probe pulse adjusted optically may not be established for the X-ray probe pulse. The focal shift was carefully diagnosed by an imaging test: A mesh with 100 μm lattice constant was imaged optically and with Ti-Kα radiation by the bent crystal. The position of the image was measured with respect to the position of a fixed needle. The result is shown in Figure 4.9. The X-ray image is shown twice to estimate the horizontal and vertical focal shift more easily. The mesh is well imaged by light as well as X-rays. However there is a miscut, i. e. the lattice planes are not perfectly parallel to the crystal surface, becoming

(a) -10 mm (b) -3 mm (c) focus (d) +3 mm (e) +10 mm

Figure 4.8: Focal spot of the bent crystal in dependence of the detector position.

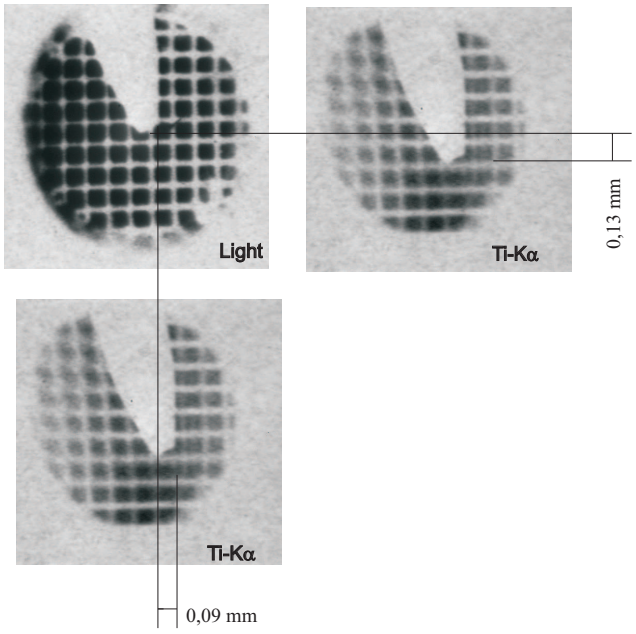

Figure 4.9: Imaging test of the GaAs bent crystal optic used in the time-resolved X-ray diffraction experiment.

manifest in a relative shift between imaged mesh and needle compared to the optical image. The focus shifts by about 100 μm in both direction. Even though this shift is quite large, the associated miscut is rather small. In the dispersion plane the miscut is 0.23 mrad, perpendicular to the dispersion plane it amounts to 0.33 mrad. Due to the large bending radii these tiny misorientations lead to the large observed shifts. Without the accurate determination of the miscut the pump-probe experiment would have been impossible.

4.4 The sample

As sample an optimally doped $YBa_2Cu_3O_7$ thin film (250 nm) on a thick $SrTiO_3$ substrate was used. The lattice parameters of $YBa_2Cu_3O_7$ are $a = 3.8227$ Å, $b = 3.8872$ Å and $c = 11.6802$ Å at room temperature [18]. The space group of $YBa_2Cu_3O_7$ is *Pmmm* (no. 47) [13]. Besides (maybe) the O(1) atom, the atoms in $YBa_2Cu_3O_7$ occupy Wyckoff positions where only the z-coordinates are variable (see Table 4.3). Therefore without a phase transition ionic displacements are allowed in c-direction only. Only ions not sitting on highly symmetric sites may be displaced. It is therefore tempting to study the c-axis response

Ion	Position	Coordinates	
Ba	$2t$	(0.5, 0.5, z)	(0.5, 0.5, $\overline{z}$)
Cu(2)	$2q$	(0, 0, z)	(0, 0, $\overline{z}$)
O(1)	$1e$	(0, 0.5, 0)	
alternative:	$2k$	(x, 0.5, 0)	($\overline{x}$, 0.5 ,0)
O(2)	$2s$	(0.5, 0, z)	(0.5, 0, $\overline{z}$)
O(3)	$2r$	(0, 0.5, z)	(0. 0.5, $\overline{z}$)
O(4)	$2q$	(0, 0, z)	(0, 0, $\overline{z}$)

Table 4.3: Wyckoff positions occupied by the atoms in the $YBa_2Cu_3O_7$ unit cell. For the notation of the atoms see Figure 2.1. Only atoms not occupying highly symmetric sites are listed.

even though superconductivity is known to be a 2 dimensional phenomenon being associated with the *ab* plane.

The lattice parameter of $SrTiO_3$ in the cubic phase at 300 K is $c = 3.9050$ Å [113] and is therefore well suited as substrate for epitaxial growth of $YBa_2Cu_3O_7$. Both the film and the substrate were *c*-oriented. This can be seen in the $\omega/2\theta$ scan, shown in Figure 4.10. Only $00l$ reflections show up. $YBa_2Cu_3O_7$ $0\,0\,3l$ reflections are superposed by the substrate's $00l$ reflections.

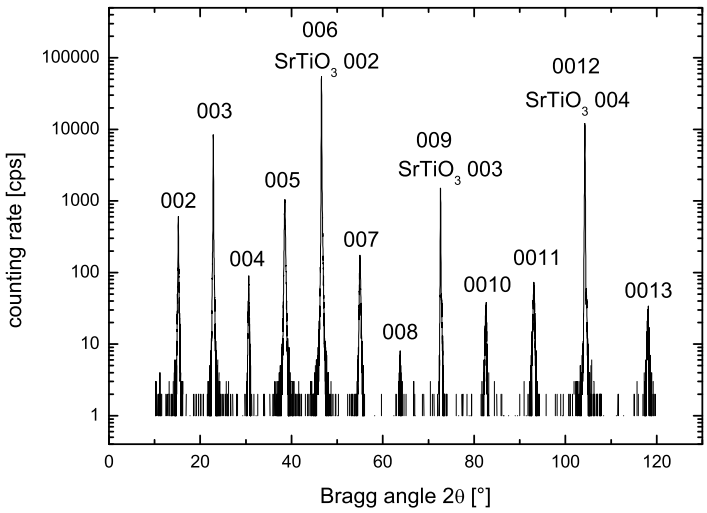

Figure 4.10: Overview $\omega/2\theta$ scan of a typical $YBa_2Cu_3O_7/SrTiO_3$ sample. Only $00l$ reflections of $YBa_2Cu_3O_7$ and $SrTiO_3$ show up, proving the *c*-orientation of the sample and the appearence of a single phase in the thin film.

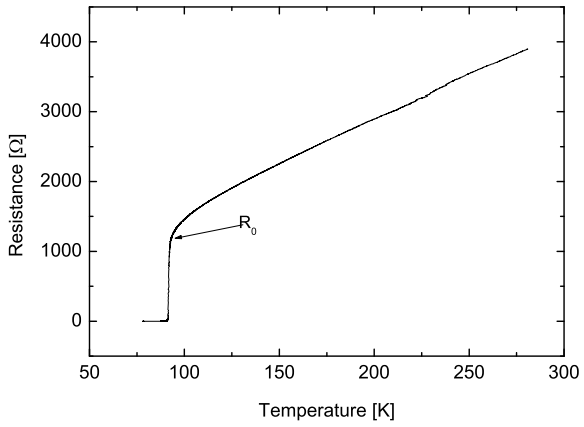

Figure 4.11: Resistance in dependence of temperature. The superconducting transitions takes place at 90.5 K.

The temperature dependence of the resistance R is shown in Figure 4.11. The transition to superconductivity (R=0) occurs at 90.5 K with a transition width estimated as $\Delta T = T(0.9R_0) - T(0.1R_0) \approx 1K$, where R_0 is given in Figure 4.11. This high transition temperature and the narrow transition width indicate the very good superconducting properties of the sample.
The crystallographic quality was examined by means of standard X-ray diffrac-

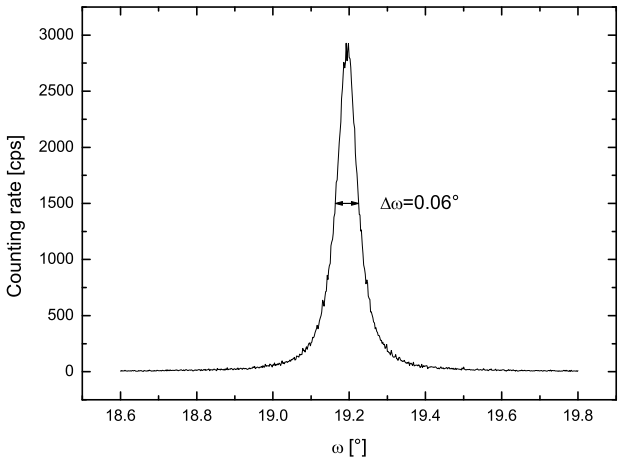

Figure 4.12: Rocking curve of $YBa_2Cu_3O_7$ 005 reflection at room temperature with Cu-Kα radiation. The rocking curve width is about 0.06°.

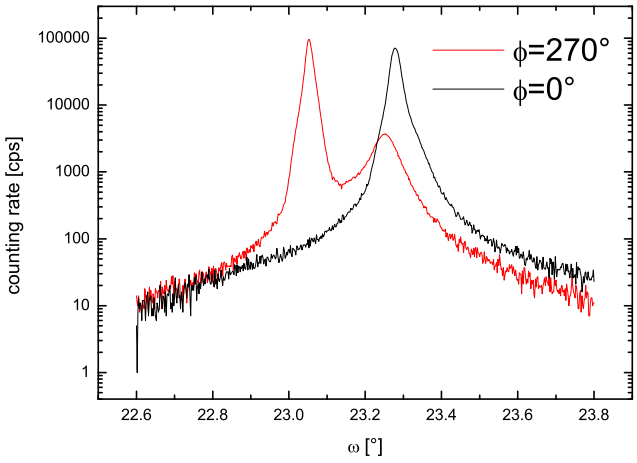

Figure 4.13: Rocking curve of $YBa_2Cu_3O_7$ 006 and $SrTiO_3$ 002 reflection at room temperature with Cu-Kα radiation in logharithmic scale. Both reflections can be separated.

tometry. For these characterization measurements Cu-Kα radiation was used. In Figure 4.12 a rocking curve for the $YBa_2Cu_3O_7$ 005 reflection is shown. The small FWHM of about 0.06° confirms the high quality of the thin film. For the experiment the $YBa_2Cu_3O_7$ 006 reflection is used which is very close to the $SrTiO_3$ 002 reflection. For the success of the experiment it is crucial that both contributions can be separated. In close collaboration with the Low Temperature Physics Group of the Institute of Solid State Physics at the University of Jena the parameters for the thin film growth (including the miscut of the substrate) were carefully adjusted to allow for the separation of the two reflections. Attention had to be paid also to the azimuthal orientation. This can be seen in Figure 4.13, where rocking curves are shown for two different orientations of the sample used for the pump-probe experiment. Only for azimuths $\phi \sim 90°$ and $\phi \sim 270°$ both contributions can be resolved (only the latter example is shown), while a azimuthal rotation by 90° let the two reflections merge.
The reasons for using a thin film sample rather than a single crystal were twofold:

- As already mentioned, for a high sensitivity measurements, the matching of excited and probed volume is crucial. For a thick sample, e. g. a single crystal, the excited and probed volume is given by the appropriate extinction depths, i. e. 70 nm for the pump pulse and about 600 nm for the probe pulse. For the thin film the probed volume is limited by the film thickness.

- Using a thin superconducting film as sample provides the opportunity to have an in-situ control for damages. A small current can be used to measure the resistivity of the excited and probed volume. If the sample were damaged by the pump pulse this could immediately be seen in the resistivity. The path for the current must be defined.

To take advantage of the second point, the sample was structured for the pump and probe experiment, i. e. all $YBa_2Cu_3O_7$, apart from a meander of width 100 μm, was again etched away. The sample design is shown in Figure 4.14. As the

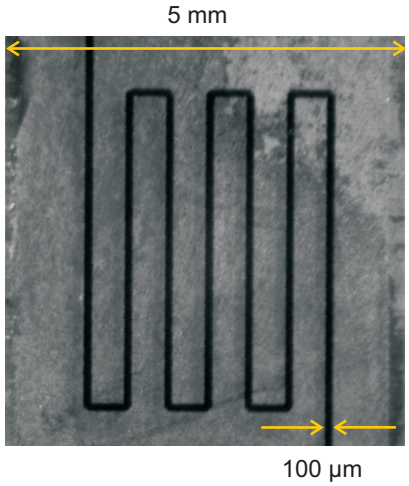

Figure 4.14: Photograph of the sample used in the pump-probe experiment. The dark structure is the $YBa_2Cu_3O_7$ meander. The non-uniform background is due to conductive silver at the back side of the transparent $SrTiO_3$ substrate.

sample could be horizontally translated during the experiment the meander-like structure actually provides seven samples: In case of a damage by the pump pulse the sample could be simply translated to the next bar. It was also possible to redirect the probe current (not shown in Figure 4.14) to further allow for the resistivity measurement.

4.5 The X-ray detector

In a first experimental campaign a front illuminated CCD camera (from ARP) was used to record the diffraction signal. A typical image is shown in Figure 4.15. The diffraction signal forms a section of a Kossel cone (positioned in the center of the image). At the right border of the diffraction signal a tail shows up which originates from defects of the bent crystal. Further features are four camera damages (two at the upper border of the image and two below the Kossel

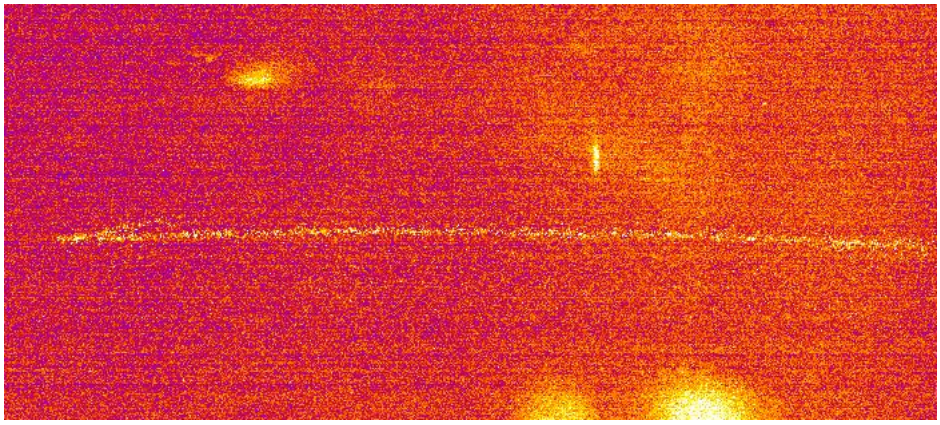

Figure 4.15: X-ray diffraction signal recorded with the ARP front illuminated CCD. $YBa_2Cu_3O_7$ on $SrTiO_3$. To be seen is only the $SrTiO_3$ 002 reflection.

cone). Strikingly, only one diffraction signal is seen (from the $SrTiO_3$ substrate). The signal from the thin film is absent, even though for these exposures an unstructured sample was used. The reason for this will become more clear if we compare this CCD image with one recorded with the deep depletion back illuminated camera from ANDOR [96] used in the later experimental campaigns (see Figure 4.16). Here one clearly sees two diffraction signals - the stronger

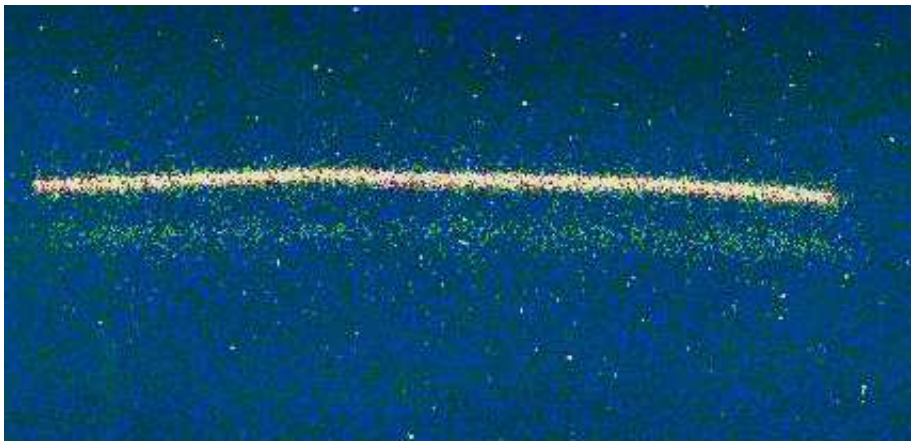

Figure 4.16: X-ray diffraction signal recorded with the ANDOR deep depletion back illuminated CCD. $YBa_2Cu_3O_7$ on $SrTiO_3$. Both reflections, $SrTiO_3$ 002 and $YBa_2Cu_3O_7$ 006, are observed.

one originating from the substrate and a much weaker one from the thin film. The parameters of the two samples used (layer thickness etc.) were comparable in both cases. The signal from the $YBa_2Cu_3O_7$ film is formed by single photon events only, i. e. one pixel is hit only by one photon. And this is the reason

	ARP front illuminated	ANDOR deep depletion back illuminated
Chip size	(2.03×2.03) cm^2	(2.66×0.67) cm^2
Number of pixels	1024×1024	1024×256
Quantum efficiency	$\sim 80\%$ (Ti-Kα)	$\sim 90\%$ (Ti-Kα)
Amplification	1.5 keV / count	23.5 eV / count
Working temperature	$-30°$	$-50°$
Dark current noise	~ 2 counts/pixel/s [114]	~ 2 counts/pixel/s
Readout noise		0.6 counts

Table 4.4: Comparison of the two cameras used in the pump-probe experiment. The noise level given for the ARP camera is due to both, the dark current noise and the readout noise. Given exposure times of several seconds, it is obvious that with the ARP camera a single Ti-Kα photon, which creates three counts per photon can not be distinguished from noise.

why the diffraction signal from the thin film could not be detected by the ARP camera: Because of much lower signal amplification the camera could not be used in the single photon regime, i. e. the signal from the thin film lies under the noise level. For a comparison of both cameras see Table 4.4. Moreover, there are no damages on the ANDOR camera which eventually would limit the effective detector area. Therefore, the use of the ANDOR camera is an important improvement for the experiment.
Further, the ANDOR camera provides a good energy resolution in the single photon regime allowing to decide whether the pixel of interest was hit by a Ti-Kα photon or by a photon of different energy (noise). For the $YBa_2Cu_3O_7$ reflection this is important to gain a sufficient signal to noise ratio.

4.6 The Cryostat

The sample was cooled by a commercial Stirling motor: Helium gas is isothermally compressed and expanded and heat is transferred isochorically in a cycle process. In principle, temperatures can be reached as low as about 35 K, however the absence of radiation shielding (as required by the experimental setup) and the oxidation of the copper surface of the sample holder (transforming the sample holder into a good absorber) led to heat input that limited the achievable temperatures. The minimum temperature attainable was about 70 K. The temperature could be adjusted by a feed-back control system: The cooler is

always working at maximum power. To increase the temperature, there is a heater, i. e. a resistor, positioned on the sample holder. A silicon diode is measuring the temperature. The heating power is automatically adjusted so that the final temperature was stable within 0.2 K. The absolute accuracy of the temperature was about 1 K.
After the acquisition of the time-dependent X-ray diffraction data presented in sections 6.1 and 6.2 the heater failed and so did the temperature adjustment. The working temperature of the cooler was therefore limited to the minimum temperature attainable with the cooler working at maximum power, i. e. about 70 K. The stability of the temperature has declined to about 1 K. Therefore no time-resolved X-ray diffraction data at higher temperatures could be taken.

4.7 Data Analysis

For the data analysis first a background image is substracted from the signal image. Subsequently, a filter is applied to eliminate high energy photon events: If the difference of the contents of two neighbouring pixels is higher than a given threshold, the content of the hard event will be replaced by the average of the three neighbouring pixel one line above that event (see Figure 4.17). Apparently, the threshold must be chosen in such a way as not to cut the real

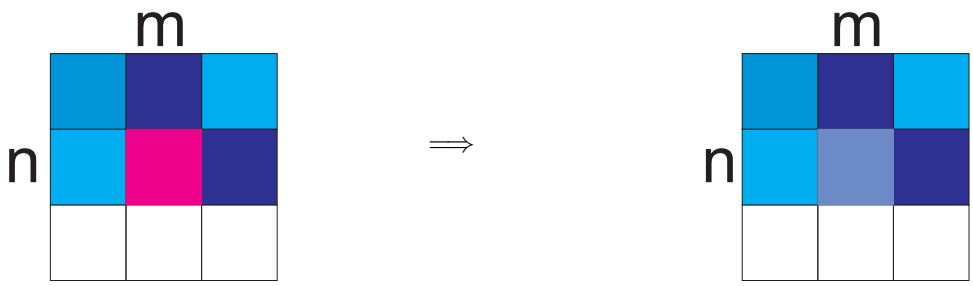

Figure 4.17: Correction of hard events: The hard event at [n][m] is replaced by the average of the content of the three neighbouring events above the hard event.

signal, and at the same time to find the high energy photon events overlaying the diffraction signal. For the experiment it was necessary to accumulate over several thousand (2000-3000) impulses, implying a total exposure time of 200 - 300 seconds, given a repetition rate of 10 Hz. In order to reduce the dark current of the CCD, the exposure times were limited to 20 - 30 seconds. All high energy photon corrected images for a given delay are summed up to form the total image.
As mentioned above, the signal forms a section of a cone on the CCD and must be straightened for further analysis. This is done by fitting the signal with a

parabola and applying the inverse function to the signal. Thereafter the lines are summed up resulting in a rocking curve. A typical image is shown in Figure 4.18. To obtain this rocking curve, 2000 pulses were accumulated. As can be seen a high dynamic range of 10^3 is achieved. The peak of the stronger $SrTiO_3$ 002 reflection is formed by about 200.000 photons and the $YBa_2Cu_3O_7$ peak by about 10.000 photons, thus the number of diffracted photons by the $YBa_2Cu_3O_7$ thin film is about $\frac{1}{20}$ of the number of diffracted photons by the $SrTiO_3$ substrate. The angular separation $\Delta\omega$ of the two peaks is given by the

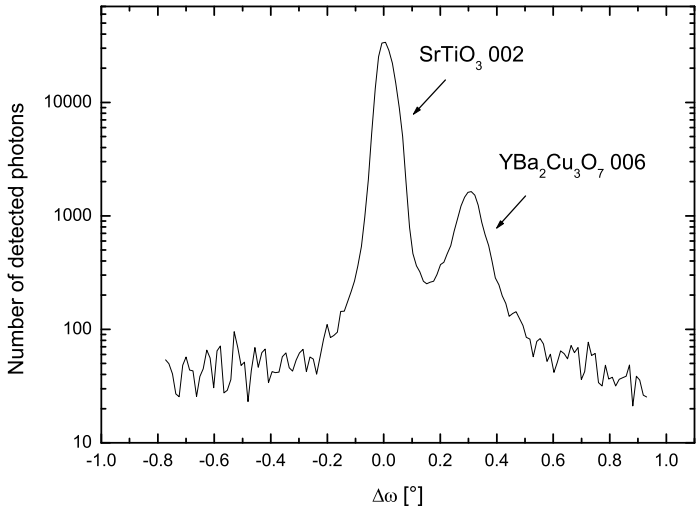

Figure 4.18: Measured rocking curve from the $YBa_2Cu_3O_7$ thin film on the $SrTiO_3$ substrate recorded with Ti-Kα_1 radiation from the laser plasma source. Intensity is plotted in logarithmic scale. 2000 pulses were accumulated.

Bragg angle difference plus the orientation deviation between the substrate and the thin film.

For further analysis, the rocking curve is fitted by an analytical function. Best results are obtained by using a four Gaussian fit as shown in Figure 4.19 for the same data set as in Figure 4.18. The reason for using two Gaussians to fit the $SrTiO_3$ reflection is a small asymmetry which will be discussed in more detail in Section 6.2 and 7.2. Table 4.5 compares the photon numbers collected in the individual contributions to the signal. Due to the large width of the background contribution it collects a rather large number of photons. However, the broadness also leads to large fit errors. Its dependence on the delay does not show any correlation with the data for $SrTiO_3$ or $YBa_2Cu_3O_7$ at all. However, it is noted, that the background signal limits the sensitivity of detecting small

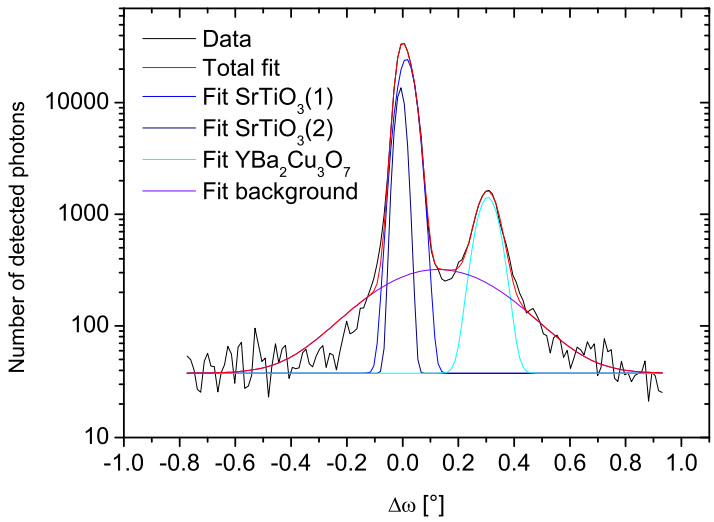

Figure 4.19: The measured rocking curves are best fitted by four Gaussian: two Gaussian for the $SrTiO_3$ 002 reflection, one for the $YBa_2Cu_3O_7$ 006 reflection and one for the background

changes in the pedestals of the $SrTiO_3$ or $YBa_2Cu_3O_7$ signal.
For further analysis the fit parameters of the two $SrTiO_3$ peaks are used to reconstruct the reflection profile and then to numerically extract the peak position, the peak value, FWHM and the integral, which are analyzed in terms of their dependence on the delay between pump and probe pulse. For the $YBa_2Cu_3O_7$ peak, the fitting results are used directly for the analysis of the temporal dependence.

Peak	Number of photons
$SrTiO_3$ 002	191000 ± 4000
$YBa_2Cu_3O_7$ 006	11000 ± 500
Background	12500 ± 1500

Table 4.5: Comparison of number of photons in the individual contributions to the entire signal (Values from fits)

4.8 Signal stability

To gain as much information as possible about the lattice response it is necessary to analyze also the integrated reflectivity. However, as discussed in Section 4.3, the X-ray emission from laser produced plasmas may suffer from temporal instability. This is shown in Figure 4.20, where the number of photons per pulse in the $SrTiO_3$ signal is plotted as a function of measured delay points. The sig-

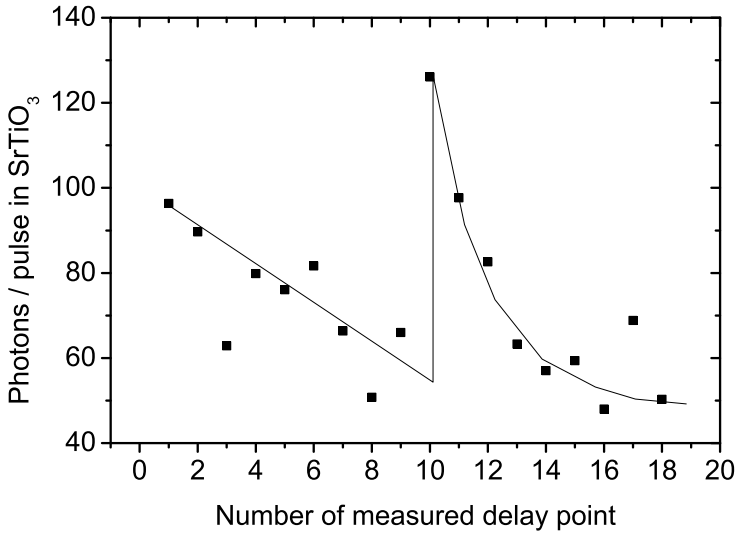

Figure 4.20: Detected Photons per pulse diffracted from the $SrTiO_3$. The decrease is due to lower laser intensities due to debris. The strong increase at delay point 10 is due to an exchange of debris protection.

nal has decreased to 50% already after 9 time points (21000 pulses in total). After the exchange of debris-protection the initial photon number is reestablished and even exceeded - followed again by a rapid decrease. Both, the higher photon number after the debris protection exchange (compared to the initial value) and the much faster, exponential-like decrease afterwards (compared to the approximately linear decrease before the exchange) can be explained by slightly different focusing conditions due to a slight rotational misalignment of the debris protection. The debris protection is a thin quartz plate in front of the parabola. During the exchange the angle of that plate is not controlled. Also, the focus is not realigned or controlled. Slightly different focusing conditions may influence the experiment in different ways:

- The X-ray source size can be modified. Reich et al. have shown that for

higher laser intensities a substantial part of X-ray emission originates from a halo around the central emission and cannot be explained by scattering of electrons inside the solid target as in case of lower intensities [110]. Thus, slightly better focusing conditions can lead to significantly larger X-ray source sizes.

- The reflected intensity from the bent crystal may change. If initially the alignment of the bent crystal is not at the maximum of the rocking curve but at a edge, a slight shift of the X-ray source may significantly alter the reflectivity.

Due to the narrow GaAs rocking curve width a shift of the X-ray source will not necessarily also cause a shift of the X-ray focus.
The temporal decrease and instability of photon numbers show the requirement for a normalization. The initial idea was to use the substrate $SrTiO_3$ 002 reflection for normalization. However, as was already mentioned in the introduction and will be discussed in more detail in the following chapters, the $SrTiO_3$ reflection has changed. Therefore, the substrate reflection cannot be used for normalization. Thus, for integrated reflectivities only relative changes between $YBa_2Cu_3O_7$ and $SrTiO_3$ can be discussed. Four diffraction signals were also acquired with the pump pulse being blocked - giving another possibility for normalization. They may assist in the discussion and interpretation of the results. However, they cannot be used to interpolate the undisturbed signal for a given exposure. For the analysis, the $SrTiO_3$ peak value of every exposure (as given by the fitting procedure) is arbitrarily set to 1. Thus, the remaining parameters (besides the peak positions and FWHM) are discussed only relative to the $SrTiO_3$ peak value.

4.9 Pump and Probe conditions

The photon energy of the pump pulse is 1.55 eV. At this photon energy the attenuation length in $YBa_2Cu_3O_7$ is about 100 nm. For $SrTiO_3$ Cardona et al. have measured the optical absorption. At 1.55 eV the absorption length is much larger than 1 m [115]. Since the pump flux with 80 $\mu J/cm^2$ was very low, this means that the pump pulse exclusively excites the thin $YBa_2Cu_3O_7$ film. No excitation by single photon absorption in $SrTiO_3$ takes place. A pump flux of 80 $\mu J/cm^2$ corresponds to a photon flux of about 10^{14} Photons/cm^2, thus this is also the maximum number of electronic excitations in $YBa_2Cu_3O_7$. A carrier density of $\sim 10^{19}$ cm^{-3} at maximum could thus be excited. This must be set in relation to the unit cell density which is $\sim 6 \cdot 10^{21}$ cm^{-3}. Thus, the

photoinduced carriers can affect only 0.2% of the probed volume. This is also the upper limit for a change of integrated reflectivity induced by these carriers. Nevertheless, the result of the optical excitation is a massive breaking of Cooper pairs. The initial Cooper pair density is about $7 \cdot 10^{21}$ cm^{-3} [116], and thus comparable with the unit cell density. As the pump fluence is chosen high enough to break all Cooper pairs, this means that modifications induced by breaking of the Cooper pairs may be substantial, given large enough changes in an individual unit cell.

The pump fluence leads to a temperature rise which was estimated to be $\Delta T \approx 7$ K. This is not enough to drive the superconductor into normal conducting state. Furthermore, the time needed for an increase of lattice temperature is large compared to the delays at which the sample is probed. Thus, lattice heating effects may be neglected in the discussion of the temporal lattice response.

The extinction depth for the X-ray probe beam for thick $YBa_2Cu_3O_7$ and $SrTiO_3$ samples are approximately the same (500 nm). As $YBa_2Cu_3O_7$ is on hand as a thin film, the interaction volume is limited by its thickness of 250 nm. The single parameters for the pump and the probe pulse are summarized in Table 4.6.

	Pump pulse	Probe pulse
Photon energy	1.55 eV	4.5 keV
Pulse duration	100 fs	$\sim 200 \ldots 300$ fs
Attenuation length		
in $YBa_2Cu_3O_7$	100 nm	500 nm
in $SrTiO_3$	$\gg 1$ m	500 nm

Table 4.6: Pump and Probe conditions for the time-resolved X-ray diffraction experiment.

5 Preparatory static measurements

Temperature dependent static rocking curves were recorded in order to estimate necessary exposure times for the measurements at the laser plasma source and in order to inspect the operability of the cooler and other required devices. The sample used for the static measurements was comparable with the one later used for the time resolved X-ray diffraction study (see Section 4.4). As the X-ray beam does not damage the thin film an unstructured sample was used. These static measurements were performed at an X-ray tube with titanium anode. The schematic setup was chosen as for the pump-probe experiment and will not be discussed separately. However, there were three important differences between both experimental conditions:

1. The X-ray source size at the laser generated plasma was of the order of 100 μm [110], at the X-ray tube 400 μm.

2. The toroidally bent crystal used for the pump-probe experiment was a GaAs(100) crystal. For the static measurement a Si(311) crystal was used. Both were compared in Table 4.2.

3. While for the pump-probe experiment an X-ray CCD camera as detector was used, for the static measurement Agfa Strukturix X-ray film was employed.

As a consequence of the first two differences the K_α doublet could not be separated in the static measurements at the X-ray tube . Both K_{α_1} and K_{α_2} were reflected off the bent crystal. The diffraction signal was digitized by means of densitometry. The experimental setup does not allow for determination of lattice constants. Also changes in the lattice constants are not readily detectable. The temperature was varied between 300 K and 80 K.
Some of the recorded rocking curves are shown in Figure 5.1. The two peaks at 300 K are the K_{α_1} and K_{α_2} $SrTiO_3$ 002 reflections. The position of the K_{α_1} peak was set to $\Delta\omega = 0$. For that sample the $YBa_2Cu_3O_7$ contribution cannot be resolved. This is firstly due to the intensity ratio between substrate and film diffraction intensity (see Figure 4.18) and, secondly, to a miscut of the sample that brings the contributions of the film and the substrate too close to each

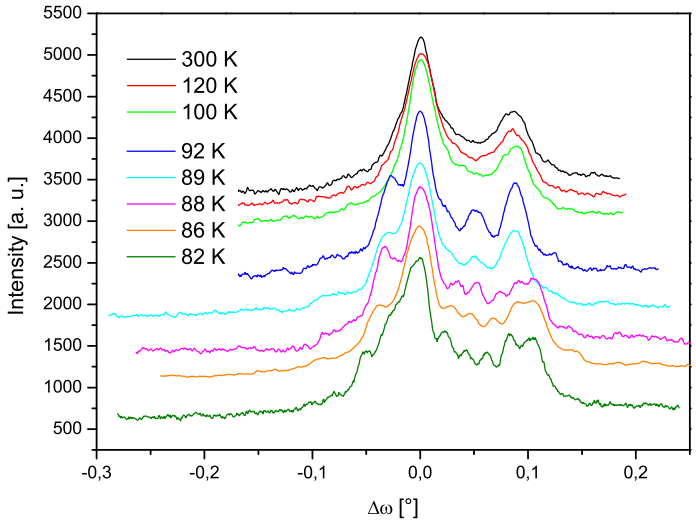

Figure 5.1: Rocking curves of a $SrTiO_3$ single crystal covered with a thin $YBa_2Cu_3O_7$ film at different temperatures.

other.

At 92 K the two peaks have split into four peaks, reflecting the cubic to tetragonal phase transition of the $SrTiO_3$ substrate. The observation that at 100 K the tetragonal splitting has not yet occured is in line with Lötzsch [79], who investigated the structural phase transition of $SrTiO_3$ in more detail. He found that even though the rotation of the oxygen octahedra starts at 105 K, formation of twin domains starts only at lower temperatures, which also depends on external parameters as the epitaxial strain. After passing the superconducting transition temperature (T_c=89 K) a number of further peaks show up in Figure 5.1 becoming even clearer at lower temperatures. This finding might be interpreted as hint for strain induced in the substrate at the superconducting transition temperature.

The larger linewidth of the upper three curves in Figure 5.1 is due to a lower angular resolution of those scans.

To possibly further elucidate the origin of the strain, the temperature-dependent measurements were repeated with the same sample. Between the individual measurements the temperature was raised to room temperature. The rocking curves at 85 K (86 K for the first scan) obtained from three consecutive scans are shown in Figure 5.2. The three rocking curves were obtained under the same conditions. No parameters were varied yet. However, the rocking curves

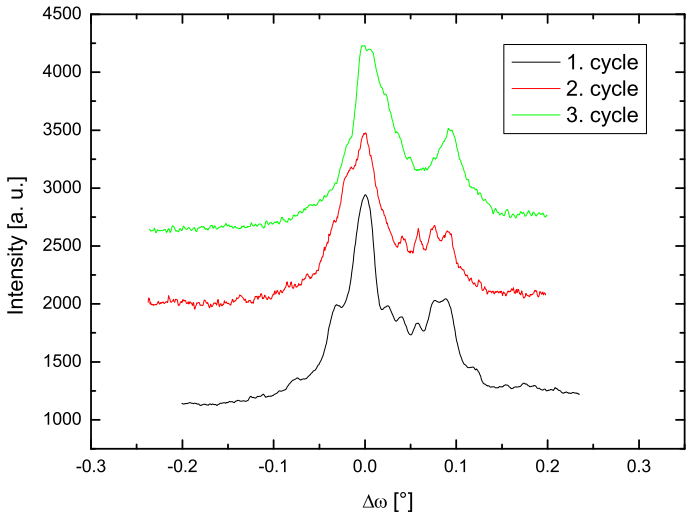

Figure 5.2: Rocking curves of a $SrTiO_3$ single crystal covererd with a thin $YBa_2Cu_3O_7$ film at 85 K taken from three individual temperature scans.

are very different. The rocking curves of the first two cycles differ only in the exact positions and intensity ratios of the individual maxima. For the third scan, however, the secondary maxima have disappeared and the main maxima are strongly broadened. During all these measurements the $YBa_2Cu_3O_7$ thin film was superconducting. Thus, after repeated cooling the sample has changed, as was also observed by Lötzsch [79] (see also Section 2.2.3). It is clear, that the mechanism leading to the disappearence of the additional peaks is closely connected to the reduction of the clamping effect. This, in turn, indicates, that the additional peaks are closely related to the thin film behaviour of the substrate induced by the epitaxial thin film.

The appearence of the additional peaks can be explained if one domain experiences a linear strain as shown in the inset of Figure 5.3, while the other one remains unstrained. Especially the latter is an idealization not being realistic, which can also be seen in Figure 5.1. Already for $T = 92$ K, thus well before the appearence of the additional peaks there is a signature of strain being present: There is a shoulder at the large angle side of the largest peak, that cannot be attributed to any single-crystal reflection. This is not surprising, as in the present of different domains in the low-T phase strain is unavoidable. Also epitaxial strain may lead to the appearance of additional peaks. A modeled reflection curve is examplarily shown in Figure 5.3. The main features (number of peaks, position, intensity ratios) of the measured diffraction signal is reproduced by

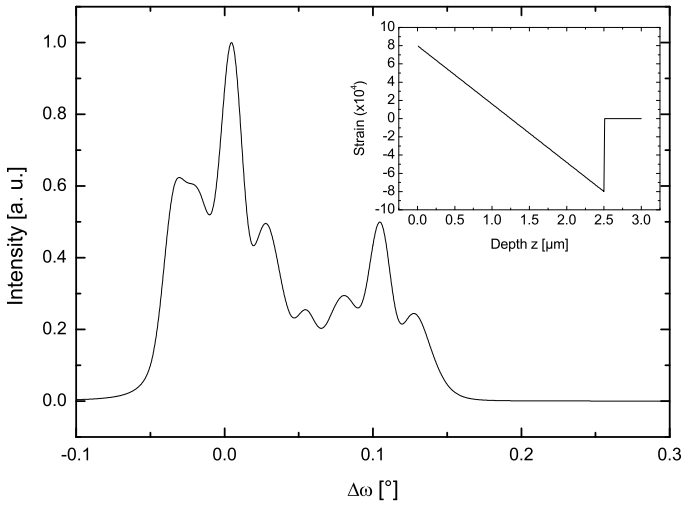

Figure 5.3: Modeled $SrTiO_3$ 200 and 002 rocking curve for Ti-Kα_1 and Ti-Kα_2 for the strain profile shown in the inset.

such a strain profile. As the exact parameters differ strongly between individual experimental data sets, the modelled diffraction curve should only qualitatively compared with the measured data.

6 Time-dependent diffraction data

As was already mentioned in Section 4.8 it is necessary to normalize the data due to instable X-ray emission. In this work the rocking curves are scaled such that the maximum value of the $SrTiO_3$ reflection is set to unity. Data points shown in this chapter were all taken in one day. The sequence at which the delay points were measured is shown in Table 6.1. The lack of data points between

No of Delay point	1	2	3	4	5	6	7	8	9
Delay [fs]	$-\infty$	1400	1300	1200	1100	1000	950	900	$-\infty$
No of Delay point	10	11	12	13	14	15	16	17	18
Delay [fs]	$-\infty$	850	800	750	700	650	600	$-\infty$	-500

Table 6.1: Sequence of measured Delay points. Delays denoted with $-\infty$ are associated with unpumped exposures.

-500 fs and +600 fs is due to experimental constraints that required stopping the data acquisition after Delay point 18. The complexity of the data analysis prevented an online analysis and thus a more appropriate choice of Delay points. After finishing the data acquisition after Delay point 18 the sample was heated up to room temperature. The following days, no transient signals were observed anymore. As shown in Chapter 5 the sample properties may have changed upon repeated cooling and heating. It will be argued in Section 7.2 that these changes will necessarily result in the absence of a transient signal.
In between delay point no. 9 and 10 the debris protection was exchanged. It was discussed in Section 4.8 that this can lead to a modified X-ray source size and different X-ray photon numbers in the X-ray focus. Due to normalization the latter does not affect the analysis of the data. A shift of X-ray source is not necessarily expected. The modified X-ray source size may be reflected in the measured rocking curve width and in the film to substrate reflection intensity ratio (if the X-ray focus is broader than the meander structure). Indeed both effects were observed and the data had to be corrected for. The way this is done is examplarily shown for the rocking curve width of the $SrTiO_3$ 002 reflection. Raw data are shown in Figure 6.1 (a). Data points at $-\infty$ refer to the unpumped exposures. Black (red) data points are those acquired before

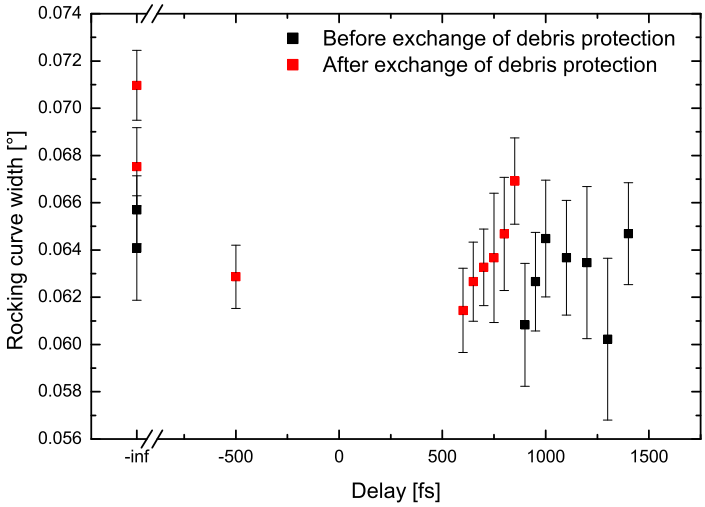

(a) Raw data

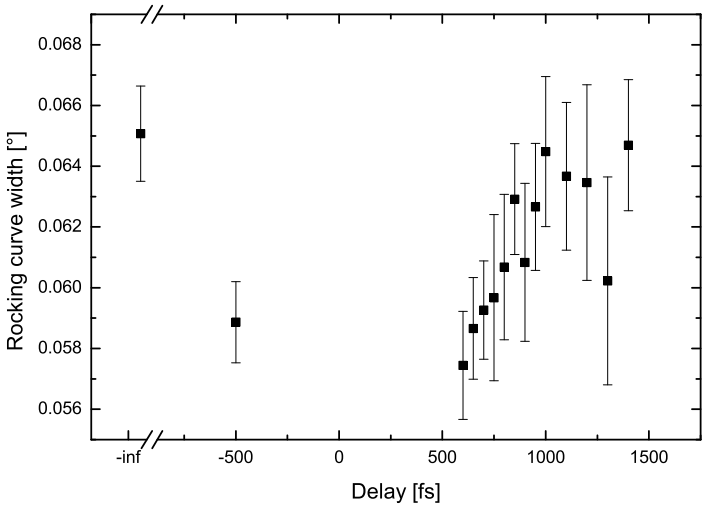

(b) Shifted data

Figure 6.1: Rocking curves acquired after the debris protection exchange are systematically broadened due to a larger source size. The data are corrected for by shifting the data points acquired after the exchange of debris protection with respect to those acquired before. The new unpumped value ($\Delta\tau = -\infty$) is the mean value of the four (shifted) individual unpumped data points.

(after) the exchange of the debris protection. Remarkably, the unpumped data points acquired after the debris protection exchange differ significantly from

those before the exchange: The measured linewidth has increased after the exchange. Also, there is a jump in the temporal trend of the pumped data points. This effect is corrected for in the following way:

1. The mean values of the unpumped data before and after the debris protection exchange are calculated.

2. The data points acquired after the debris protection exchange are shifted with respect to those acquired before in order to achieve overlap of the two unpumped values.

The result is shown in Figure 6.1 (b). The error of the unpumped value is now the standard deviation of the four (shifted) unpumped points. In the same way the data sets for the $YBa_2Cu_3O_7$ integrated reflectivity and linewidth as well as the $SrTiO_3$ integrated reflectivity and the ratio between both reflections is corrected.

6.1 Temporal response of $YBa_2Cu_3O_7$

Integrated reflectivity

In Figure 6.2 the integrated reflectivities for the $YBa_2Cu_3O_7$ 006 reflection in dependence on the delay between pump and probe pulse are shown. The corrected data are shown in Figure 6.2(b). Data are plotted as relative changes with respect to the mean unpumped value. In the frame of experimental uncertainties no definite conclusions can be drawn. However it seems that upon excitation the integrated reflectivity of the $YBa_2Cu_3O_7$ 006 reflection drops. Again, this statement is made with the constraint that the $SrTiO_3$ peak value is set to 1. The fact, that at $\Delta\tau = -500$ fs the signal is already reduced can be explained by the error of the determination of temporal overlap ($\sim$ 700 fs, see Section 4.1). The temporal resolution is nevertheless only limited by the duration of the pump and probe pulses, and is thus of the order of $100 \ldots 200$ fs. At $\Delta\tau \sim 1$ ps, the integrated reflectivity has recovered to its undisturbed value.

The peak value of the $YBa_2Cu_3O_7$ 006 reflection was evaluated in the same way as the integrated reflectivity. The results are shown together with the relative changes of the integrated reflectivity in Figure 6.3. For the sake of clarity error bars are not shown besides the ones for the unpumped exposures. It can be seen that the integrated reflectivity as well as the peak value follow the same time dependence. This shows that the rocking curve shape is essentially conserved and it indicates a reduction of structure factor (if the effect is not exclusively to be explained by the normalization to the $SrTiO_3$ 002 peak value).

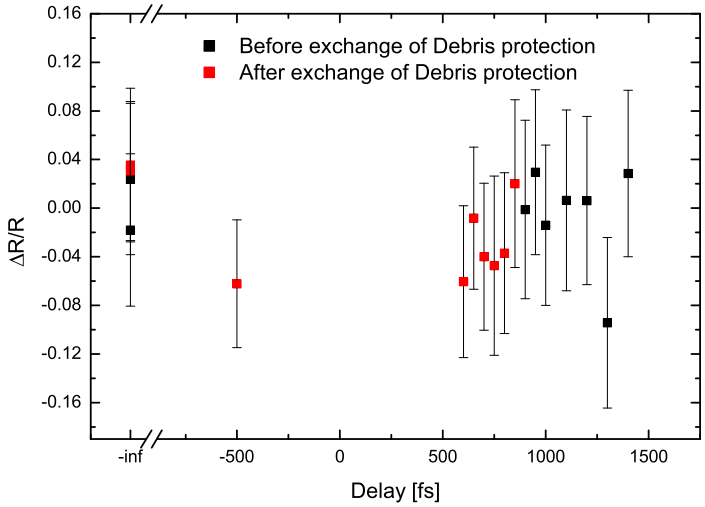

(a) Raw data

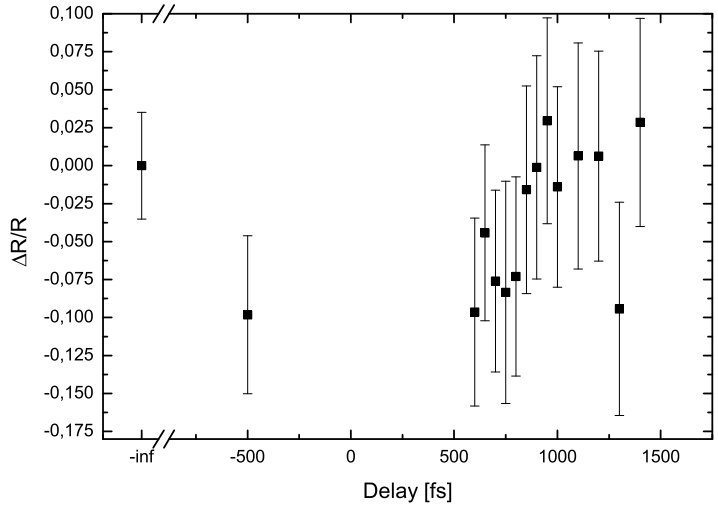

(b) Shifted data

Figure 6.2: Integrated reflectivity changes of the $YBa_2Cu_3O_7$ 006 reflection in dependence on delay between pump and probe pulse. The peak value of the substrate $SrTiO_3$ 002 reflection is set to 1.

Peak position

The peak position in dependence on the delay between pump and probe pulse is plotted in Figure 6.4. It is given relative to the first unpumped value of

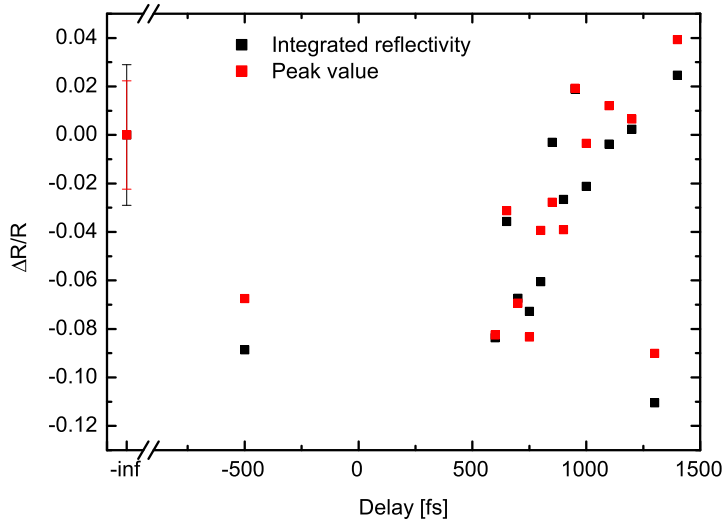

Figure 6.3: Comparison between the relative changes of integrated reflectivity and the peak value of the $YBa_2Cu_3O_7$ 006 reflection. The peak value of the substrate $SrTiO_3$ 002 reflection is set to 1.

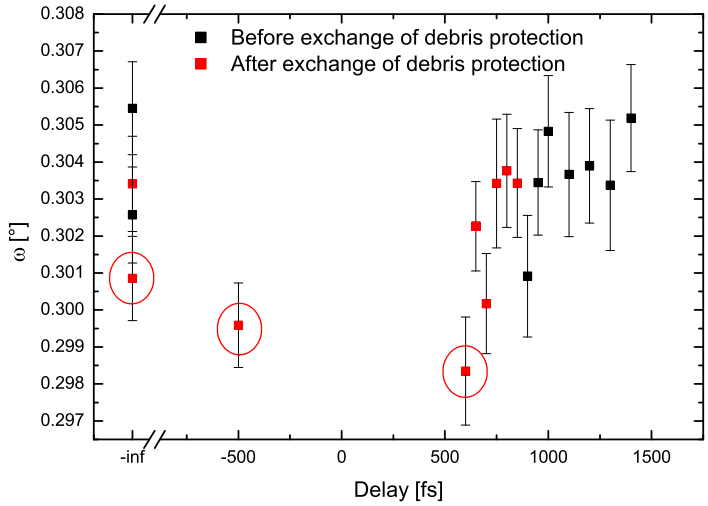

Figure 6.4: The position of the $YBa_2Cu_3O_7$ 006 reflection in dependence on the delay between pump and probe pulse. The peak position is given relative to the initial position of the $SrTiO_3$ 002 reflection. The three marked data points are the last three that were taken.

the $SrTiO_3$ peak position. A dependence of the peak position on the delay is measured. However the changes tend towards the initial values very fastly: Already for $\Delta\tau \leq 750$ fs the peak position remains constant. For the data evaluation it is useful to compare the unpumped values with the pumped data which were taken in temporal proximity. Special attention should be paid to the data points at delays $\Delta\tau = -500$ fs and $\Delta\tau = 600$ fs, as they exhibit the largest changes and, moreover, an unpumped point was acquired between these data points. In Figure 6.2 it can be seen that the unpumped value for

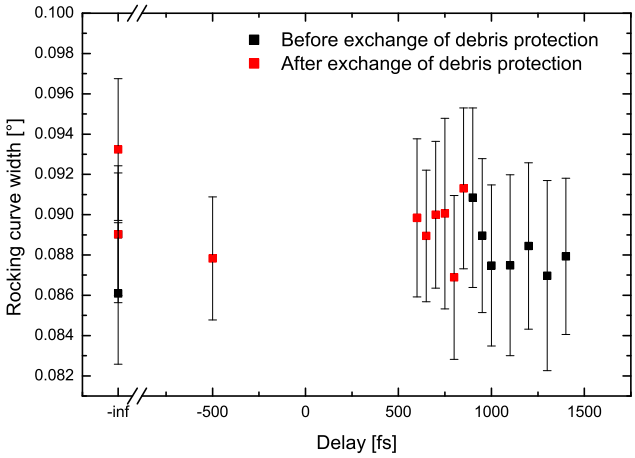

(a) Raw data

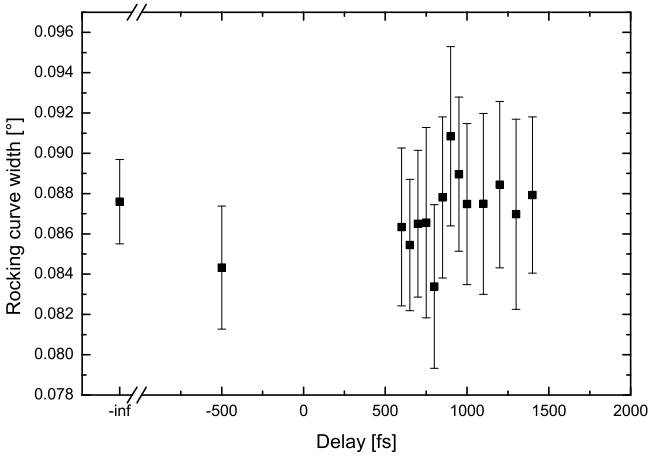

(b) Shifted data

Figure 6.5: The linewidth of the $YBa_2Cu_3O_7$ 006 reflection in dependence on the delay between pump and probe pulse.

the integrated reflectivity is distinctly larger than the values at $\Delta t = -500$ fs and $\Delta t = 600$ fs. The same holds for the peak value. For the peak position, however, the unpumped value taken in between the data at $\Delta t = -500$ fs and $\Delta t = 600$ fs (all three are marked in Figure 6.4) is the lowest unpumped value shown and (considering the error bars) coincides with the two pumped values. This might be an indication that the shift of the $YBa_2Cu_3O_7$ peak is not a real effect.

Peak width

The width of the $YBa_2Cu_3O_7$ rocking curves does not show any modification upon excitation within experimental uncertainty. Results are shown in Figure 6.5. Error bars are of the order of 4% of the linewidth.

6.2 Temporal response of $SrTiO_3$

Rocking curve shape

In Figure 6.6 (a) the results of the fitting procedure (sum of two Gaussians) for the measured rocking curves of the $SrTiO_3$ 002 reflection are shown. Fits instead of raw data are compared as they provide a clearer view; the measured rocking curves together with the fits are shown in Figure 6.6 (b). Fits and data are matching very well. Errors of the data points resulting from photon statistics are smaller than the symbols. The rocking curves are slightly asymmetric having a larger weight at the large angle side. All curves acquired after the exchange of debris protection are shown. The rocking curves before the debris protection exchange are omitted for clarity, because this has also slight impact on the rocking curves (as already seen in case of the $YBa_2Cu_3O_7$ 006 reflection). For all cases the peak value of the rocking curve is scaled to 1. The bold black and red lines show the rocking curve in the unpumped case. The black curve is the first measurement after the exchange of debris protection, the red curve the one before last. They differ slightly on the large angle side. Apparently there is a small drift during the measurement. However, the differences between pumped and unpumped exposures are larger. Most astonishingly, the rocking curve becomes narrower upon excitation. There is also a small shift towards smaller angles. The main changes of the rocking curve shape occur at the large angle side. The maximum shift of the rocking curve is about $\Delta\omega = -0.008^\circ = -0.48'$ and the maximal narrowing is by about 0.01°.
The time dependence of the single parameters are now discussed in more detail.

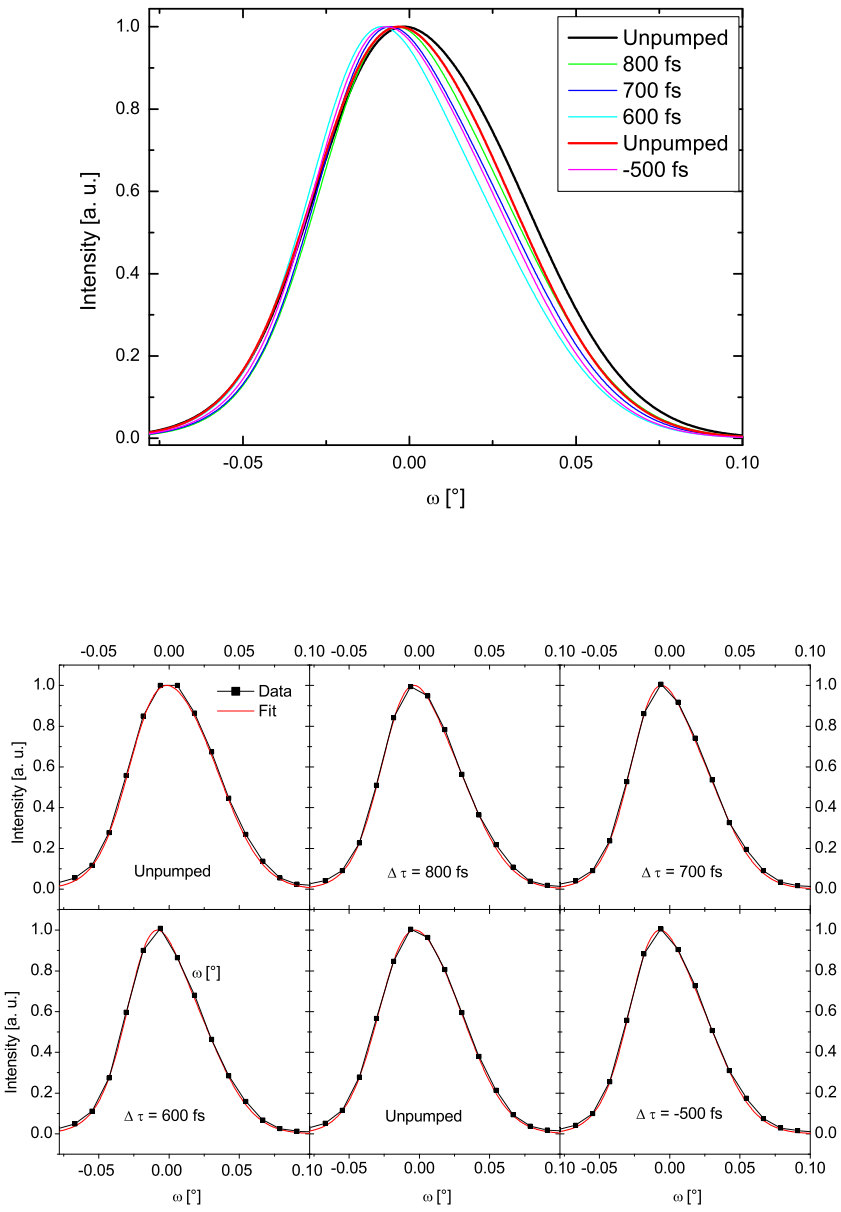

Figure 6.6: Comparison of the $SrTiO_3$ 002 rocking curves for different delays between pump and probe pulse. For clarity only fits are compared. Upon excitation the rocking curve is asymmetrically narrowed and shifted towards smaller angles. In the lower panel, a comparison of the fits from the upper part with the data is shown.

Integrated reflectivity

As the peak of the $SrTiO_3$ reflection is normalized to 1, an analysis of the integrated reflectivity can only yield statements on the rocking curve shape.

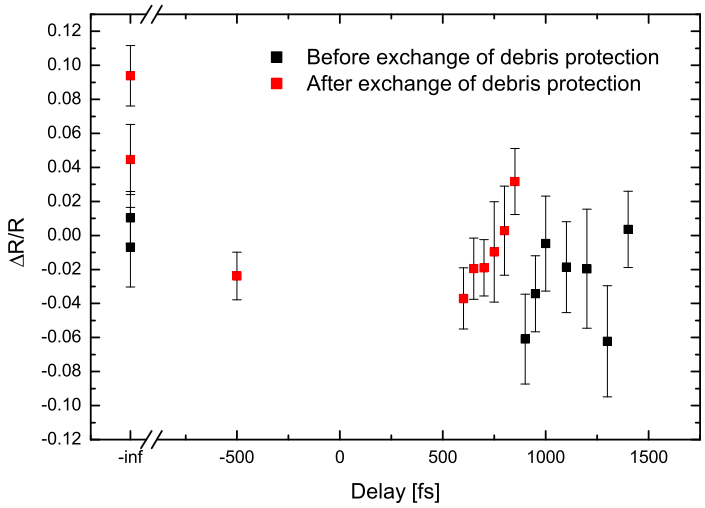

(a) Raw data

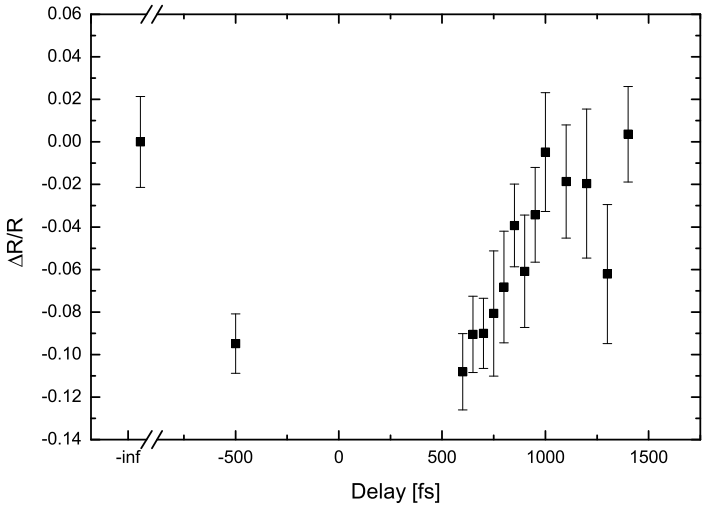

(b) Shifted data

Figure 6.7: Integrated reflectivity changes of the $SrTiO_3$ 002 reflection in dependence on the delay between pump and probe pulse. The peak value of the $SrTiO_3$ 002 reflection is set to 1.

The integrated reflectivity of the normalized $SrTiO_3$ peak in dependence on the temporal delay is shown in Figure 6.7. Data points at $-\infty$ refer to the unpumped exposures. Black (red) data points are those acquired before (after) the exchange of the debris protection. Error bars result from errors of the

fit values and are calculated as described in Appendix B. From the previous discussion of the rocking curve shape it is not surprising that the integrated reflectivity is reduced upon pumping. It reflects the narrowing of the rocking curve. At $\Delta\tau = -500$ fs the ratio of integrated reflectivity to peak value is already reduced by 10% At $\Delta\tau = +600$ fs the integrated reflectivity is even more reduced. However at this delay the relaxation process has already started. The initial value of the integral is reestablished at $\Delta\tau \sim 1000$ fs. From there on, the integral remains constant within experimental uncertainty.

Peak position

In Figure 6.8 the temporal dependence of the peak position, i. e. the shift of Bragg angle is shown. It was determined numerically from the sum of the two Gaussians. The temporal dependence is very similar to the one of the peak

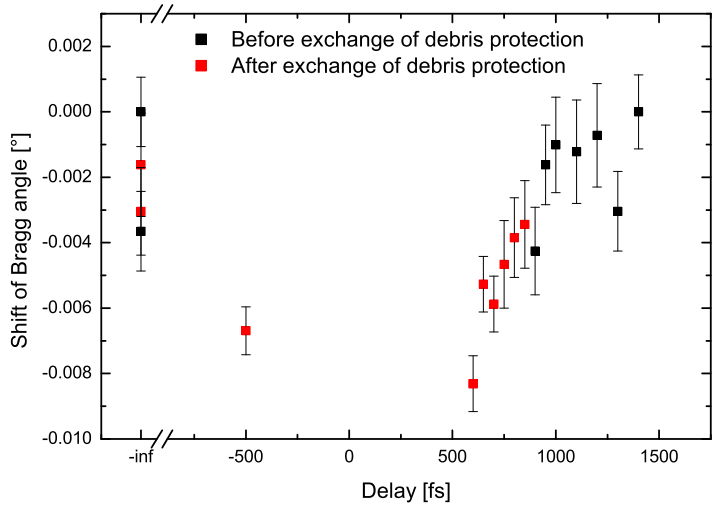

Figure 6.8: The position of the $SrTiO_3$ 002 reflection in dependence on the delay between pump and probe pulse. Values are all relative to the first unpumped exposure.

integral: Already at $\Delta\tau = -500$ fs the Bragg angle is reduced, at $\Delta\tau = +600$ fs, the relaxation process has already started, reestablishing the initial value at about $\Delta\tau \sim 1000$ fs. The maximum shift of the Bragg angle was measured at $\Delta\tau = +600$ fs, corresponding to a relative change of lattice constant of $\frac{\Delta d}{d} = 1.4 \cdot 10^{-4}$.

Peak width

In Figure 6.9 the FWHM for the $SrTiO_3$ peak is shown in dependence on the delay between pump and probe pulse. As was already seen in Figures 6.6 and 6.7, the linewidth is reduced upon excitation. The time dependence is similar

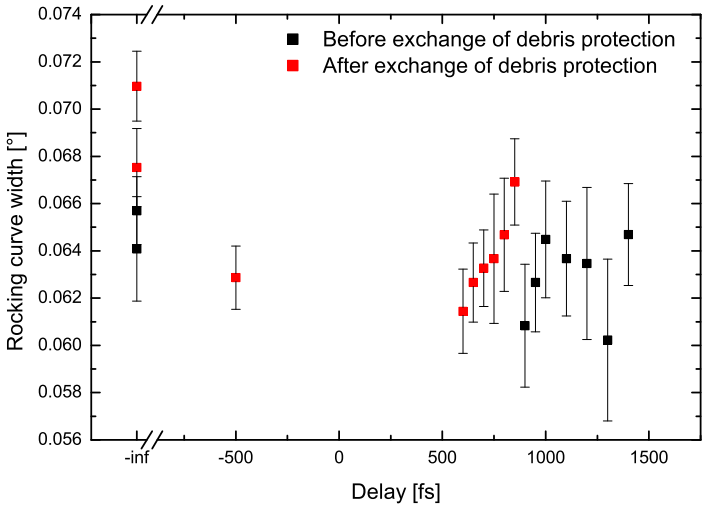

(a) Raw data

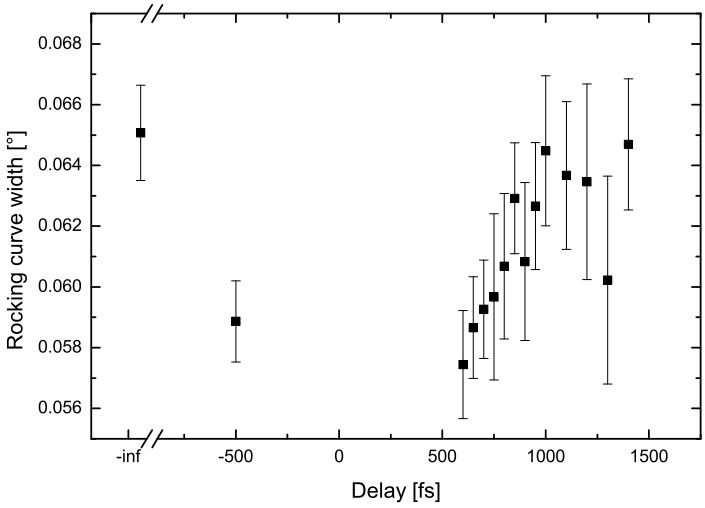

(b) Shifted data

Figure 6.9: The rocking curve width of the $SrTiO_3$ 002 reflection in dependence on the delay between pump and probe pulse.

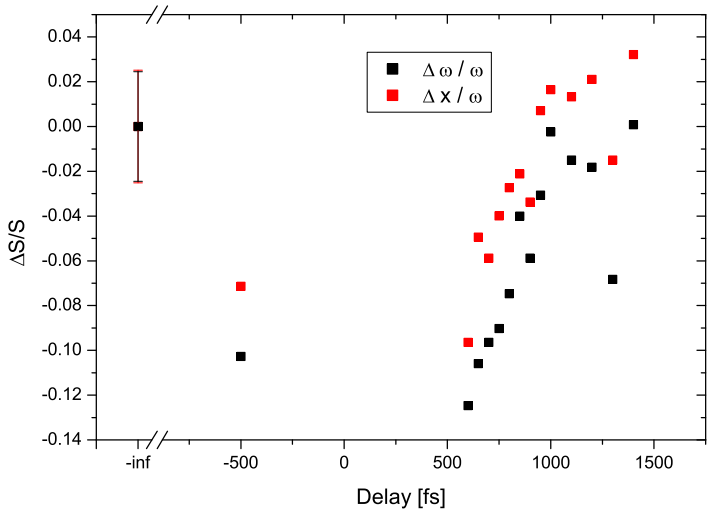

Figure 6.10: Comparison between the temporal dependence of the rocking curve width and the peak position.

to the one for the peak integral and the peak position. The minimum linewidth is measured for $\Delta\tau = 600$ fs, where it is reduced by about 10% compared to the undisturbed value. In Figure 6.10 the shift of the Bragg angle (red data points) is shown together with the change of the linewidth (black data points) of the $SrTiO_3$ 002 reflection. For comparison, both data sets are normalized to the unpumped value of the rocking curve width. Error bars are omitted as to provide a clearer view on the data. The temporal dependence of both parameters is approximately the same. One can see that the peak shifts almost by the same amount as the FWHM is decreased.

Ratio of Peak values

Finally, the ratio of the integrated reflectivities of the two reflections is shown in Figure 6.11. The error bars of individual data points are smaller than 10% of the value itself. In the frame of this experimental accuracy no temporal variation of the ratio of integrated reflectivities can be detected.

6.3 Summary of the Results and Conclusions

To summarize, the following (unexpected) results were obtained:

- The $SrTiO_3$ 002 reflection is affected by the excitation of the $YBa_2Cu_3O_7$

thin film.

- The width and the peak position of the $SrTiO_3$ peak has changed upon excitation. The rocking curve is asymmetrically narrowed.
- The shift of the $SrTiO_3$ peak would correspond to a lattice constant in-

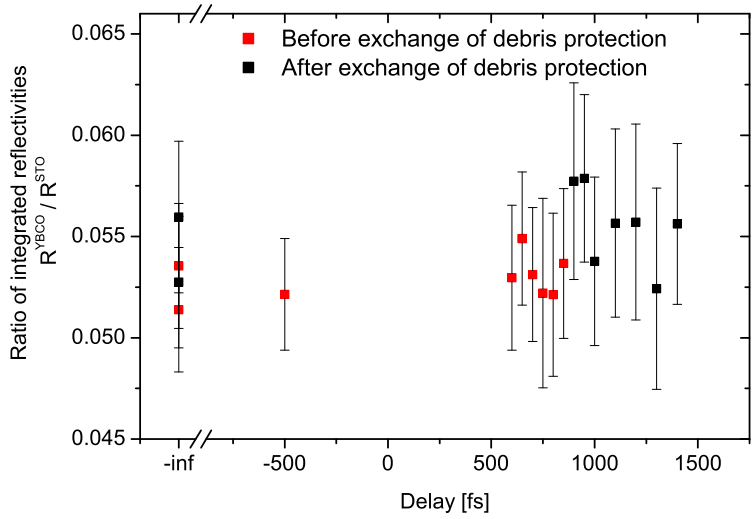

(a) Raw data

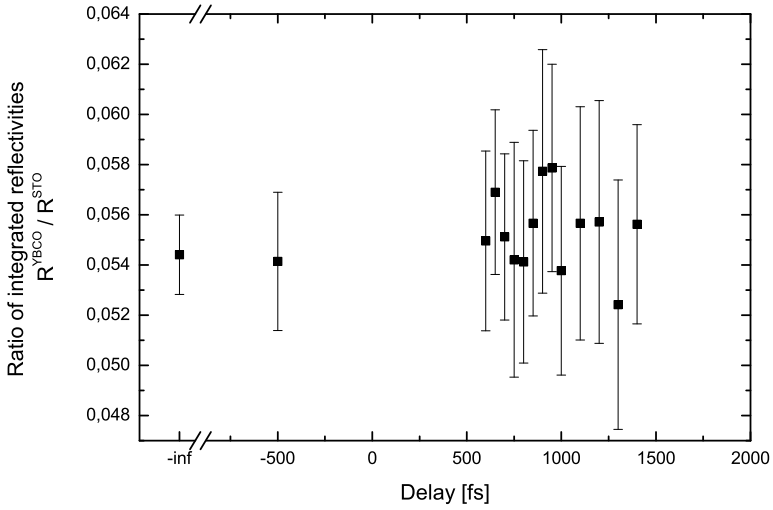

(b) Shifted data

Figure 6.11: Ratio of integrated Reflectivities of the YBa_2CuO_7 006 and $SrTiO_3$ 002 reflection

crease of $\frac{\Delta c}{c} \sim 1.4 \cdot 10^{-4} c$

- The ratio of the peak values between $YBa_2Cu_3O_7$ and $SrTiO_3$ has decreased upon excitation.
- The ratio of the $YBa_2Cu_3O_7$ integral to $SrTiO_3$ peak value has decreased upon excitation. The temporal dependence follows the one of the ratio of peak values.
- The ratio of the integrated reflectivities is not affected by the excitation.
- In the frame of experimental uncertainties a shift of the $YBa_2Cu_3O_7$ peak position could not be uniquely detected.
- The width of the $YBa_2Cu_3O_7$ peak is not altered within experimental precision.
- All changes that are observed have the same temporal dependence. They take place on sub-ps to few ps time scales.

At this point it should be remembered, that there is essentially no optical excitation of the $SrTiO_3$ substrate (see Section 4.9). Therefore all observed crystallographic changes in the substrate must have been induced by the excitation of the $YBa_2Cu_3O_7$ film and must originate at the interface between substrate and film.
It is instructive to estimate the velocity of a surface excitation required to excite the probed thickness of the substrate t on the observed time scales: $v = \frac{t}{\Delta\tau} \sim \frac{500\,\mathrm{nm}}{1\,\mathrm{ps}} = 5 \cdot 10^5$ m/s. This is much larger than the sound velocity in $SrTiO_3$ at 70 K (7000 m/s [117]). Therefore, the timescales can only be explained, if one assumes that a major part of the probed volume is excited coherently, e. g. due to an electric field.

7 Physical interpretation

The most astonishing result of the time-resolved X-ray diffraction experiment performed in this thesis is the fact that the $SrTiO_3$ reflection is affected. Due to the strong absorption of the thin film, the negligible absorption in the substrate and the very low pump fluence, a significant optical excitation of the $SrTiO_3$ can be excluded. Therefore, all crystallographic changes in $SrTiO_3$ must result from changes (electronic and/or crystallographic) in $YBa_2Cu_3O_7$. As crystallographic changes in the $YBa_2Cu_3O_7$ thin film would couple to the $SrTiO_3$ via strain waves, this can be excluded by the time scales at which the changes in $SrTiO_3$ take place. The fact that the time dependence of the changes is similar to that of the optically measured Cooper pair density (see Section 2.1.4) suggests that the crystallographic changes in $SrTiO_3$ are directly caused by the electronic changes in $YBa_2Cu_3O_7$.
In the following, possible effects influencing the lattice response of both the thin superconducting film and the $SrTiO_3$ substrate will be discussed.

7.1 $YBa_2Cu_3O_7$

7.1.1 Number of broken Cooper pairs

As suggested by Mazin et al. [60], Cooper pairs are optically broken by phonons which are released as highly excited electrons relax (see Section 2.1.4). Assuming that the entire pump laser energy is used for breaking Cooper pairs, the total number of broken pairs results to

$$n_b = \frac{(1-R)\cdot F}{t\cdot 2\Delta}. \tag{7.1}$$

Here, $\frac{(1-R)\cdot F}{t}$ is the input energy density, with the laser fluence F, the reflectivity R and the absorption length t. As no theory for high-T_c superconductors is available the BCS-Theory is used to describe the Cooper pairs [118]. In its frame the binding energy of the Cooper pairs is the superconducting gap 2Δ. The number of Cooper pairs in the undisturbed superconductor at temperature T is

$$n_0 = \frac{N(E_F)\cdot\Delta(T)}{2}, \tag{7.2}$$

where $N(E_F) = 2.5$ states/eV/cell/spin is the volume density of states at the Fermi energy for $YBa_2Cu_3O_7$ [119]. The superconducting gap at 70 K can be estimated by $\Delta(T = 70\,\mathrm{K}) = 1.74 \cdot \Delta(0)\left[1 - \frac{T}{T_c}\right]^{\frac{1}{2}} \sim 12$ meV, where $\Delta(T = 0) = 15$ meV and $T_c = 90$ K were used. With the laser parameters used here ($R = 0.2$ [120], $F = 80\,\mu\mathrm{J/cm^2}$, $t = 100$ nm) all Cooper pairs are broken given that the entire laser energy is used for breaking the Cooper pairs. Even if only 1% of the laser energy is tranferred into broken pairs as suggested by Zhao et al. [63], a substantial fraction (20%) of the Cooper pairs will be broken.

7.1.2 Displacive excitation of coherent phonons

Following the model of Mazin et al. [60] for the optical response of superconductors, coherent optical phonons are excited upon the ultrafast breaking of Cooper pairs. This would, in principle, lead to a modification of the structure factor for the $YBa_2Cu_3O_7$ reflection. The reduced pairing energy E_{pair} must be compensated by a modified elastic energy E_{el} in order to maintain the energy balance:

$$0 = \delta E_{\mathrm{pair}} + \delta E_{\mathrm{el}} \tag{7.3}$$

For the pairing energy the BCS expression is used [118]:

$$E_{\mathrm{pair}} = \frac{1}{2} N \Delta^2, \tag{7.4}$$

where N is the volume density of states at the Fermi level and 2Δ is the superconducting gap, which in turn depends on the density of states at the Fermi level: $\Delta \sim \mathrm{e}^{-\frac{1}{\lambda}}$ with $\lambda \sim N$. A small variation of the pairing energy is connected with a small ionic displacement δQ.

$$\delta E_{\mathrm{pair}} = a\Delta^2 \frac{\mathrm{d}N}{\mathrm{d}Q} \delta Q, \tag{7.5}$$

where $a = \frac{1}{2} + \frac{1}{\lambda}$. The variation of elastic energy due to an ionic displacement δQ is

$$\delta E_{\mathrm{el}} = \hbar\omega \frac{\delta Q^2}{4}. \tag{7.6}$$

The dimensionless δQ is connected to a real space coordinate via $x = \delta Q \sqrt{\frac{\hbar}{2m\omega}}$. Inserting equations (7.5) and (7.6) into equation (7.3) yields an expression for δQ as a function of the variation of the density of states:

$$\delta Q = \frac{4a\Delta^2}{\hbar\omega} \cdot \frac{\mathrm{d}N}{\mathrm{d}Q} \tag{7.7}$$

With $\Delta(70\text{K}) \sim 12$ meV, $a \sim 2$ and $\frac{\mathrm{d}N}{\mathrm{d}Q} \sim 0.1$ states/eV/cell/spin for the Cu and Ba mode (obtained from frozen phonon calculations) [60], $\omega_{\mathrm{Cu}} = 150$ cm^{-1} and $\omega_{\mathrm{Ba}} = 120$ cm^{-1} [61], the displacement due to destruction of superconductivity results to

$$x \;=\; 3 \cdot 10^{-5} c \tag{7.8}$$

for both the copper and the barium mode. This would result in a change of integrated reflectivity of $\frac{\Delta R}{R} \sim 10^{-3}$ which is not detectable within the experimental capabilities used here. Therefore displacive excitation of coherent phonons can not account for the observed changes in the $YBa_2Cu_3O_7$ thin film.

7.1.3 Split models

As was already discussed in Section 2.1.3 structural as well as electronic inhomogeneities play an important role in high-T_c superconductors. Zigzag–like CuO chains, Cu(2) split position as well as the double well potential for the apical oxygen were introduced as possible structural inhomogeneities. It might be expected that upon breaking superconductivity the local structural distortions due to electronic inhomogeneities change and that this can be seen in the average crystallographic structure. As in the reported experiment only the $YBa_2Cu_3O_7$ 006 reflection was investigated, no possible distortions of the CuO chains which are located in b direction can be seen. However, the apical double well potential as well as the splitting of the Cu(2) site imply distortions in c directions.

The idea is that by optical Cooper pair breaking the valency of the planar copper ion or the apical oxygen ion may change which in turn determines the equilibrium position inside the unit cell. As suggested by Gutmann for the planar Cu(2) ion [30], the existence of two equilibrium positions is attributed to two different valence states. Thus, a change in the valence state, alters the occupation of the two possible sites for the oxygen or copper ion. The initial (unexcited) occupation numbers are taken from Mustre de Leon [28] and Gutmann [30]. Mustre de Leon found the two oxygen sites nearly equally occupied and separated by 0.13 Å, while Gutmann gave an occupation of the Cu(2) A-site of 85% and the two sites being separated by 0.18 Å[1]. To simplify the discussion and to account for experimental uncertainties of this study as well as the two cited works, for the following calculations it was assumed that the separation in both cases is $0.025\,c = 0.3$ Å. Thus the results represent certainly upper limits for the expected changes. The integrated reflectivities were calculated in the

[1] For the notation of the sites see Figure 2.9

Planar copper		Apical oxygen	
Occupation site A	$\frac{\Delta R}{R}$	Occupation site A	$\frac{\Delta R}{R}$
85%	0	50%	0
50%	-7%	0%	+4%
30%	-10%	100%	-4%
20%	-14%		
0%	-18%		

Table 7.1: Reflectivity change in dependence on the occupation of the two possible sites for the planar Cu(2) ion and the apical oxygen, respectively. Depopulation of the Cu(2) A-site from 85% to 30% can account for the observed decrease of integrated reflectivity. (The position of site A with respect to site B is given by $z_A = z_b - 0.025c$.)

frame of kinematic X-ray diffraction theory. Applying this diffraction theory to the thin films is certainly a good approximation. In Table 7.1 the reflectivity changes for different occupations of the sites for the 2 cases are shown. It is seen that by reduction of A-site occupation from 85% to 30% the observed reduction of integrated reflectivity can be explained. The double well potential model for the apical oxygen with the given initial occupation numbers of the two sites cannot explain the observation. If, however, initially the two sites are not equally occupied, but (almost) all atoms occupying site B, a complete redistribution into site A may account for the changes.

7.2 $SrTiO_3$

7.2.1 Strain distribution

The model, introduced above, may explain the changes in the $YBa_2Cu_3O_7$ thin film. But it does not provide an answer on why the $SrTiO_3$ 002 reflection is affected by the pumping process - even though it is not optically excited. As was already discussed in Section 6.3, strain waves are not appropriate for explaining the changes. An effect is sought that affects the whole probed $SrTiO_3$ volume, coherently. A clue is provided by the time-dependent rocking curves (see Figure 6.6): Upon pumping they are asymmetrically narrowed. The fact, that the linewidth decreases after pumping indicates that relaxation of an initially distorted region plays a decisive role. Again, relaxation due to modified lattice matching can not explain the time scales of the changes. The observation that the rocking curves are asymmetric and that the narrowing occurs mainly on the large angle side suggests that strain gradients are present

in the $SrTiO_3$ in c-direction and that these strain gradients are reduced upon excitation.

In this Section the strain profile shall be elucidated with the aim to draw conclusions from the exact form on a possible physical origin.

Different strain profiles were used to calculate the $SrTiO_3$ 002 reflection curve which was then compared to the measured one. Parameters of the strain profile were adapted in order to optimize the agreement between modelled and measured rocking curve. Calculation were performed in the frame of dynamical diffraction theory as described in Section 3.2.2. An example is shown in Figure 7.1. The strain profiles are shown in the inset. The profile is modelled by a

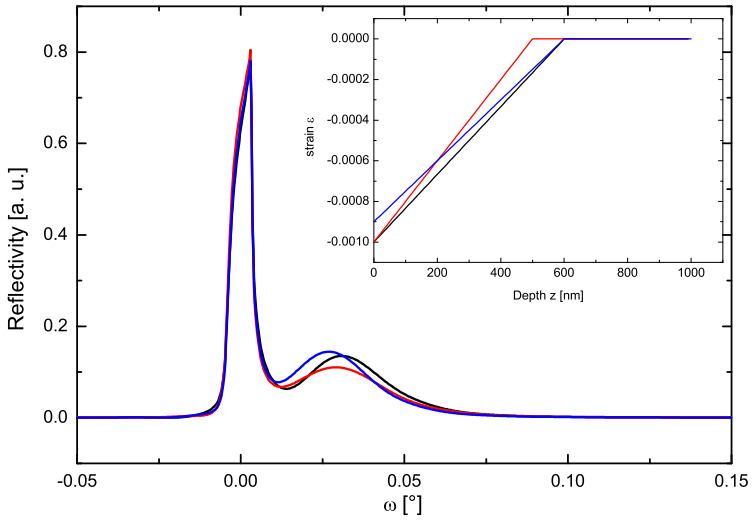

Figure 7.1: Intrinsic rocking curves for several strain distributions as shown in the inset.

linearly increasing strain starting with a negative value ϵ_0 at the interface to the $YBa_2Cu_3O_7$ ($z = 0$). At the depth $z = z_D$ the strain vanishes and remains zero. Three similar strain profiles with slightly different parameters and the resulting intrinsic rocking curves are shown. In all cases the rocking curves are dominated by a narrow intense peak originating from the unstrained bulk and a broader less intense peak originating from the strained volume. The peak value of the bulk part is determined by the thickness of the strained volume, i. e. the more expanded is the strained volume, the smaller is the peak value of the bulk contribution. On the other hand, as the thickness of the strained layer is increased, also the peak value of the associated peak increases. Increasing the absolute value of the initial strain ϵ_0 will shift the broader peak away from

the bulk contribution. The sign of the initial strain determines whether the strain contribution is on the large angle side or on the small angle side.
To compare this rocking curve with the measured one the apparatus function which is mainly given by the finite X-ray focal size must be taken into account. In this work a Gaussian function with a FWHM$\approx 0.05^\circ = 190$ arcsec was used. This is the angle under which the X-ray focus is seen by the detector.

Unpumped rocking curves

Figure 7.2 shows the calculated rocking curves for different strain distributions similar to those shown in Figure 7.1 and, for comparison, a measured rocking curve acquired without excitation of the sample. Error bars of the data points are too small to be seen. The peak values of all modelled data are normalized to

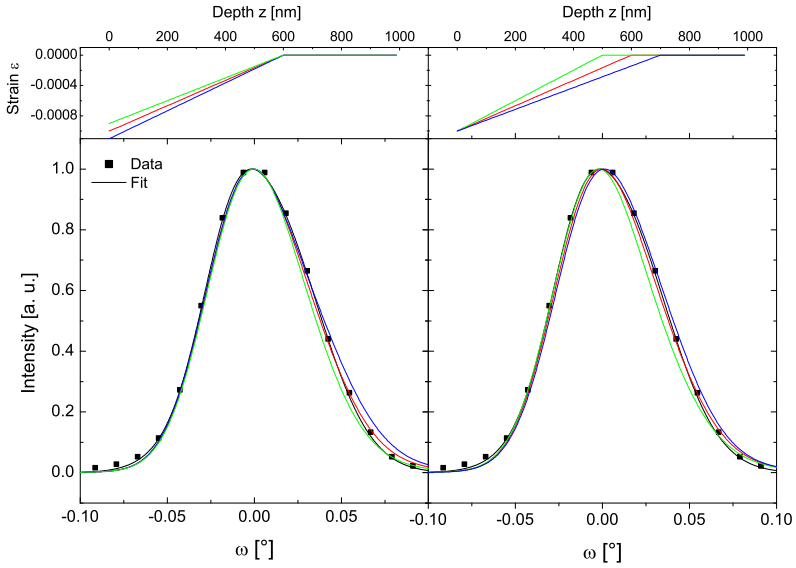

Figure 7.2: Modelled rocking curves for linear strain distributions as shown in the upper part.

1 as also in the experiment no statements on the maximum value could be given. The left part shows how the maximum strain influences the rocking curves. Here, the thickness of the strained layer is kept constant. In the right part the maximum strain is kept constant and the strained layer thickness is varied. Apparently the strain gradients are too small to account for a double peak structure of the rocking curve. However, increasing or decreasing the initial strain by only 10^{-4} results in distinctly broader or narrower rocking curves,

respectively. Also a variation of the strained layer thickness by only 100 nm clearly influences the rocking curve. By varying the peak strain, discrepancies appear at the lower part of the edge at the large angle side, while varying the thickness of the strained layer influences the whole side. Very good aggreement with the data is obtained for $z_D = 600$ nm and a maximum strain of $\epsilon_0 = -1.0 \cdot 10^{-3}$.
As the apparatus function is rather broad compared to the intrinsic $SrTiO_3$ 002 reflection curve, the sensitivity to the exact strain profile is not as good as the previously presented modelled rocking curves may imply. Very good agreement is also obtained for a step profile of the strain. This is shown in Figure 7.3. For four different strain values ($-1.0 \cdot 10^{-3}$, $-8 \cdot 10^{-4}$, $-6.5 \cdot 10^{-4}$ and $-5 \cdot 10^{-4}$) and different thicknesses of the strained surface layer the rocking curves were calculated. These modelled curves are compared with the measured rocking curves. While for $\epsilon_0 = -1 \cdot 10^{-3}$ the rocking curves features a double peak structure also for smaller thicknesses of the strained layer, in the other cases the strain leads only to a broadening. For $\epsilon_0 = -5 \cdot 10^{-4}$ the broadening is negligible and the resulting rocking curves are much narrower than the measured rocking curves. An excellent agreement with the data is obtained for a step like strain distribution with $\epsilon_0 = -6.5 \cdot 10^{-4}$ and $z_D = 600$ nm.
As the experimental accuracy is not sufficient to distinguish between the linear and the constant profile it is not necessary to use more complicated strain distributions.

Pumped rocking curve

It is not possible to reproduce the rocking curves acquired from the excited sample by strain profiles used for the unpumped case. This is examplified in Figure 7.4, where the modelled rocking curves for three different strain profiles and a measured rocking curve ($\Delta\tau = 600$ fs) are compared. As espected the agreement with the data at the low angle side is quite good for all modelled rocking curves, however significant deviations occur at the large angle side. That side of the measured rocking curve is best reproduced by a strain distribution with an interface strain $\epsilon_0 = -9 \cdot 10^{-4}$ and a strained layer thickness of $z_D = 400$ nm. Close to the maximum the agreement is insufficient for this strain profile. There, very good agreement is yielded for a steeper strain profile ($\epsilon_0 = -9 \cdot 10^{-4}$, $z_D = 300$ nm), but also for a vanishing strain, i. e. a perfect single crystal. Therefore it might be instructive to try modelling the measured rocking curve by two different contributing strain profiles of the form as before. And indeed this results in quite good agreement with the data. Rocking curves are again modelled for $\Delta\tau = 600$ fs. It is assumed that a fraction of the sample

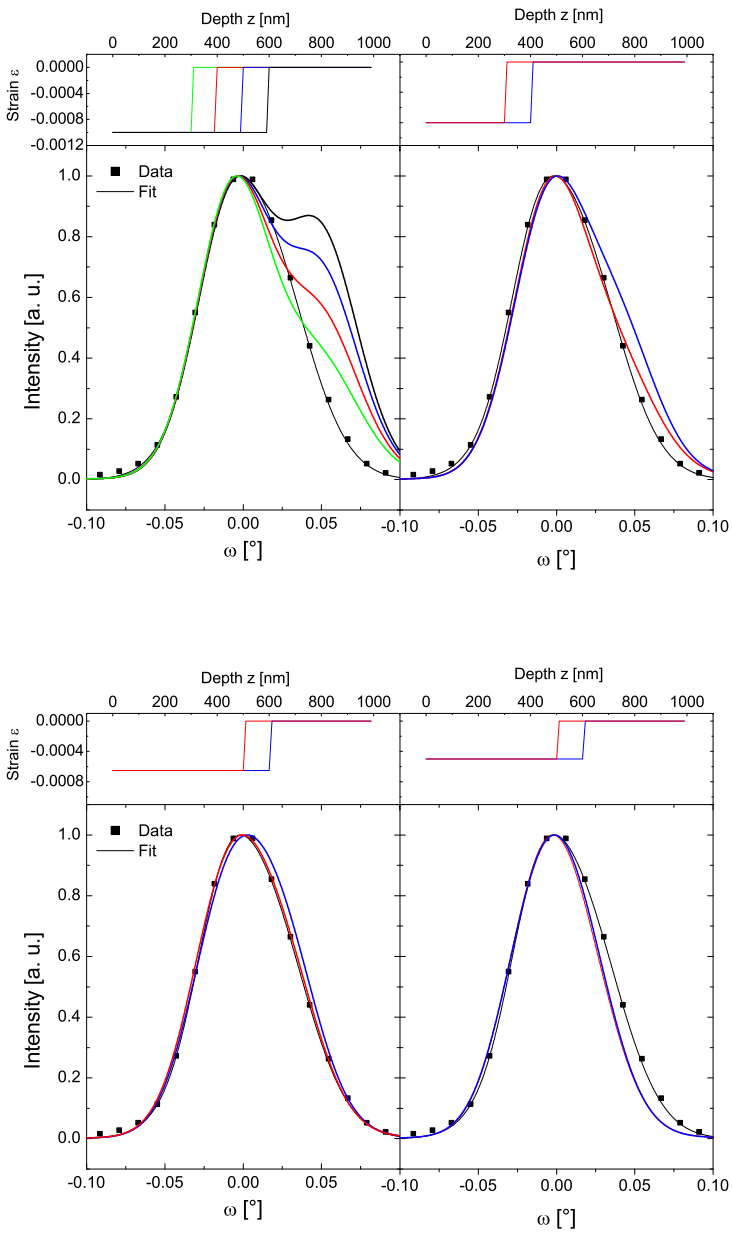

Figure 7.3: Modelled rocking curves for step-like strain distributions shown in the upper part.

is relaxed (R-fraction). Other parts remain in the strain situation as for the unpumped case (S-fraction). As will be shown below, good results are obtained when the ratio of the R-fraction to the total probed volume is assumed to be $\sim 50\%$. A possible scenario is sketched in Figure 7.5. Emphasis is placed to the fact that there is an inhomogeneous in-plane strain distribution. Such a lateral

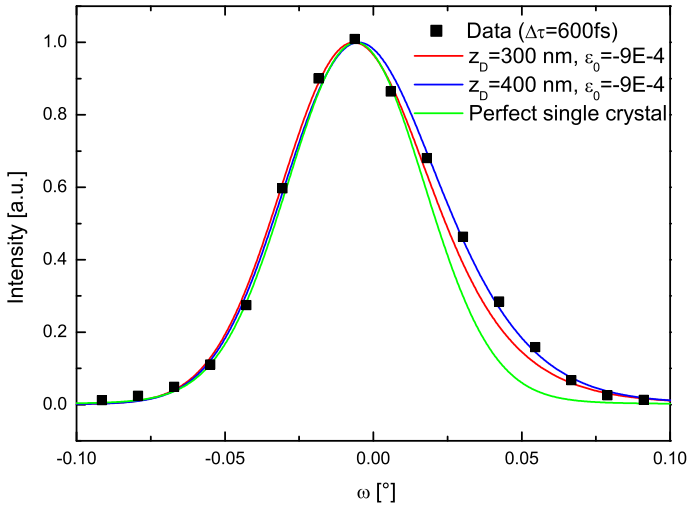

Figure 7.4: Modelled rocking curves for the pumped case ($\Delta\tau$ = 600 fs) for homogeneous, linear strain profiles.

inhomogeneous strain distribution can be explained if the probed sample volume is larger than the pumped volume. As the $SrTiO_3$ is not optically excited but changes are induced by the excitation of the $YBa_2Cu_3O_7$ thin film, the size of the pumped volume is not given by the pump pulse diameter, but by the width of the $YBa_2Cu_3O_7$ meander, i. e. 100 μm. The probe pulse focal spot size was mesured to be of the order of $100 \ldots 120\,\mu$m. As the angle of incidence for the X-rays is $\sim 45°$ the horizontal size (in dispersion plane) of the probed volume is enlarged by $\frac{1}{\sin 45°}$, amounting to $140 \ldots 170\,\mu$m. Thus, the ratio of covered to total probed $SrTiO_3$ area is in reasonably good agreement to acount for the lateral inhomogeneity.

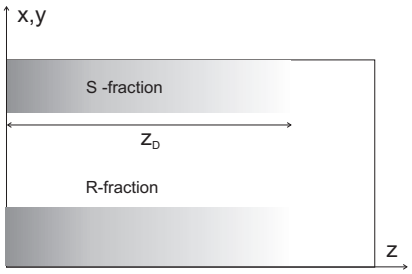

Figure 7.5: A possible inhomogeneous strain distributions for modelling the pumped rocking curves. The S-fraction of the sample remains strained as in the unpumped case, while the R-fraction relaxes.

It is not necessarily required that the relaxed volume is unstrained. Thus, using the strain profiles as for the unpumped exposure, there are three parameters that can be varied to find the best fit to the data:

- The ratio of relaxed to unchanged volume fraction R.
- The maximum strain for the relaxed case ϵ_0.
- The thickness of the strained layer in the relaxed volume fraction z_D.

As the two different strain distributions used for the unpumped case cannot be distinguished by the data, here the linear dependence of the strain on the thickness is used, e. g. the unmodified volume is characterized by $\epsilon_0 = -1 \cdot 10^{-3}$ and $z_D = 600$ nm. It turns out that an unstrained situation in the relaxed volume fraction yields a very good agreement with the data. In Figure 7.6, modelled rocking curves for this situation are shown together with the measured one. Error bars of the data points are smaller than the symbol size. For modelling the rocking curves the volume fraction was varied. Very good agreement is

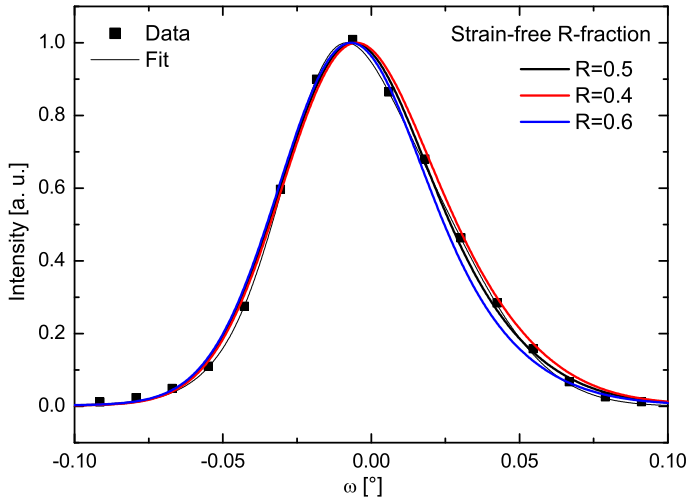

Figure 7.6: Modelled rocking curves for the pumped case and different ratios of strained and relaxed volume. The relaxed part is taken as strain-free.

obtained for the case that 50% of the volume has relaxed. Less modified volume overestimates the large angle side, while for a larger volume fraction of unstrained $SrTiO_3$ the small angle side becomes too important. The sensitivity of the experiment is not good enough to decide whether the modified region is indeed unstrained or whether the volume remains slightly strained as associated

changes of the rocking curves are tiny. In Figure 7.7 the experimentally acquired rocking curve is compared with the partially strain-free situation as well as for the case that the modified volume remains slightly strained ($\epsilon_0 = -5 \cdot 10^{-4}$, $z_D = 300$ nm). This is approximately the strain that the data can exclude.

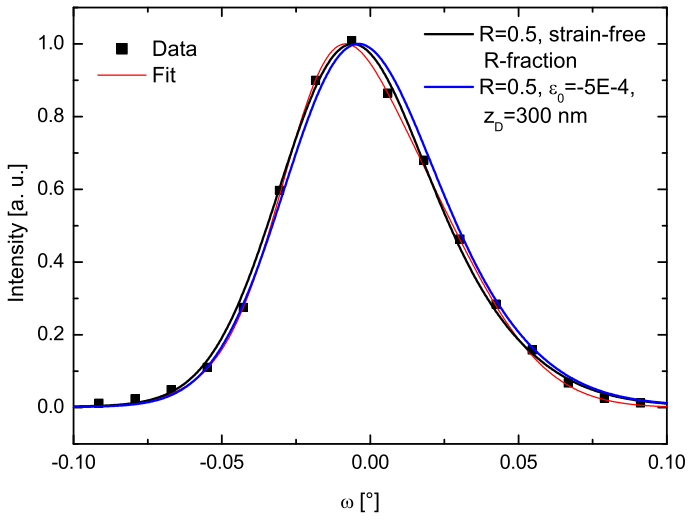

Figure 7.7: Modelled rocking curves for the pumped case and different strain situations in the relaxed volume fraction. It was assumed that 50% of the volume has relaxed upon excitation.

Smaller strains or less expanded strained regions yield about as good agreement with the data as the strain-free case.
So far, attention was paid to the shape of the rocking curve and for the sake of clarity the modelled curves were shifted as to provide an overlap as good as possible with the measured rocking curve. Now it will be shown that with the previously introduced model also the shift of the peak is well reproduced. This is shown in Figure 7.8, where the (unshifted) modelled rocking curves for the unpumped and a pumped case($\Delta\tau = 600$ fs) are directly compared. The shift of the peak amounts to about $\Delta\omega = 0.005°$ which is in very good agreement with the measured peak shift. Moreover, in Figure 7.8 the two rocking curves were not normalized. As they both result from the convolution of the intrinsic rocking curves with the same apparatus function the maxima can be compared even though this was not possible in the experiment. It can be seen that the maximum of the unpumped rocking curve is higher and it is reduced upon excitation. This is a very important finding for the interpretation of the time dependent data of $YBa_2Cu_3O_7$: With the measured $SrTiO_3$ peak val-

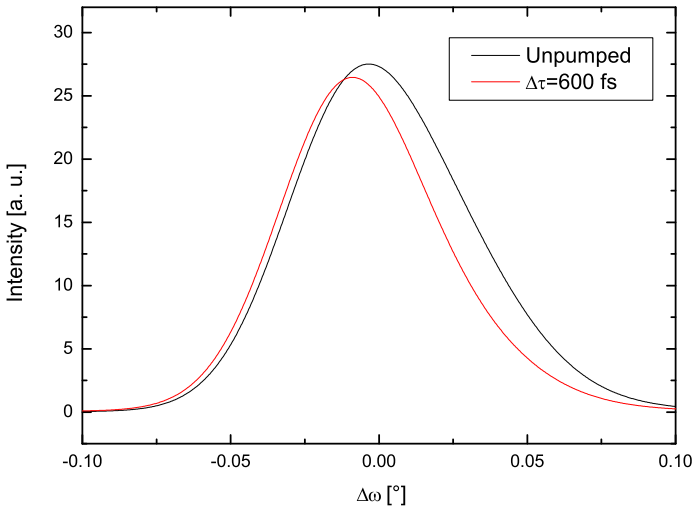

Figure 7.8: Modelled unpumped and pumped rocking curve ($\Delta\tau = 600$ fs).

ues scaled to one, the integrated reflectivity as well as the peak value of the $YBa_2Cu_3O_7$ 006 reflection were reduced upon excitation. If the model used to derive the peak value of the $SrTiO_3$ 002 reflection holds then the reduction of the $YBa_2Cu_3O_7$ values is true and even larger.

Summary

For the unpumped case the measured rocking curve can be well modelled by assuming that a surface layer of thickness z_D is homogeneously strained, where both, a linear depth dependence of the strain and a constant strain yield excellent agreement with the data.
The strain distribution of the excited $SrTiO_3$ is more complicated. A single strain profile as for the unpumped case is not sufficient to model the data. However, assuming that only a fraction of the probed volume has indeed relaxed upon excitation yields good agreement with the data. In about 50% of the probed $SrTiO_3$ volume the strain is strongly reduced and might even vanish.

7.2.2 Microscopic origin

Part of the strain profile used to model the measured rocking curve might be explained by the epitaxial strain induced by the $YBa_2Cu_3O_7$ thin film into the substrate. However, as the in-plane lattice constant of $YBa_2Cu_3O_7$ is smaller than the in-plane lattice constant of $SrTiO_3$ the epitaxial strain leads to an

in-plane compression and subsequently to an out-of plane expansion, thus a positive strain in c direction. As the measured rocking curve is mainly explained by a negative strain, the tension induced by the $YBa_2Cu_3O_7$ can not account for the observed rocking curve profile. Also the expansive stress induced by dislocations [121, 122] can not explain the rocking curve profile, neither does the existence of twin domains. The reasons are the following:

1. As shown in Section 5 and measured also by Cao et al. [70] the longer c-axis in the low-temperature tetragonal phase of $SrTiO_3$ is less populated. Therefore an insufficient angular resolution would indeed result in asymmetric rocking curves - however, the steeper side should be the large angle side which is in contradiction with the data.

2. Lötzsch [79] has shown that in the thin near surface region the tetragonal relaxation in the low-T phase of $SrTiO_3$ is suppressed if it is covered by a thin $YBa_2Cu_3O_7$ film, thus no twin domains are expected at all.

To elucidate the physical origin of this strain distribution as well as its response to an excitation of the $YBa_2Cu_3O_7$ thin film one has to study the situation at the interface between the film and the substrate. Their electrical contact gives rise to band bending and therefore to rather strong electric fields inside the substrate. This situation is schematically and in a very simplified way shown in Figure 7.9. The work function of the $YBa_2Cu_3O_7$ strongly depends on the exact

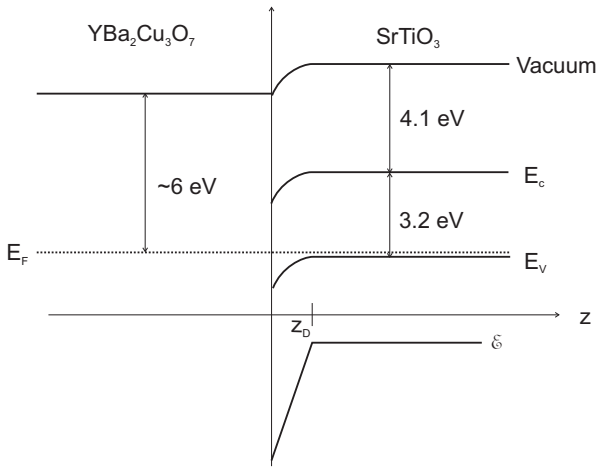

Figure 7.9: Band diagramm of the sample.

oxygen concentration and is not well known. The first few layers of the film are thought to be oxygen deficient due to oxygen diffusion into the substrate. The work function of oxygen deficient $YBa_2Cu_3O_7$ ranges from 6.3 to 7.5 eV,

for fully oxygenated $YBa_2Cu_3O_7$ it amounts to 5.2-6.0 eV [123]. As the Fermi level is a global quantity and the whole sample is in thermodynamic equilibrium here a value of 6.0 eV was assumed. This is supported by work of Große which implies a difference in work function W_A between the values of $YBa_2Cu_3O_7$ and Au ($W_A = 5.1 \pm 0.1$ eV [124]) of about $1.0 \ldots 1.2$ eV [125]. $SrTiO_3$ is a wide-band p-type semiconductor ($E_g \sim 3.2$ eV). At $T \sim 100$ K, the Fermi level lies about 0.2 eV above the valence band edge E_V. The electron affinity is about 4.1 eV [126]. This determines the difference in work function to be ~ 1 eV, giving rise to space charge regions and band bending. A Schottky contact is formed. While in $YBa_2Cu_3O_7$ the electrostatic potential is rapidly shielded by the larger number of carriers resulting in depletion layer thicknesses of the order of the Debye length, in $SrTiO_3$ the depletion layer is much more extended. It is given by [127]

$$z_D = \sqrt{\frac{2\epsilon\epsilon_0}{eN} U_K}, \tag{7.9}$$

where ϵ is the dielectric constant of $SrTiO_3$, ϵ_0 is the permittivity of free space, N is the carrier density and e the elemantary charge. The contact potential U_K is given by $U_K = \frac{1}{e}(E_F^{SrTiO_3} - E_F^{YBa_2Cu_3O_7}) \sim 1$ V. The electric field $\mathcal{E}$ associated with the space charge in $SrTiO_3$ depends linearly on the distance to the interface:

$$\mathcal{E} = \begin{cases} \frac{e}{\epsilon\epsilon_0} N(z_D - z) & \text{for} \quad 0 < z < z_D \\ 0 & \text{for} \quad z > z_D \end{cases} \tag{7.10}$$

Using the bulk value of the dielectric constant at 70 K, $\epsilon = 2500$ [128] and a carrier density of the order of 10^{17} cm^{-3} yields a depletion layer thickness of 1.7 μm and a maximum field strength of $\mathcal{E}(x = 0) = 1 \cdot 10^6$ V/m. Lötzsch has shown that a thin surface layer of single crystalline $SrTiO_3$ covered with $YBa_2Cu_3O_7$ behaves like a thin film due to epitaxial strains [79]. As with Ti-Kα radiation (used also by Lötzsch) only a thin surface layer is investigated, the same situation also occurs in the present work. Thus, not the dielectric constant of bulk $SrTiO_3$ but the more appropriate value of a thin $SrTiO_3$ film must be used, which is unfortunately very sample dependent. Fuchs et al. report dielectric constants of $SrTiO_3$ thin films sandwiched between $YBa_2Cu_3O_7$ electrodes as high as 5000 at about 90 K for zero bias electric field. Fields of the order of 10^6 V/m reduce the dielectric constant by about 1000. They find a paraelectric to ferroelectric phase transition with a Curie temperature of about 90 K that is increased by a bias electric field [75]. Christen et al. found dielectric constants of the order of 100 at 100 K [129]. Große et al. [125] found thickness dependent values for the dielectric constant due to space charge regions and corresponding

thickness dependent internal electric fields. For a thin film thickness of the order of 250 nm they measured a maximum dielectric constant of ~ 700 at about 100 K. The situation in the present work is complicated by the fact that the thin film behaviour of $SrTiO_3$ is induced by epitaxial strain due to the $YBa_2Cu_3O_7$ thin film. There is no real thin $SrTiO_3$ film. Choosing one of the above values of the dielectric constant for the case considered here is therefore arbitrary. However, the dielectric constant of the surface layer of the $SrTiO_3$ substrate will be of the order of several hundreds. In Figure 7.10 the depletion layer thickness and the maximum electric field strength are plotted in dependence on the dielectric constant for various carrier densities. The solid lines show the depletion layer

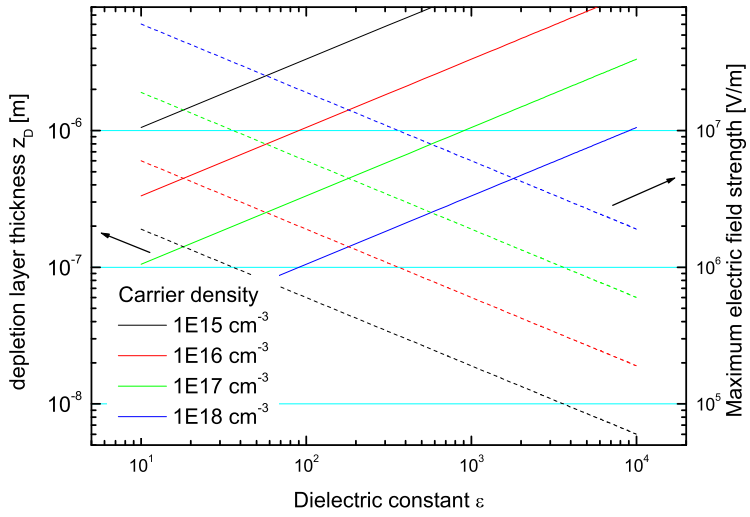

Figure 7.10: Depletion layer thickness and maximum electric field strength in dependence on the dielectric constant for different carrier densities in $SrTiO_3$.

thickness and the dashed lines represent the maximum electric field strength. The precise carrier density is unknown. The bulk carrier density of high quality $SrTiO_3$ single crystals is quite low. Values of the order of $10^{15} \ldots 10^{16}$ cm^{-3} are reported [123]. However the near surface region is subjected to an increased defect density. One may therefore expect a higher carrier density in the surface near region of the $SrTiO_3$ substrate. In Figure 7.10 carrier densities between $10^{15} \ldots 10^{18}$ cm^{-3} were considered, the density of 10^{15} cm^{-3} being certainly too small. Thus, the previously discussed large parameter space determines a maximum internal field strength on the order of $\sim 10^6 \ldots 10^7$ V/m and a depletion layer thickness on the order of $z_D \sim 100 \ldots 1000$ nm.
Obviously, not only the dielectric constant must be taken for a thin film, one

has also to take into account that in thin films a paraelectric to ferroelectric transition occurs at finite temperatures [75]. Since ferroelectrics are piezoelectric the internal field gradient is connected with a strain gradient. No data on the piezoelectric coefficient of thin $SrTiO_3$ films is available. Therefore for an estimation of the strain the coefficient of $BaTiO_3$ is used, which is a material very similar to $SrTiO_3$ but becomes ferroelectric already at 120° C. The relevant coefficient amounts to $d_{333} = 90 \cdot 10^{-12}$ m/V [130]. This value holds for room temperature which is much smaller than the Curie temperature, i. e. the temperature dependence is negligible.
In the present case the exact Curie temperature is unknown. For thin $SrTiO_3$ films in between two $YBa_2Cu_3O_7$ electrodes Fuchs et al. determined the Curie temperature for zero bias electric field to be about 90 K. The Curie temperature however is very sensitive to strain and electric fields. Thus the Curie temperature is strongly sample dependent.
Using the room temperature piezoelectric coefficient of $BaTiO_3$, the maximum strain due to piezoelectric effect is on the order of $\epsilon \sim 10^{-4} \ldots 10^{-3}$. The strain has the same dependence on depth as the electric field and, thus, vanishes at z_D. These results are in reasonably good agreement with the linear strain distribution used to model the unpumped data.

Pumped data

The measured rocking curve of the excited sample is modelled by assuming that 50% remains in the unexcited state and the other 50% has relaxed, i. e. are perfect single-crystalline. The time scales at which the crystallographic properties change does not permit major atomic redistributions such as formation of twin domains. As the strain in the unpumped situation originates from an electric field due to band bending, a fast relaxation process may be due to a change of contact potential or a superposition with another field. The fact that a substantial fraction of the $SrTiO_3$ remains in its initial state sheds light on the possible microscopic origin of the changes. The pump pulse diameter was chosen to be larger than the probe pulse diameter which in turn was larger than the width of the $YBa_2Cu_3O_7$ meander due to its large angle of incidence (45°). The covered fraction of the probed volume was about 40% and thus smaller than the ratio of the relaxed volume to the total probed volume as determined by adapting the strain distribution. However, in light of the uncertainties of the strain distribution, this is a reasonable agreement. From this it can be concluded, that the crystallographic changes in $SrTiO_3$ are indeed induced by changes in $YBa_2Cu_3O_7$. On the exact mechanism leading to the observed fast strain release one may only speculate up to now. However, at this point a pos-

sible mechanism is proposed:
As proposed in Section 7.1.3 Cooper pair breaking is closely related to a repopulation of the two possible sites for the Cu(2) planar ion or the apical oxygen ion due to a valence state change. This in turn will modify the geometry of the charge stripes (see Section 2.1.3). Perali et al. have suggested that this will firstly shift electronic levels and, secondly, possibly destroy superconductivity [48]. The shift of electronic levels will directly influence the conditions at the interface to the substrate and thus the band bending. A reduction of the difference of Fermi levels, i. e. the contact potential will lead to a decrease of both, the electric field and the depletion layer thickness (see eq. (7.9) and (7.10)). Consequently, the strain induced by piezoelectricity and the thickness of the strained layer is reduced.
In static measurements, such a structural response of the $SrTiO_3$ substrate may only be observed when passing through the paraelectric to ferroelectric phase transition. The electronic changes at the interface are proposed to be caused by an optically modified stripe geometry in $YBa_2Cu_3O_7$, which also suppresses superconductivity. Thermal Cooper pair breaking, however, leaves the stripe geometry unaffected and therefore does not influence the contact potential between thin film and substrate significantly.

Static measurements

The static measurements introduced in Section 5 support the model suggested above: In Section 5 the occurence of additional peaks in the diffraction signal was interpreted as hint for strain induced into the substrate by entering the superconducting state. However, it can also be interpreted by strain due to piezoelectricity resulting from band bending in a thin ferroelectric surface layer of the $SrTiO_3$ substrate. In this case there would be a (near) coincidence of superconducting transition temperature and Curie temperature. As was already mentioned, the exact Curie temperature is strongly sample dependent. Fuchs et al. measured a value of 90 K for zero bias field [75]. Further support comes from the disappearence of the additional peaks after several cooling cycles. Ferroelectricity is induced in the substrate by the epitaxial strain from the thin $YBa_2Cu_3O_7$ layer. Very good clamping is required to induce ferroelectricity. Due to the structural phase transition of the substrate at 105 K and different coefficients of thermal expanison of thin film and substrate much stress is introduced into the sample (both in the thin film and in the substrate) during a cooling cycle. After a critical stress is reached (possibly only after several cycles) it is released by formation of dislocations which will reduce the clamping of the thin film and thus destroy the ferroelectric behaviour.

This explains not only the disappearence of the additional peaks in the static diffraction signal but also the disappearence of the time-dependent diffraction signal after few cooling cycles.

8 Summary and Outlook

In this PhD thesis time-resolved X-ray diffraction in optical pump - X-ray probe scheme was applied for the first time to a High-Temperature Superconductor in the superconducting state. The aim was to study the possible lattice response to optical Cooper pair breaking. As sample a thin $YBa_2Cu_3O_7$ film with a superconducting transition temperature of T_c=90 K, epitaxially grown on a $SrTiO_3$ single crystal was used. The time-resolved experiments were performed at a laser-produced plasma X-ray source emitting ultrashort X-ray bursts in the full solid angle. The use of a titanium tape target allowed for exploiting the full repetition rate of the laser system of 10 Hz. This was a prerequisite for a high dynamic range of the acquired diffraction data.
The use of a well-characterized toroidally bent GaAs crystal permitted very sensitive measurements of changes in the rocking curve shape and of the Bragg angle. Bragg angle shifts as small as ~ 4 arcsec could be detected, which would correspond to a strain of $\frac{\Delta d}{d} \sim 2 \cdot 10^{-5}$.

In the frame of this PhD thesis an experimental setup was implemented combining a goniometer with a commercial Stirling machine. Temperatures as low as 70 K were achievable. Diffraction signals were acquired both from the thin film and the substrate.

In a first experiment static temperature dependent rocking curves were acquired. For temperatures $T \leq 92$ K the diffraction data reflect the presence of tetragonal domains in $SrTiO_3$. With the onset of superconductivity, for $T \leq 88$ K a number of additional peaks appear for one sample. These are modeled by a linear strain profile in one kind of the $SrTiO_3$ domains. It is suggested that a thin near-surface region in $SrTiO_3$ behaves like a thin film and becomes ferroelectric. The strain originates from a piezoelectric behaviour due to large electric fields close to the $SrTiO_3/YBa_2Cu_3O_7$ interface resulting from Fermi level alignment.
It is found that the temperature dependence of the diffraction profiles is strongly sample dependent and changes upon repeated heating and cooling.

In a second step, time-resolved X-ray diffraction experiments were performed with a well characterized sample. Similar pump pulse parameters as in all-optical studies (1.55 eV photon energy, $80\mu J/cm^2$ flux, 80 fs pulse duration)

were chosen to break all or a large fraction of the Cooper pairs.
While in the frame of experimental accuracy ($\Delta\theta \approx 5$ arcsec and $\Delta\omega \approx 15$ arcsec for the $YBa_2Cu_3O_7$ reflection) no changes of the $YBa_2Cu_3O_7$ peak position and rocking curve width are detected, there are indications for a change of integrated reflectivity ($\sim 10\% \pm 5\%$). Nevertheless, the integrated reflectivity was only measured relative to the peak reflectivity of the substrate. This makes the discussion of the effect difficult. A reduction of integrated reflectivity combined with unchanged peak position and peak width means that the structure factor is altered upon excitation. The observed changes take place on time scales of a few ps in agreement with the expected quasiparticle relaxation times in $YBa_2Cu_3O_7$.
It is shown that an effect of this order of magnitude cannot be explained by the displacive excitation of coherent phonons commonly used to discuss optical pump probe data on High-Temperature Superconductors. Alternatively it is proposed that the change in Cooper pair density is accompanied by a valence change of the planar Cu(2) atom leading to local structural changes, i. e. modified buckling of the CuO_2 planes.

To the best of my knowledge this study showed for the first time structural changes in the substrate induced by changes in the thin film measured with sub-ps time resolution. It is stressed that the substrate itself is not optically excited. Nevertheless, the optical pump – X-ray probe experiment revealed distinct modifications in the diffraction signal of $SrTiO_3$. A shift towards smaller Bragg angles ($\Delta\theta \approx 30$ arcsec) as well as an asymmetric narrowing of the rocking curve, i. e. a decrease of rocking curve width ($\Delta\omega \approx 25$ arcsec) accompanied by a change of rocking curve shape, are reported. The measured changes are well above the experimental uncertainties ($\Delta\theta \approx 4$ arcsec and $\Delta\omega \approx 8$ arcsec for the $SrTiO_3$ reflection).
No experimental conclusions could be drawn on possible changes of the integrated reflectivity.

In the unexcited states the rocking curves show a remarkable asymmetry which is reduced upon excitation. A strain in the $SrTiO_3$-$YBa_2Cu_3O_7$ interface region was modeled to account for the observed unexcited rocking curve. Good agreement is obtained for a linearily increasing strain profile with a maximum negative strain at the interface of $-1 \cdot 10^{-3}$ and a strained layer thickness of about 600 nm. To explain this strain profile the epitaxial strain induced thin film behaviour of a thin near surface region in $SrTiO_3$ is used as in case of the static temperature-dependent measurements. An estimation of the expected strain profile is consistent with the profile obtained by fitting the measured rocking curve.

The observed changes following excitation in the $SrTiO_3$ rocking curve are discussed in terms of modified electronic conditions at the interface due to electronic changes in $YBa_2Cu_3O_7$. A reduction of contact potential reduces both, the maximum electric field at the interface and the depletion layer thickness, and therefore the strain profile.

To gain further experimental support for or to disprove the suggested model a variety of further experiments are necessary: To identify the role of the possible ferroelectric transition of a thin surface layer of the $SrTiO_3$ substrate the experiment should be repeated with both, a substrate that does not become ferroelectric, e. g. $LaAlO_3$, and a substrate that is ferroelectric, e. g. $BaTiO_3$. To obtain the required good clamping between film and substrate maybe different superconducting thin films have to be used.

To understand the role of Cooper pairs for the observation it is important to repeat the experiment at different temperatures below and above the superconducting transition. If the signal follows the Cooper pair density, this will prove that superconductivity is directly involved in the mechanism leading to these observations.

Whether superconductivity is indeed a necessity or whether similar effects can be observed with other thin films is a question that might be more difficult to answer. The time scales being involved in the underlying mechanism may be completely different for superconductors and semiconductors for example. Further, the accessibility of free states by the absorption of one pump photon must be ensured.

If there is no correlation between the onset of superconductivity and the lattice response of the substrate it can also mean that the present local inhomogeneities (stripe order) rather than superconductivity is responsible for the observations. This can be investigated in more detail by using layered nickelates that are not superconducting but which exhibit a stripe phase [131].

This work has shown that if one wants to study a possible lattice response in a high-T_c superconductor to ultrafast breaking of Cooper pairs it is extremely important to use a well characterized substrate for the thin film. As the expected response from the high-T_c sample is very small, any variation of the substrate should be either smaller or extremely well understood.

Bibliography

[1] C. Rischel et al. *Nature*, **390**: 490, 1997

[2] C. Rose-Petruck et al. *Nature*, **398**, 1999

[3] C. W. Siders et al. *Science*, **286**: 1340, 1999

[4] A. Cavalleri et al. *Phys. Rev. Lett.*, **87**: 237401, 2001

[5] A. Rousse et al. *Nature*, **410**: 65, 2001

[6] K. Sokolowski-Tinten et al. *Phys. Rev. Lett.*, **87**: 225701, 2001

[7] T. Feurer et al. *Phys. Rev. E*, **65**: 016412, 2002

[8] K. Sokolowski-Tinten et al. *Nature*, **422**: 287, 2003

[9] M. Bargheer et al. *Science*, **306**: 1771, 2004

[10] A. Morak et al. *phys. stat. sol. (b)*, **243**: 2728, 2006

[11] J. G. Bednorz et al. *Z. Phys. B*, **64**: 189, 1986

[12] M. K. Wu et al. *Phys. Rev. Lett.*, **58**: 908, 1987

[13] K. Yvon et al. *Z. Phys. B*, **76**: 413, 1989

[14] A. Damascelli et al. *Rev. Mod. Phys.*, **75**: 473, 2003

[15] J. L. Tallon et al. *Phys. Rev. B*, **51**: 12911, 1995

[16] B. Büchner et al. *Phys. Rev. Lett.*, **73**: 1841, 1994

[17] O. Chamissem et al. *Nature*, **397**: 45, 1999

[18] J. D. Jorgensen et al. *Phys. Rev. B*, **41**: 1863, 1990

[19] A. R. Moodenbaugh et al. *Phys. Rev. B*, **38**: 4596, 1988

[20] D. M. Paul et al. *Phys. Rev. Lett.*, **58**: 1976, 1987

[21] P. M. Horn et al. *Phys. Rev. Lett.*, **59**: 2772, 1987

[22] R. Srinivasan et al. *Phys. Rev. B*, **38**: 889, 1988

[23] A. J. Millis et al. *Phys. Rev. B*, **38**: 8908, 1988

[24] H. You et al. *Phys. Rev. B*, **43**: 3660, 1991

[25] C. Meingast et al. *Phys. Rev. Lett.*, **67**: 1634, 1991

[26] W. Dmowski et al. *Phys. Rev. Lett.*, **61**: 2608, 1988

[27] B. H. Toby et al. *Phys. Rev. Lett.*, **64**: 2414, 1990

[28] J. Mustre de Leon et al. *Phys. Rev. Lett.*, **65**: 1675, 1990

[29] A. Bianconi et al. *Phys. Rev. Lett.*, **76**: 3412, 1996

[30] M. Gutmann et al. *Phys. Rev. B*, **61**: 11762, 2000

[31] J. R. Hardy et al. *Phys. Rev. Lett.*, **60**: 2191, 1988

[32] M. Francois et al. *Sol. State Comm.*, **66**: 1117, 1988

[33] J. Mustre de Leon et al. *Phys. Rev. B*, **45**: 2447, 1992

[34] J. D. Sullivan et al. *Phys. Rev. B*, **48**: 10638, 1993

[35] A. Bianconi et al. *Phys. Rev. B*, **54**: 10218, 1996

[36] A. Yamamoto et al. *Phys. Rev. B*, **42**: 4228, 1990

[37] A. I. Beskrovnyi et al. *Physica C*, **166**: 79, 1990

[38] A. I. Beskrovnyi et al. *Physica C*, **171**: 19, 1990

[39] M. Onoda et al. *Sol. State Comm.*, **67**: 799, 1988

[40] W. A. Groen et al. *Sol. State Commun.*, **68**: 527, 1988

[41] P. G. Radaelli et al. *Phys. Rev. B*, **48**: 499, 1993

[42] E. D. Isaacs et al. *Phys. Rev. Lett.*, **72**: 3421, 1994

[43] J. M. Tranquada et al. *Nature*, **375**: 561, 1995

[44] H. A. Mook et al. *Nature*, **404**: 729, 2000

[45] R. P. Sharma et al. *Nature*, **404**: 736, 2000

[46] S. A. Kivelson et al. *Nature*, **393**: 550, 1998

[47] J. Zaanen. *Science*, **286**: 251, 1999

[48] A. Perali et al. *Sol. State comm.*, **100**: 181, 1996

[49] N. L. Saini et al. *Phys. Rev. Lett.*, **79**: 3467, 1997

[50] J. M. Chwalek et al. *Appl. Phys. Lett.*, **57**: 1696, 1990

[51] S. G. Han et al. *Phys. Rev. Lett.*, **65**: 2708, 1990

[52] C. J. Stevens et al. *Phys. Rev. Lett.*, **78**: 2212, 1997

[53] V. V. Kabanov et al. *Phys. Rev. B*, **59**: 1497, 1999

[54] R. A. Kaindl et al. *Science*, **287**: 470, 2000

[55] R. D. Averitt et al. *Phys. Rev. B*, **63**: 140502, 2001

[56] R. Rosei et al. *Phys. Rev. B*, **5**: 3883, 1972

[57] V. Z. Kresin et al. *J. Supercond.*, **1**: 327, 1988

[58] N. W. Ashcroft et al. *Solid state physics* (Saunders College, 1976)

[59] D. H. Reitze et al. *Phys. Rev. B*, **46**: 14309, 1992

[60] I. I. Mazin et al. *Phys. Rev. B*, **49**: 9210, 1994

[61] W. Albrecht et al. *Phys. Rev. Lett.*, **69**: 1451, 1992

[62] H. J. Zeiger et al. *Phys. Rev. B*, **45**: 768, 1992

[63] Y. G. Zhao et al. *J. Supercond.*, **12**: 675, 1999

[64] E. Li et al. *Phys. Rev. B*, **65**: 184519, 2002

[65] F. A. Hegmann et al. *Phys. Rev. B*, **48**: 16023, 1993

[66] M. J. Holcomb et al. *Phys. Rev. B*, **53**: 6734, 1996

[67] H. A. Mook et al. *Phys. Rev. Lett.*, **70**: 3490, 1993

[68] R. J. McQueeney et al. *Phys. Rev. Lett.*, **82**: 628, 1999

[69] E. Dagotto et al. *Science*, **271**: 618, 1996

[70] L. Cao et al. *Phys. Stat. Sol. (a)*, **181**: 387, 2000

[71] G. Shirane et al. *Phys. Rev.*, **177**: 858, 1969

[72] K. A. Müller et al. *Phys. Rev. B*, **19**: 3593, 1979

[73] J. Hemberger et al. *Phys. Rev. B*, **52**: 13159, 1995

[74] H. Uwe et al. *Phys. Rev. B*, **13**: 271, 1976

[75] D. Fuchs et al. *J. Appl. Phys.*, **85**: 7362, 1999

[76] J. H. Haeni et al. *Nature*, **430**: 758, 2004

[77] D. E. Grupp et al. *Science*, **276**: 392, 1997

[78] T. Komoto et al. *Phys. Rev. B*, **74**: 064303, 2006

[79] R. Lötzsch. *Erprobung eines Helium-Durchfluss-Kryostaten für zeitaufgelöste Röntgenbeugungsexperimente.* Master thesis, Friedrich-Schiller University Jena, 2006

[80] A. Heidemann et al. *Z. Physik*, **258**: 429, 1973

[81] Q. Hui et al. *J. Phys.: Condens. Matter*, **17**: 111, 2005

[82] F. He et al. *Phys. Rev. B*, **70**: 235405, 2004

[83] M. von Laue. *Röntgenstrahlinterferenzen* (Akademische Verlagsgesellschaft, Frankfurt, 1960)

[84] S. Takagi. *Acta Cryst.*, **15**: 1311, 1962

[85] S. Takagi. *J. Phys. Soc. Jap.*, **26**: 1239, 1969

[86] D. Taupin. *Bull. Soc. Fr. Miner. Crist.*, **87**: 469, 1964

[87] A. Authier. *Dynamical Theory of X-ray diffraction* (Oxford University Press, 2001)

[88] J. Wark et al. *Phys. Rev. B*, **40**: 5705, 1989

[89] Z. Chang et al. *Appl. Phys. Lett.*, **69**: 133, 1996

[90] J. Larsson. *Opt. Lett.*, **26**: 295, 2001

[91] R. W. Schoenlein et al. *Science*, **287**: 2237, 2000

[92] E. Seres et al. *Appl. Phys. Lett.*, **89**: 181919, 2006

[93] R. W. Schoenlein et al. *Science*, **274**: 236, 1996

[94] C. Ziener. *Aufbau eines 12 TW Titan:Saphir-Lasers zur effizienten Erzeugung charakteristischer Röntgenstrahlung.* Ph.D. thesis, Friedrich-Schiller-University, Jena, 2001

[95] N. Zhavoronkov et al. *Opt. Lett.*, **30**: 1737, 2005

[96] F. Zamponi et al. *Rev. Sci. Instr.*, **76**: 116101, 2005

[97] A. Lübcke et al. *Appl. Phys. B*, **80**: 801, 2005

[98] T. Missalla et al. *Rev. Sci. Instr.*, **70**: 1288, 1999

[99] M. Bargheer et al. *Appl. Phys. B*, **80**: 715, 2005

[100] I. Uschmann et al. *Appl. Optics*, **44**: 5069, 2005

[101] M. S. del Rio et al. Computer Program XOP (X-ray oriented Programs)

[102] O. Wehrhan et al. Berechnungen für verschiedene gebogene Kristalle, 2004. Private communications

[103] E. Förster et al. *Rev. Sci. Instr.*, **63**: 5012, 1992

[104] I. Golovkin et al. *Phys. Rev. Lett.*, **88**: 0450021, 2002

[105] O. Renner et al. *Rev. Sci. Instr.*, **68**: 2393, 1997

[106] K. Fujita et al. *Rev. Sci. Instr.*, **72**: 744, 2001

[107] M. Vollbrecht et al. *J. Quant. Spectr. Radiat. Transfer*, **58**: 965, 1997

[108] E. Förster et al. *Appl. Opt.*, **36**: 831, 1997

[109] I. Uschmann et al. *Appl. Opt.*, **39**: 5865, 2000

[110] C. Reich et al. *Phys. Rev. E*, **68**: 056408, 2003

[111] G. Hoelzer et al. *Chryst. Res. Technol.*, **33**: 555, 1998

[112] A. Galler. Master thesis, Friedrich-Schiller University Jena, 2005

[113] O. Madelung (ed.). *Oxide*, volume 16a of *Landolt Börnstein Zahlenwerte und Funktionen aus Naturwissenschaften und Technik: Neue Serie, Gruppe 3* (Springer, Berlin, 1981)

[114] A. Morak. *Röntgenbeugung auf subpikosekunden Zeitskalen*. Ph.D. thesis, Friedrich-Schiller University, Jena, 2003

[115] M. Cardona. *Physical Review*, **140**: A651, 1965

[116] I. Bozovic et al. *Phys. Rev. B*, **38**: 5077, 1988

[117] B. Lüthi et al. *Phys. Rev. B*, **2**: 1211, 1970

[118] J. Bardeen et al. *Phys. Rev.*, **108**: 1175, 1957

[119] C. O. Rodriguez et al. *Phys. Rev. B*, **42**: 2692, 1990

[120] J. Orenstein et al. *Phys. Rev. B*, **42**: 6342, 1990

[121] U. Rütt et al. *Europhys. Lett.*, **39**: 395, 1997

[122] R. Wang et al. *Phys. Rev. Lett.*, **80**: 2370, 1998

[123] A. I. Dedyk et al. *Phys. Sol. State*, **39**: 305, 1997

[124] D. E. Eastman. *Phys. Rev. B*, **2**: 1, 1970

[125] V. Große et al. In *Verhandlungen der DPG* (2007)

[126] V. E. Henrich et al. *Phys. Rev. B*, **17**: 4908, 1978

[127] R. Enderlein et al. *Grundlagen der Halbleiterphysik* (Akademie-Verlag, 1992)

[128] H. E. Weaver. *J. Phys. Chem. Solids*, **11**: 274, 1959

[129] H.-M. Christen et al. *Phys. Rev. B*, **49**: 12095, 1994

[130] M. Zgonik et al. *Phys. Rev. B*, **50**: 5941, 1994

[131] J. M. Tranquada et al. *Phys. Rev. Lett.*, **73**: 1003, 1994

[132] W. H. Zachariasen. *Theory of X-ray diffraction in Crystals* (Wiley, New York, 1945)

A Basics of dynamical theory of X-ray diffraction

The central basis of the dynamical theory is solving Maxwell's equation in a material of periodic refraction index, i. e. electron density. Maxwell's equation applied to a non-conducting, non-magnetic, uncharged material are

$$\begin{array}{rclcrcl} \operatorname{rot}\mathbf{H} & = & \frac{\partial \mathbf{D}}{\partial t} & & \operatorname{rot}\mathbf{E} & = & -\frac{\partial B}{\partial t} \\ \operatorname{div}\mathbf{B} & = & 0 & & \operatorname{div}\mathbf{D} & = & 0 \\ \mathbf{E} & = & \frac{\mathbf{D}}{\epsilon_0(1+\chi)} & & & & \end{array} \tag{A.1}$$

The periodicity of the electron density ρ is reflected in a periodic susceptibilitiy χ, that can therefore be expanded into a Fourier series:

$$\chi(\mathbf{r}) = \frac{\rho(\mathbf{r})e^2}{\epsilon_0\left[m(\omega_0^2-\omega^2)-i\omega\Gamma\right]} = \sum_{\mathbf{h}} \chi_{\mathbf{h}} \exp[2\pi i \mathbf{h}\cdot\mathbf{r}], \tag{A.2}$$

where $\mathbf{h}$ is a reciprocal lattice vector, m is the electron mass, ω_0 its resonance frequency, ω the X-ray frequency and Γ a friction term. Usually the real part of the susceptibility is of the order of $\sim 10^{-4}\ldots10^{-6}$ and the imaginary part is even smaller. In the dynamical X-ray diffraction theory it is common to use the electric displacement $\mathbf{D}$ to describe the propagation of an electromagnetic wave in such a material. The wave equation for $\mathbf{D}$ is:

$$\operatorname{rot}\operatorname{rot}\left[(1-\chi)\mathbf{D}\right] = -\frac{1}{c^2}\frac{\partial^2\mathbf{D}}{\partial t^2}, \tag{A.3}$$

where it was used that χ is a small value. Due to the periodicity of the material, the electric displacement is a Bloch wave and can also be expanded into a Fourier series.

$$\mathbf{D} = \sum_{\mathbf{h}} \mathbf{D}_{\mathbf{h}} \exp[i\omega t - 2\pi i \mathbf{k}_{\mathbf{h}}\cdot\mathbf{r}] \tag{A.4}$$

with the wave vectors $\mathbf{k_h}$. Only those Fourier coefficients $\mathbf{D_h}$ contribute for which the wave vector $\mathbf{k_h}$ (nearly) satisfies Laue's equation. In a perfect crystal and for the case of an incident plane wave, $\mathbf{D}$ in the crystal is the sum of plane waves. To account for distortions, i. e. strain distributions in the crystal, Takagi allowed $\mathbf{D_h}$ to slowly vary with $\mathbf{r}$, while the wave vector $\mathbf{k_h}$ remains

constant [84, 85]. Entering with eq. (A.2) and the modified eq. (A.4) into eq. (A.3), taking into account only contributions of 2 waves inside the crystal (only two reciprocal lattice vectors involved in the diffraction process $\mathbf{h} = \mathbf{0}, \mathbf{H}$) and restricting the discussion to the 1D case leads to the following system of coupled differential equations:

$$i\frac{\lambda}{\pi}\frac{\partial D_0}{\partial x_0} = \chi_0 D_0 + C\chi_{\overline{H}} D_H - i\frac{\lambda}{c\pi}\frac{\partial D_0}{\partial t} \quad (A.5)$$

$$i\frac{\lambda}{\pi}\frac{\partial D_H}{\partial x_H} = \chi_0 D_H + C\chi_H D_0 - \alpha_H D_H - i\frac{\lambda}{c\pi}\frac{\partial D_H}{\partial t}, \quad (A.6)$$

where x_0 and x_h are the incident and diffracted directions, C is the polarization factor ($C = 1$ for σ polarization and $C = \cos 2\theta$ for π polarization) and

$$\alpha_H = \frac{G_H^2 + 2\mathbf{k_0}\cdot\mathbf{H}}{k_0^2} = -2\Delta\theta\sin(2\theta_B). \quad (A.7)$$

Here, $\mathbf{H}$ is a reciprocal lattice vector and $\mathbf{k_0}$ is the wave vector of the electric displacement wave in the incident direction. θ_B is the Bragg angle and $\Delta\theta$ is the deviation from the Bragg angle. The term $\chi_{\overline{H}}$ in eq. (A.5) is the Fourier coefficient of the susceptibility corresponding to the reciprocal lattice vector $-\mathbf{H}$. The right term in eq. (A.7) is valid for the perfect crystal case. Strain ϵ is introduced by allowing the Bragg angle to vary with depth, thus

$$\alpha = -2\sin(2\theta)[\Delta\theta + \epsilon\tan\theta] \quad (A.8)$$

for the symmetric Bragg case, i. e. the reflection from lattice planes parallel to the crystal surface. Besides the simplifications mentioned above, the following assumptions were used to derive the set of coupled equations (A.5) und (A.6):

1. The susceptibility is spatially constant.
2. The Fourier coefficients of the electric displacement field vary only slowly in space and time compared to the variations of $\exp[i\omega t - 2\pi i\mathbf{k_h}\cdot\mathbf{r}]$. Thus, only first order terms were used.

The explicit time dependence of the two wave amplitudes in the crystal $\mathbf{D_h}$ may be important if the phenomena of interest take place on times scales shorter than the time an X-ray pulse needs to traverse the extinction depth. For shorter processes the X-rays essentially see a static crystal. For the symmetric Bragg case the time to traverse the extinction depth is

$$T = \frac{\lambda\sin^2\theta}{c\pi C|\chi_{Hr}|}, \quad (A.9)$$

where $\chi_{Hr} = \mathrm{Re}\chi_H$. In Table A.1 T is given for different crystal reflections (for Ti-Kα). The characteristic time T to build up the wave field inside the

Reflection	Bragg angle θ	susceptibility $\lvert\chi_{Hr}\rvert$	Time T / fs
Si 111	26.06°	$2.058 \cdot 10^{-5}$	3
Si 311	57.28°	$1.315 \cdot 10^{-5}$	16
GaAs 222	57.57°	$2.13 \cdot 10^{-6}$	100
GaAs 400	77.07°	$6.161 \cdot 10^{-5}$	4
$SrTiO_3$ 002	44.88°	$6.314 \cdot 10^{-5}$	2

Table A.1: Extinction depth transit times for various crystal reflections. For strong reflections these times are small compared with the time scales at which the processes of interest take place.

crystal is the larger the larger the Bragg angle is and the weaker the reflection, i. e. the smaller $|\chi_{Hr}|$. For strong reflections, the characteristic time scales are of the order of few fs and thus, much smaller than the pump pulse duration (100 fs) and thus also much shorter than the characteristic time scales of induced phenomena. For weak reflections, e. g. GaAs 400, however, it would be important to consider the explicit time dependence of the wave amplitudes. For the $SrTiO_3$ 002 reflection that is investigated in the present work, the time dependencies in eq. (A.5) and (A.6) can be neglected.
For the following treatment of the X-ray diffraction in strained crystals, it is useful to introduce dimensionless quantities according to Zachariasen [132]:

$$\begin{aligned} &\text{Dimensionless depth} && : \quad A = \frac{\pi C |\chi_{\mathbf{h}r}| z}{\lambda \sqrt{|\gamma_0 \gamma_H|}} \\ &\text{Dimensionless absorption} && : \quad \kappa = \frac{\chi_{\mathbf{h}i}}{\chi_{\mathbf{h}r}} \qquad\qquad g = \frac{\frac{1-b}{2}\chi_{0i}}{C|\chi_{\mathbf{h}r}|\sqrt{|b|}} \\ &\text{Dimensionless angle} && : \quad y = \frac{\frac{1-b}{2}\chi_{0r} + \frac{b}{2}\alpha}{C|\chi_{\mathbf{h}r}|\sqrt{|b|}} \end{aligned} \tag{A.10}$$

where C is again the polarization factor, z is the depth and λ is the wavelength. γ_0 and γ_H are the direction cosines of the incident and diffracted wave and $b = \gamma_0/\gamma_H$ is the asymmetry ratio. The sample specifics are stored in the parameters $\chi_{\mathbf{h}r}$, $\chi_{\mathbf{h}i}$, χ_{0r} and χ_{0i} which are the real and imaginary parts of the Fouriercoefficients χ_H and χ_0 of the susceptibility.
The coupled system of differential equations (A.5) and (A.6) is then decoupled by introducing the term $X = \frac{D_H}{\sqrt{|b|}D_0}$ and the resulting equation is:

$$i\frac{\mathrm{d}X}{\mathrm{d}A} \quad = \quad (1+i\kappa)X^2 - 2(y+ig)X + (1+i\kappa) \tag{A.11}$$

As strain is introduced in the system by allowing the Bragg angle to vary with depth, y is a function of A also. Eq. (A.11) can be solved for strain profiles that are piecewise constant or that can be considered as. To do this, the crystal is split into laminae of thickness ΔA. The reflectivity $X(A)$ is then found by the reflectivity $X_0(A_0)$ with $\Delta A = A - A_0$:

$$X(A) = \frac{sX_0 + i(KX_0 - B)\tan[s\Delta A]}{s - i(K - BX_0)\tan[s\Delta A]}, \tag{A.12}$$

where $B = (1 + i\kappa)$, $K = (y + ig)$ and $s = \sqrt{K^2 - B^2}$. As boundary condition it can be used that $X = 0$ at the lower surface and iteration goes to the top (diffracting surface). The reflected intensity, i. e. the value to be compared with experimental results, is then $|X|^2$.

B Estimation of the errors of the $SrTiO_3$ peak parameters

As the $SrTiO_3$ 002 reflection is fitted by the sum of 2 Gaussian the errors of parameters used for further analysis are in general not simply given by the errors of the fit values. Here, formulars are derived that were used to estimate the errors of the peak parameters presented in Section 6.2. The analytical form of the function used to fit the $SrTiO_3$ 002 reflection is given by

$$S = G_1 + G_2 \tag{B.1}$$

with

$$G_1(x) = \frac{A_1}{w_1\sqrt{\frac{\pi}{2}}} \exp\left[-2\frac{(x-x_{c1})^2}{w_1^2}\right] \tag{B.2}$$

$$G_2(x) = \frac{A_2}{w_2\sqrt{\frac{\pi}{2}}} \exp\left[-2\frac{(x-x_{c2})^2}{w_2^2}\right]. \tag{B.3}$$

The partial derivatives of G_1 and G_2 are

$$\frac{\partial G_j}{\partial x_{cj}} = \frac{4(x-x_{cj})}{w_j^2} G_j \tag{B.4}$$

$$\frac{\partial G_j}{\partial w_j} = \left[\frac{4(x-x_{cj})^2}{w_j^3} - \frac{1}{w_j}\right] G_j \tag{B.5}$$

$$\frac{\partial G_j}{\partial A_j} = \frac{1}{A_j} G_j \tag{B.6}$$

$$\frac{\partial G_j}{\partial x} = -\frac{4(x-x_{cj})}{w_j^2} G_j \tag{B.7}$$

where $j = 1, 2$.

B.1 Error of the peak integral

As the total integral is given by the sum of the integrals of the two individual Gaussians

$$A = A_1 + A_2 \tag{B.8}$$

also the error is given by the sum of the individual uncertainties.

$$\Delta A = \Delta A_1 + \Delta A_2 \tag{B.9}$$

B.2 Error of peak position

The signal peaks at x_0, where $\frac{\partial S}{\partial x} = 0$. The derivative of S is given by

$$\frac{\partial S}{\partial x} = -4\frac{x - x_{c1}}{w_1^2} \cdot G_1(x) - 4\frac{x - x_{c2}}{w_2^2} \cdot G_2(x) \tag{B.10}$$

For the peak position x_0 it therefore follows:

$$0 = -4\frac{x_0 - x_{c1}}{w_1^2} \cdot G_1(x_0) - 4\frac{x_0 - x_{c2}}{w_2^2} \cdot G_2(x_0) \tag{B.11}$$

The error Δx_0 follows from the errors of the single fit parameters:

$$\begin{aligned}\Delta x_0 = &\left|\frac{\partial x_0}{\partial x_{c1}}\right| \cdot \Delta x_{c1} + \left|\frac{\partial x_0}{\partial x_{c2}}\right| \cdot \Delta x_{c2} + \left|\frac{\partial x_0}{\partial w_1}\right| \cdot \Delta w_1 + \\ &\left|\frac{\partial x_0}{\partial w_2}\right| \cdot \Delta w_2 + \left|\frac{\partial x_0}{\partial A_1}\right| \cdot \Delta A_1 + \left|\frac{\partial x_0}{\partial A_2}\right| \cdot \Delta A_2\end{aligned} \tag{B.12}$$

The partial derivatives of x_0 are obtained implicitely from equation (B.11):

$$\frac{\partial x_0}{\partial x_{cj}} = \frac{\left[\frac{1}{w_j^2} - \frac{x_0 - x_{cj}}{w_j^2}\frac{\partial}{\partial x_{cj}}\right] G_j(x_0)}{Z} \tag{B.13}$$

$$\frac{\partial x_0}{\partial w_j} = \frac{\left[2\frac{x_0 - x_{cj}}{w_j^3} - \frac{x_0 - x_{cj}}{w_j^2}\frac{\partial}{\partial w_j}\right] G_j(x_0)}{Z} \tag{B.14}$$

$$\frac{\partial x_0}{\partial A_j} = \frac{-\frac{x_0 - x_{cj}}{w_j^2}\frac{\partial G_j}{\partial A_j}}{Z}, \tag{B.15}$$

where $j = 1, 2$ and

$$Z = \left[\frac{1}{w_1^2} + \frac{x_0 - x_{c1}}{w_1^2}\frac{\partial}{\partial x_0}\right] G_1(x_0) + \left[\frac{1}{w_2^2} + \frac{x_0 - x_{c2}}{w_2^2}\frac{\partial}{\partial x_0}\right] G_2(x_0). \tag{B.16}$$

The error of the peak position is obtain by inserting eq. (B.4-B.7) and eq. (B.13-B.15) into eq. (B.12)

B.3 Error of FWHM

The rocking curve is slightly asymmetric. It is therefore necessary to calculate the two positions at which the intensity is at half maximum, independently. For both positions x_1 and x_2 the intensity is equal:

$$S(x_1) = S(x_2) = \frac{1}{2}S(x_0) \tag{B.17}$$

Entering with equation (B.1) in (B.17) results in implicite equations for x_1 and x_2, respectively:

$$0 = G_1(x_{1/2}) + G_2(x_{1/2}) - \frac{1}{2}\left(G_1(x_0) + G_2(x_0)\right) \tag{B.18}$$

The uncertainty of the line width is given by $\Delta w = \Delta x_1 + \Delta x_2$. Δx_1 is calculated as

$$\Delta x_1 = \sum_{j=1,2} \left\{ \left| \frac{\partial x_1}{\partial x_{cj}} \right| \Delta x_{cj} + \left| \frac{\partial x_1}{\partial w_j} \right| \Delta w_j + \left| \frac{\partial x_1}{\partial A_j} \right| \Delta A_j \right\}. \tag{B.19}$$

The error of x_2 is calculated analogously. The required partial derivatives are determined implicitely from eq. (B.18). How to obtain the partial derivative of x_1 with respect to x_{c1} is shown in detail. The other partial derivatives will be only indicated. Considering x_1 as function of x_{c1} only, equation (B.18) is rewritten as:

$$0 = G_1(x_1(x_{c1}), x_{c1}) + G_2(x_1(x_{c1})) - \frac{1}{2}(G_1(x_0, x_{c1}) + G_2(x_0)) \tag{B.20}$$

It was used, that the FWHM itself is dependent on the positions of the individual Gaussian peaks, but not on the peak position of the total reflection curve x_0. Applying $\frac{\partial}{\partial x_{c1}}$ to equation (B.20) yields

$$0 = \frac{\partial G_1(x_1)}{\partial x_1}\frac{\partial x_1}{\partial x_{c1}} + \frac{\partial G_1(x_1)}{\partial x_{c1}} + \frac{\partial G_2(x_1)}{\partial x_1}\frac{\partial x_1}{\partial x_{c1}} - \frac{1}{2}\frac{\partial G_1(x_0)}{\partial x_{c1}} \tag{B.21}$$

and solving for $\frac{\partial x_1}{\partial x_{c1}}$ gives:

$$\frac{\partial x_1}{\partial x_{c1}} = \frac{\frac{1}{2}\frac{\partial G_1(x_0)}{\partial x_{c1}} - \frac{\partial G_1(x_1)}{\partial x_{c1}}}{\frac{\partial G_1(x_1)}{\partial x_1} + \frac{\partial G_2(x_1)}{\partial x_1}} \tag{B.22}$$

The remaining partial derivatives are

$$\frac{\partial x_1}{\partial p_{i,j}} = \frac{\frac{1}{2}\frac{\partial G_j(x_0)}{\partial p_{i,j}} - \frac{\partial G_j(x_1)}{\partial p_{i,j}}}{\frac{\partial G_1(x_1)}{\partial x_1} + \frac{\partial G_2(x_1)}{\partial x_1}} \tag{B.23}$$

$$\frac{\partial x_2}{\partial p_{i,j}} = \frac{\frac{1}{2}\frac{\partial G_j(x_0)}{\partial p_{i,j}} - \frac{\partial G_j(x_2)}{\partial p_{i,j}}}{\frac{\partial G_1(x_2)}{\partial x_2} + \frac{\partial G_2(x_2)}{\partial x_2}} \tag{B.24}$$

$$\tag{B.25}$$

where $p_{i,j} = \{x_{cj}, w_j, A_j\}$. Entering with eq. (B.23, B.24) and eq. (B.4-B.7) into eq. (B.19) and the corresponding equation for x_2 readily gives the error of the FWHM for the $SrTiO_3$ 002 reflection.

Acknowledgements

I would like to thank all the people who helped making this work possible.
First of all, I thank Prof. Förster for the interesting topic of this thesis and Ingo Uschmann for the support - experimentally and mentally (he never gave up hope that the experiment would successfully run one day - and he was right).

Most of the data presented here were taken in a six week experimental campaign. Anyon who had experienced such a time (even if shorter) knows, what this means. Such a campaign cannot be done by one person alone. I would like to thank all who contributed to it. Especially I am grateful to Ingo Uschmann, Flavio Zamponi and Tino Kämpfer.

For their help with the cooling technique I thank Thorsten Köttig and Matthias Thürk.

Veit Große has manufactured the excellent samples used for these studies. And even though the data presented in this work were taken from two different samples only, he prepared a lot more in order to find the right parameters for the preparation process. Veit Große and Frank Schmidl were also the persons who had periodically to struggle with my questions about superconductivity and thin films. For their input and patience I am very grateful.
Stimulating impulses for the discussion of the strange response of the sample also came from Prof. Seidel.

This work would not have been possible without extensive discussions with a number of physicists who never evaded my questions at any time even though they were not working in the field of high temperature superconductors. Among these are Prof. Sauerbrey, Martin Preuß and Robert Lötzsch.

Hilmar Straube performed some ray tracing calculations for which I like to thank him.

Thanks is also due to the laser crew and the staff from the workshops.

I enjoyed very much the pleasant working atmosphere in the X-ray optics group. It helped a lot, when the experiments did not work as I wanted them to.

Last but not least I would like to thank my friends and my family (especially Michele) for reminding me every day that there are more important things in the world than broken Cooper pairs.

Curriculum Vitae

Persönliche Daten

Name:	Lübcke
Vorname:	Andrea
Geburtsdatum:	9. Dezember 1978
Geburtsort:	Grevesmühlen

Ausbildung

1985–1991:	Grundschule
1991–1997:	Gymnasium Brüel
1997–2002:	Studium der Physik an der Friedrich-Schiller Universität Jena
2000 – 2001:	Sechsmonatiges Forschungspraktikum am Lawrence Livermore National Laboratory (USA)
Diplomarbeit zum Thema:	"Ausnutzung des Borrmanneffektes zur Entwicklung eines ultraschnellen Schalters im Röntgenbereich"
Seit Oktober 2002:	Doktorandin am Institut für Optik und Quantelektronik der FSU Jena

Jena, den 4. Juni 2007 Andrea Lübcke

Ehrenwörtliche Erklärung

Ich erkläre hiermit ehrenwörtlich, dass ich die vorliegende Arbeit selbstständig und ohne Hilfe Dritter und ohne Benutzung anderer als der angegebenen Hilfsmittel und Literatur angefertigt habe. Die aus anderen Quellen direkt oder indirekt übernommenen Daten und Konzepte sind unter Angabe der Quelle gekennzeichnet.

Weitere Personen waren nicht an der inhaltlich-materiellen Erstellung der vorliegenden Arbeit beteiligt. Insbesondere habe ich hierfür nicht die entgeltliche Hilfe von Vermittlungs- bzw. Beratungsdiensten (Promotionsberater oder andere Personen) in Anspruch genommen. Niemand hat von mir unmittelbar oder mittelbar geldwerte Leistungen für die Arbeiten erhalten, die im Zusammenhang mit dem Inhalt der vorgelegten Dissertation stehen.

Die Arbeit wurde bisher weder im In- noch im Ausland in gleicher oder ähnlicher Form einer anderen Prüfungsbehörde vorgelegt.

Die geltende Prüfungsordnung der Physikalisch-Astronomischen Fakultät ist mir bekannt

Ich versichere ehrenwörtlich, dass ich nach bestem Wissen die reine Wahrheit gesagt und nichts verschwiegen habe.

Jena, den 4. Juni 2007 Andrea Lübcke